January 2022

The Impact Of Stress Dependent Permeability Alteration On Gas Based EOR In The Bakken Formation

Ailin Assady

Recommended Citation

Assady, Ailin, "The Impact Of Stress Dependent Permeability Alteration On Gas Based EOR In The Bakken Formation" (2022). *Theses and Dissertations*. 4319.
https://commons.und.edu/theses/4319

THE IMPACT OF STRESS DEPENDENT PERMEABILITY ALTERATION ON GAS BASED EOR IN THE BAKKEN FORMATION

By

Ailin Assady
Bachelor of Science, Petroleum Engineering, University of Tehran, 2014
Master of Science, Reservoir Engineering, Amir Kabir (Polytechnic) University, 2017

A Dissertation

Submitted to the Graduate Faculty

of the

University of North Dakota

in fulfillment of the requirements

for the degree of

Doctor of Philosophy

Grand Forks, North Dakota

August
2022

Name: Ailin Assady

Degree: Doctor of Philosophy

This document, submitted in partial fulfillment of the requirements for the degree from the University of North Dakota, has been read by the Faculty Advisory Committee under whom the work has been done and is hereby approved.

DocuSigned by:
Vamegh Rasouli
0EB950E8C9C9450...
Vamegh Rasouli

DocuSigned by:
Tao Jiang
4E5F948EDBBF43C...
Tao Jiang

DocuSigned by:
Hui Pu
C03B8AB854E4448...
Hui Pu

DocuSigned by:
Kegang Ling
AE10F7CCAFC7487...
Kegang Ling

DocuSigned by:
Sattar Dorafshan
60308943EA7B4C7...
Sattar Dorafshan

Name of Member 6 - delete if not needed

This document is being submitted by the appointed advisory committee as having met all the requirements of the School of Graduate Studies at the University of North Dakota and is hereby approved.

DocuSigned by:
Chris Nelson
2E0AF088C733403...
Chris Nelson
Dean of the School of Graduate Studies

7/19/2022
Date

PERMISSION

Title	The Impact of Stress Dependent Permeability Alteration on Gas Based EOR in The Bakken Formation
Department	Petroleum Engineering
Degree	Doctor of Philosophy

In presenting this thesis in partial fulfillment of the requirements for a graduate degree from the University of North Dakota, I agree that the library of this University shall make it freely available for inspection. I further agree that permission for extensive copying for scholarly purposes may be granted by the professor who supervised my thesis work or, in his absence, by the chairperson of the department or the dean of the Graduate School. It is understood that any copying or publication or other use of this thesis or part thereof for financial gain shall not be allowed without my written permission. It is also understood that due recognition shall be given to me and to the University of North Dakota in any scholarly use which may be made of any material in my thesis.

Ailin Assady
July 18, 2022

TABLE OF CONTENTS

LIST OF FIGURES vii

LIST OF TABLES... xi

ACKNOWLEDGMENTS xii

ABSTRACT... xiv

CHAPTER

1 INTRODUCTION 1

- 1.1 Research Objectives... 1
- 1.2 Methodology 2
- 1.3 Highlights... 4
- 1.4 Thesis Organization 4

2 REVIEW OF LITERATURE: BAKKEN FORMATION CHARACTERIZATION 6

- 2.1 Introduction... 6
- 2.2 Geologic Setting of the Bakken Formation 7
- 2.3 Permeability Measurements for Bakken Samples 9
  - 2.3.1 Permeability Measurements.. 10
  - 2.3.2 Pulse-Decay Method.. 11
  - 2.3.3 Oscillating-Pulse Method.. 14
  - 2.3.4 Stress-dependent Permeability.. 16
- 2.4 Digital Rock Physics for Rock Characterization 19
  - 2.4.1 Processing 22
  - 2.4.2 Porosity Determination.. 23
  - 2.4.3 Absolute Permeability Measurement.. 24
- 2.5 Summary... 26

3 ASSESSMENT OF PERMEABILITY HYSTERESIS DURING LOADING/UNLOADING IN BAKKEN FORMATION 28

3.1 Introduction and Review 28

3.3.1 Permeability Measurement Validation 37

3.2 Description of Rock Sample 31

3.3 Permeability Measurement 34

3.4 Digital Rock Analysis 39

3.5 Stress-Dependent Permeability 43

3.6 Permeability Damage Calculation 48

3.7 Experiments and Results 53

3.7.1 Stress Range 53

3.7.2 Pore Pressure 62

3.7.3 Pore Size Distribution 70

3.8 Summary and Conclusions 74

4 PERMEABILITY MODELING USING MACHINE LEARNING 77

4.1 Introduction 77

4.2 Machine Learning Workflow 79

4.3 Data Gathering and Integration 79

4.4 Data Pre-processing 80

4.5 Machine Learning Model Description and Setup 84

4.6 Results and Discussions 86

4.6.1 Low-level Generalization (Single Well) 86

4.6.2 High-level Generalization (Multiple Wells) 90

4.7 Conclusions 92

5 SIMULATION MODELING AND EVALUATING FOR PERFORMANCE 93

5.1 Introduction 93

5.2 Historical Bakken Tests 94

5.2.1 Water Injection Tests 94

5.2.2 Gas Injection Tests..95

5.3 Reservoir Pressure Regions 97

5.4 Reservoir Simulation Modeling..99

5.4.1 DSU Variable Regions...99

5.4.1.1 Simulation Procedures 102

5.4.2 Results and Discussion 104

5.4.2 Bottom Hole Pressure Variable Regions 109

5.4.2.1 History Matching 111

5.4.2.2 Equation of State (EOS) Model...112

5.4.2.3 Single Fracture Stage Modeling...112

5.4.2.4 History Match and Simulation Results 115

5.4.2.5 EOR Forecasting...116

5.5 Summary and Conclusions 120

6 CONCLUSIONS AND RECOMMENDATIONS 123

6.1 Conclusions..123

6.2 Recommendations..128

REFERENCES 130

LIST OF FIGURES

Figure Page

2-1 Extend the Williston Basin with the major North Dakota structures shown 7

2-2 Stratigraphic column showing the lithology of the Bakken Formation 8

2-3 Cores from different Bakken units for lithology identification 8

2-4 Schematic (courtesy of NER) and Configuration of the permeability measurement apparatus (UND-PE lab) 13

2-5 An example from Ling et al., 2013 shows pulse decay analysis for a Middle Bakken core sample 14

2-6 (a) permeability reduction for a MB sample under higher effective stress (i.e., net confining pressure): (b) stress-dependent permeability on logarithmic scale for matrix and fractured rock samples 17

2-7 An integrated digital rock workflow used in this study 22

2-8 Calculating connected pore algorithm; (a) Input data (b) Result of Axis connectivity with z-axis orientation 24

2-9 Velocity streamlines in the calculation of intrinsic permeability tensor 25

3-1 Middle Bakken core samples used in this study (a) Sampling well location, Mountrail County (b) Raw core samples (c) Prepared core samples 34

3-2 (a) Configuration of permeability measurement apparatus (b) Permeability measurement assembly 35

3-3 Boundary condition applied in pulse-decay configuration 36

3-4 An example of pulse decay analysis for Middle Bakken core sample (a) Changes of the upstream and downstream pressure during experiment (b) in (ΔP_t / ΔP_0) vs. time plot 37

3-5 Steady-state permeability measurement 38

3-6 Measured permeability using steady-state and pulse-decay methods 39

3-7 Digital rock analysis procedure; extracting a sub-volume, segmentation, pores, extracting pore network model; core sample#1 41

3-8 Example of one sub-volume segmentation, total porosity, effective and isolated pores, 3D pore-network; core sample#2 43

3-9 Pore size distribution from 3-D pore networks of sample 1 and 2 43

3-10 Shaded area between loading and loading path represents permeability evolution....48

3-11 Dividing permeability hysteresis path to two separated regions; before and after critical effective stress....49

3-12 Exponential and power-law models fitted to first experiment data points for core-sample#2 with no pore pressure effect....51

3-13 Average permeability damage: power-law match, exponential match, experiment graph, based on the loading/unloading curve (5 to 55 MPa) for core sample#2 52

3-14 Comparing long and short loading/unloading pressure 55

3-15 Short length stress loading/unloading and exponential fitted model....55

3-16 Dividing the data points into two regions and fitting exponential model on semi-log plot; core sample#2....56

3-17 Calculated average permeability damage for short and long hysteresis path; core sample#2 ....

3-18 Material constants for short and long hysteresis paths: (a) Loading (b) Unloading....58

3-19 Comparing prediction hysteresis path using short and long length stress exponential relationship....60

3-20 Material constant using power law model 61

3-21 Effect of pore pressure during loading the sample 63

3-22 Effect of pore pressure during unloading the sample 64

3-23 Comparing permeability values for different pore pressure and constant effective stress....65

3-24 Dividing the loading/unloading path for experiment data points with non-zero pore pressure....66

3-25 Comparing average permeability results for second experiment (pore pressure effect) ...67

3-26 Loading/Unloading average stress sensitivity coefficient based on pore pressure change, after and before critical point....68

3-27 Comparing average permeabilities with stress sensitivity coefficients before and after critical point for three different pore pressure values....69

3-28 Comparing measured permeabilities for two different PSDs....71

3-29 Dividing the data point into two regions and fitting exponential model on semi-log plot; core sample#1....72

3-30 Average permeability damage for both core samples....73

3-31 Average stress sensitivity coefficient for both core samples....73

4-1 Machine learning roadmap....79

4-2 Permeability versus net confining stress of rock samples from Middle Three Forks formation, well Debrecen 1-3H....80

4-3 Graphical detection of permeability outliers based on the quartiles method....81

4-4 Correlation matrix for regression inputs....82

4-5 Log transform of the output (permeability)....83

4-6 Artificial neural network structure....85

4-7 Evolution of mean squared error as a function of the applied number of neurons for the training set, the validation set and the testing set....87

4-8 MSE distribution along the data subset for validation and training, 8 hidden neurons (right), 5 hidden neurons (center), and 34 hidden neurons (left)....88

4-9 Linear fit of predicted permeability with the real permeability data (ANN model - Single Well)....88

4-10 Comparing permeability-stress models matching with the experimental core data for Three Forks formation....89

4-11 Comparing permeability-stress models matching with the experimental core data for Bakken formation....

4-12 Non-equal distribution of data, overestimation/underestimation of permeability data.....91

4-13 (a) Linear fit of predicted permeability with the real permeability data (Decision tree model – Six Well). (b) Predicted permeability vs. true permeability for tested well....91

5-1 Reservoir pressure vs. Time and respective regions 98

5-2 Single-stage base model with 8 layers for Bakken and Three Forks Fm....101

5-3 Decline oil rate under primary depletion for cases 1, 2 and 3 102

5-4 Pressure disturbance in a (a) Single-stage (b) stimulated reservoir 103

5-5 Oil recovery factor for cases 1, 1.A, 1.B, 1.C, and 1.D 104

5-6 Incremental produced oil over time-Case 1 105

5-7 Incremental produced oil over time-Case 2 107

5-8 Incremental produced oil over time-Case 3 107

5-9 Incremental oil prediction for studied cases (1, 2 and 3C) 108

5-10 3D illustration of the reservoir simulation model 110

5-11 Top view – NFR, induced and hydraulic fractures 113

5-12 History matched DFN Pressure dependent permeability – sets – Exponential models before and after critical effective pressure 115

5-13 Results of history matching model for well MB-PROD....116

5-14 Bottom hole pressure response from three different permeability correlations (1. No permeability change, 2. Exponential 3. Two sets of exponentials before and after critical pressure)....117

5-15 Incremental oil of all three models during regions 2 and 3: (a) BHP at region 2 (b) BHP) at region 3....119

5-16 Incremental oil of all two sets of the exponential model during huff and puff and continuous gas injection....120

LIST OF TABLES

Table Page

2-1 Summary of permeability measurements for MB samples based on different methodologies 19
3-1 Calculated total and effective porosity 42
3-2 Summary of fitted curves for whole data sets, before and after critical point 51
5-1 Summary of the historical Bakken EOR pilot tests 94
5-2 Different reservoirs regions and possible injection scenarios....99
5-3 Fracture properties used in this study 100
5-4 Different simulation case studies in this study 104
5-5 Properties of modeled Middle Bakken and Three Forks Formations used for simulation griding 111
5-6 Injected gas compositions used in the simulation model....112
5-7 Different reservoirs regions and possible injection scenarios....114
5-8 Optimum injection case selected for this study 117
5-9 Different reservoirs regions and possible injection scenarios....120

ACKNOWLEDGMENTS

I would like to express my sincere appreciation and gratitude to my advisor Dr. Vamegh Rasouli for the continuous support of my Ph.D. study and related research and his patience, motivation, and immense knowledge. His guidance helped me in all the time of research and writing of this thesis. I could not have imagined having a better advisor and mentor for my Ph.D. study. Special thanks to Mr. Tao Jiang, my co-advisor, for his invaluable encouragement and guidance during my studies. I thank him for all the time he spent reviewing the work and providing me with insightful comments. I also could not have undertaken this journey without my defense committee: Dr. Hui Pu, Dr. Kegang Ling, and Dr. Sattar Dorafshan, who generously provided knowledge and expertise.

I had the pleasure of starting to work at the Energy and Environmental Research Center (EERC) as an intern and reservoir engineer, where I am learning and thriving. I am honored to acknowledge the North Dakota Industrial Commission, which has provided funding to the EERC that is allowing research on this fundamental concept to continue through the State Energy Research Center (SERC). My experience at the EERC has been and will continue to be a very important and fulfilling part of my life.

Additionally, I also acknowledge the material means during this work and the financial support I received from the University of North Dakota Petroleum Engineering Department. The financial help of the American Chemical Society Petroleum Research Fund (ACS-PRF) and the North Dakota Industrial Commission (NDIC) is highly appreciated. This endeavor would not

have been possible without their generous support. I also acknowledge the North Dakota Geological Survey, Wilson M. Laird Core Library for providing us with core samples and Thermo-Fisher Scientific company for their software support. I would like to thank CMG (Computer Modelling Group) for providing the CMG license and their continuous support.

I would like to mention Dr. H. Jabbari, who supervised the initial part of this work (Chapter 2 and 3). I thank all my colleagues, especially my fellow classmate Dr. Abdelmalek Bellal for his encouragement, support, discussion, and advice. He assisted as a key person in the data analytic part; without his help, the concept of this work could not go beyond an idea.

Finally, I would be remiss in not mentioning my family and friends, especially my mother, Mahvash, and two sisters, Anousha and Atoosa, for their support, encouragement, understanding, and love throughout my life. Their belief in me has kept my spirits and motivation high during this process. I will always be grateful for having such great family and friends.

Dedicated to my Dear Father, Behrouz Assady.

ABSTRACT

Effective stress exerted on porous rocks can change and alter reservoir permeability accordingly during reservoir development. The permeability evolution under different reservoir statues will impact oil production and EOR design in the Bakken shale porous media. An accurate permeability model can improve capturing the fluid transport mechanism and create a reliable long-term dynamic fluid forecast via reservoir simulation. This research is focused on studying permeability alteration behavior under different pressure circumstances. The reservoir gradually loses its original pore pressure during production, increasing reservoir net effective stress. Therefore, a reduction in reservoir properties such as permeability or porosity can occur in response to net stress change within the pores due to the withdrawal of the fluids from the reservoir. In contrast, a fluid injection can reduce formation pressure drop and maintain pressure during the development process in tight rock reservoirs. However, physical parameters (e.g., permeability) cannot be fully recovered, and back to its initial value, this nature of rock is characterized as stress sensitivity or hysteresis. Stress-dependent properties are hard to model accurately in reservoir simulation because of the uncertainty associated with the stress-dependent coefficients and correlations. The conventional reservoir simulators use the compressibility concept to consider the change of pore volume, where the rock properties are usually assumed to be insensitive to the evolution of the stress state. However, reservoir compaction and stress changes can significantly impact reservoir management and production performance. In this study, a review of different rock characterizations of the Three forks and Bakken core samples to determine stress dependency of permeability and its hysteresis during pressurizing/ depressurizing rock samples is conducted. Core samples from the Middle Bakken formation in North Dakota for further permeability alteration experiments are utilized. This data will be used to evaluate the permeability behavior with respect to critical pressure known as pressure shock. Also, the data analytic approach to model permeability on a larger scale based on several inputs such as depth, different net confining stress, and porosity is performed. Numerical reservoir simulation using Bakken and Three Forks formation is utilized to integrate permeability pressure correlation in simulation modeling and compare several injection scenarios with non-sensitive permeability models.

The results indicate that ignoring the effect of slope discontinuity at a critical effective stress using the same equation for a whole range of data is inaccurate. Indeed, developing permeability-stress correlations cause inapplicable mathematical models and, consequently, erroneous permeability damage prediction. Following this concept, modifying the correlation for two Bakken cores shows that considering the critical points on each hysteresis path could improve the final form of the stress-dependent permeability relationship. Also, machine learning modeling using available lab core data can be used as an alternative method to capture Bakken and Three Forks permeability changes under different net confining stress while incorporating the critical pressure effect. Furthermore, to evaluate the several gas injection scenarios, the timely reservoir pressure change is divided into three distinct regions where critical effective pressure impact and miscibility of gas injection vary based on current reservoir statutes. The results demonstrate that gas injection in these formations is a strong function of fracture/matrix permeability damage. Compared to the model without considering stress-dependent permeability, the cumulative production could reduce because the permeability decreases along

with reservoir pressure decline. As a result, considering permeability modeling in numerical simulation can help to understand the role of different injection scenarios and enhance the knowledge for controlling and managing reservoir production by proper operation decisions in unconventional reservoirs.

CHAPTER 1

INTRODUCTION

The objective of this research is to investigate the impact of the exerted effective stress on porous rocks and respective reservoir permeability alteration in Bakken and Three Forks Formation based on the experimental core data. The first question in reservoir characterization of the Bakken is raised from the difficulties associated with naturally fractured reservoirs in permeability alteration due to the depletion or injection and prediction of permeability under reservoir conditions where the lab experiments are limited. The second question is related to the significance of the different roles of fracture in the hysteresis path before and after critical effective stress. The third question is how permeability evolution under different reservoir statues will impact oil production and EOR design in the Bakken shale porous media.

1.1. Research Objectives

This work aims to 1) study and measure the Bakken permeability change over a wide range of pressure changes and determine the critical effective stress point; 2) propose a novel method of curve fitting model to experimental permeability-stress data points with considering critical effective stress. 3) Integrate modified correlations with critical point consideration in a numerical simulation model where the permeability evolution and cumulative fluid production are calculated at each step. The effect of reservoir compaction and permeability damage under several lab conditions can be utilized to evaluate different gas injection scenarios for the Bakken Formation. An accurate model will allow simulating the permeability change when water/gas injection is performed to maintain reservoir pressure and prevent permeability decline. This work aims at improving the numerical simulation model for reliable production forecast and EOR performance evaluation, leading to optimal EOR operations in unconventional reservoirs.

1.2. Methodology

This study consists of three main approaches: 1) Experimental and digital rock characterization 2) Data analysis 3) Numerical reservoir simulation.

Experimental Rock Characterization: Description of rock structures and characterizing rock to understand permeability, geomechanics, storage capacity, and fluids transport. The measurement of permeability of Bakken rock samples is very challenging due to their extremely low permeability. In this study, the number of Bakken core samples' permeability were determined using steady state, oscillating-pulse, and pulse-decay methods. Also, the elastic moduli (i.e. Young's modulus, Poisson's ratio) of these core plugs were estimated through the measurement of seismic velocities (Vp and Vs); furthermore, permeability is determined under different confining pressure and pore pressure for two different pore size Middle Bakken core samples using pulse decay method. These experiments were carried out using the Autolab-1500 in UND-PE Lab equipment by first gradually increasing the confining pressure from 1000 psi to 6000 psi. Then subsequently reduced back gradually to 1000 psi where permeability was measured at each step. Based on laboratory measurements, the influence of stress loading/unloading and the effect of pore pressure, and stress range on permeability damage for Middle-Bakken core samples were illustrated. This approach can help us to get a better insight into the impact of mentioned parameters on permeability hysteresis path and permeability evolution under different effective stress conditions.

Digital Rock Analysis: While in conventional reservoirs, the concept of Darcy flow is a reasonable assumption in simulating fluid flow, this is not applicable in unconventional reservoirs. In ultra-small pores of shale formations, fluid flow may not meet one or more assumption requirements for Darcy flow. In those nanopores, the turbulent flow can occur and causes deviation from the conventional models. The development of more accurate models to improve our knowledge of complex flow through nano-/micro-scale pores of shales is necessary considering the unique features of unconventional reservoirs. Micro-CT scan of the Bakken shale core sample was applied in visualizing the microscopic pores, and rock properties e.g. porosity, and pore size distribution, were determined.

Data analysis: Based on the experimental results, the permeability follows an exponential trend with respect to effective stress. However, these correlation coefficients are taken from core samples at a certain depth and cannot represent the permeability evolution of the entire formation. The permeability-pressure relationship dominant in tight fractured formations was examined by utilizing the machine learning (ML) approach. Also, a large volume of data related to porosity and permeability at different net confining pressures was collected from the NDIC Website. An artificial neural network (ANN) model was trained based on the variation of core samples' permeability for a wide range of depths to define a general model and predict permeability alteration as a function of the effective stress changes. The developed model can be introduced in reservoir modeling to sheds more light on realistic production forecast and EOR performance evaluation, leading to optimal EOR operations in unconventional reservoirs.

Numerical Simulation: Although high oil recovery results have been observed in the lab for enhanced oil recovery (EOR) in the Bakken, all previous nine EOR pilots in the field showed that oil recovery improvement is minimal. It is clear that there is a gap between laboratory studies and field practices for EOR in the Bakken, and the fundamental fluid flow/EOR mechanisms in the tight shaly formations have not been fully understood. Existing simulation models are mostly based on flow mechanisms in conventional reservoirs, and these models have strong limitations when applied to design EOR plans in the Bakken unconventional reservoir. The effect of reservoir compaction and permeability damage presented in this work was used to evaluate different gas injection scenarios for the Middle Bakken and Three Forks Formation. A comprehensive fracture and reservoir modeling was conducted to evaluate the effects of permeability evolution under numerous injection scenarios. The EOR performance of the stress-dependent model against the non-sensitive permeability model was demonstrated.

1.3. Highlights

- Several permeability alteration experiments were carried out to better understand the permeability behavior under a condition similar to reservoir statutes and to determine hysteresis response.
- To the best of my knowledge, this is one of the first studies in the Bakken formation to use the machine learning approach and estimate permeability under a wide range of depth and net confining stress, based on available core data extracted from several wells and offers a cost-saving method. The machine learning model covering critical effective stress during the permeability modeling will increase the accuracy and simplicity of the permeability modeling.

1.4. Thesis Organization

This dissertation contains six chapters as below:

Chapter 1 provides the background to the project and a brief explanation of the integrated workflow. It also contains the objectives of this study, the methodology used, and the significance of this research.

Chapter 2 is a brief review of the literature regarding Bakken rock characterization, a summary of past studies related to the lab work, numerical simulations, and analytical models to study the permeability evaluation.

Chapter 3 presents the experimental procedure using the Auto-Lab 1500. Also, a summary of digital rock characterization is integrated for calculating effective porosity and pore size distribution of core samples, and further evaluation of permeability behavior explanations. Permeability damage and different permeability correlation will be discussed.

Chapter 4 consists of introduces a novel approach for permeability modeling and prediction. Two different ANN models for one and six wells are presented. The proposed models were compared to experimental results. The advantages and disadvantages of this approach and improving solutions are discussed.

Chapter 5 is dedicated to a simulation study where a new region of pressure will be defined based on the findings of Chapters 3 and 4, a synthetic reservoir model with an integrated ANN permeability pressure model, and a history-matched Bakken/Three Forks reservoir model with complex fracture network and permeability change will be used to evaluate gas injection scenarios to improve incremental oil production.

In Chapter 6 a summary of the findings from this study will be presented along with some recommendations and future studies that can be carried out.

CHAPTER 2

REVIEW OF LITERATURE: BAKKEN FORMATION CHARACTERIZATION

2.1. Introduction

The Bakken reservoir of Williston Basin is an unconventional shale formation, composed of an upper shale member (UB), a middle member (MB) of dolomitic silt- and sandstone, and a lower shale member (LB). Activity in developing the Bakken Formation has increased due to the success of horizontal drilling coupled with multi-stage hydraulic fracturing stimulation (Jabbari and Zeng, 2011; Jabbari and Benson, 2013). However, maintaining production— which requires hydraulic fracturing and well stimulation— is quite challenging for these types of wells. Hence, the primary recovery factors in the Bakken Fm remain very low, estimated at less than 10% of the original oil in place. Figure 2-1 shows the boundaries of the Williston Basin defined within the US portion of the basin.

Gas injection can be an effective enhanced oil recovery method in naturally fractured or hydraulically fractured tight formations. Recent studies showed that CO2-EOR could be a viable method to increase recovery in tight shale plays (Yang et al., 2015; Zhang et al., 2018; Abuamarah et al., 2019; Tang et al., 2020). The primary recovery mechanism in a tight formation is basically depressurization and solution gas drive. There are several EOR methods for improving the recovery among which gas injection can be an effective method.

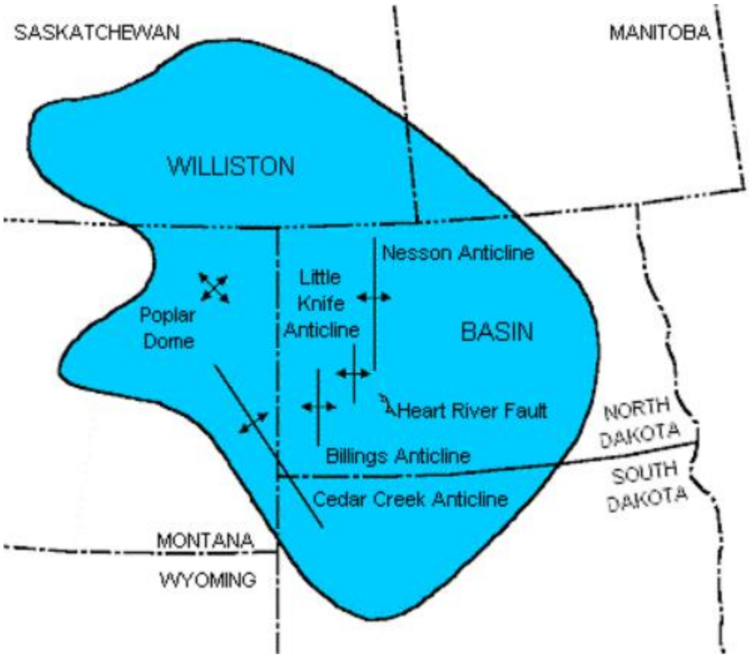

Fig. 2-1. Extend the Williston Basin with the major North Dakota structures shown (Courtesy of North Dakota Geological Survey)

This section aims at better understanding the characteristics of the Bakken Fm. and the mechanisms of gas-based EOR in the Williston Basin, and assessing the potential for optimal EOR projects to add reserves. The results from the literature are presented and compared for validation.

2.2. Geologic Setting of the Bakken Formation

The Bakken Formation is an organic rich shale, mudstone, and sandstone that were deposited during the late Devonian and early Mississippian periods. This large formation is located in the western portion of North Dakota, forming the Williston Basin, the northeastern region of Montana, and extends into Saskatchewan and Manitoba. It is divided into three members, the Upper, Middle and Lower Bakken. The Middle Bakken serves as the reservoir thereby hosting all the mobile oil. The Upper and Lower members have almost the same lithofacies comprising of organic rich shales as classified by Smith and Bustin, 1995 and LeFever et al., 1991 (see Figure 2-2).

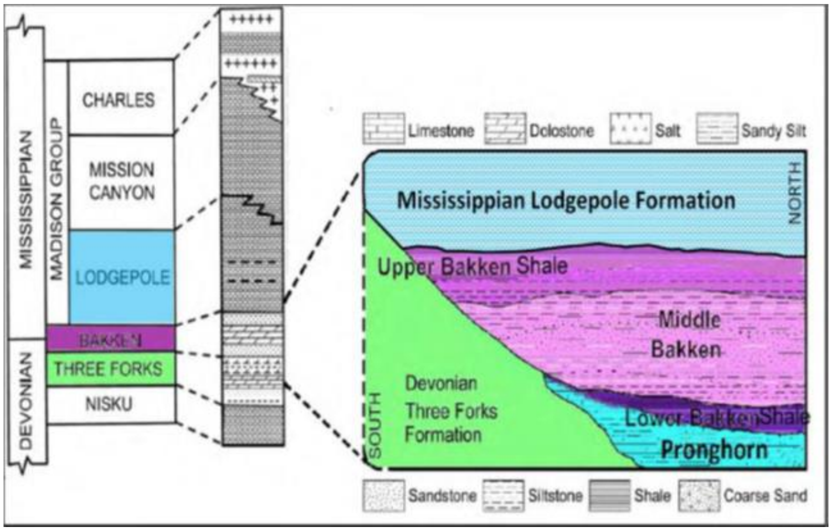

Fig. 2-2. Stratigraphic column showing the lithology of the Bakken Formation (Jin et al., 2017)

Moreover, the depositional sequence of the Bakken Fm. started during the late Devonian period in the Upper Kaskaskia sequence. From the stratigraphic studies, the Bakken Fm. is recognized as the basal unit of the Upper Kaskaskia, with its black color and a sharp erosional contact with the Three Forks Fm. Rapid transgression leads to the deep marine depositional environment of the Lower Bakken member (Gerhard at al., 1990).

This rapid deposition favored an anaerobic environment that preserved organic matter. The Middle Bakken was deposited in three different episodes ranging from offshore for sub-unit A, fair-weather wave base and the zone of breaking waves for sub-unit B, and between storm and fair-weather wave base for sub-unit C (Smith and Bustin, 1995) (Figure 2-3).

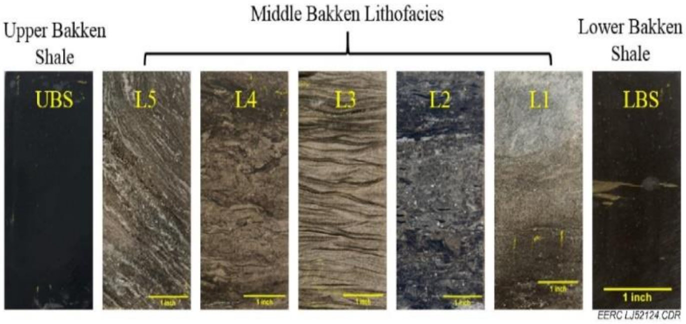

Fig. 2-3. Cores from different Bakken units for lithology identification (Jin et al., 2013)

2.3. Permeability Measurements for Bakken Samples

Numerous researchers have shown that nano/micro-scale heterogeneity has a noticeable impact on mesoscale properties, physical phenomena, and hydrocarbon recovery assessment (Farajzadeh et al., 2011; Alharthy et al., 2013). Therefore, it is essential to determine the microstructure of the rock matrix. In specific cases, one of the prevalent methods for enhancing oil recovery lies within gas injection and huff and puff processes. These methods have gained the attention of researchers and have shown recovery enhancement from both experimental and field results. Among the gasses considered, CO_2 can be preferable due to its low minimum miscible pressure (MMP) with oil, and relatively a smaller molecule (0.33 nm) compared to other common injected gases (e.g., 0.39 nm for C_1 and C_2 and 0.43 nm for C_3). Hence, to predict hydrocarbon production, we need to obtain the characteristics, such as porosity, specific surface area, and pore size distribution to analyze the nano-scale transport within the pores of shale and fracture network (Lu et al., 1995; Chen et al., 2013).

Accurate estimation of total hydrocarbon storage will lead to reservoir management from economic and technical perspectives. Among all input parameters to reservoir simulation, absolute permeability is counted as an essential one to forecast hydrocarbon production. This becomes more important when dealing with tight, heterogeneous reservoirs where the permeability can be in the nano-Darcy magnitude. Due to the complexities that exist in tight reservoirs (i.e., mineralogy and extremely tight pores), conventional core analysis methods (CCAL) are not reliable to apply and would lead to highly erroneous results. Therefore, based on the Darcy (1856) experimental work, numerous analytical and experimental works were conducted to improve the accuracy of permeability measurements for tight samples (Dong et al., 2010; Ma and Zoback, 2016; Gan et al., 2018; Civan, 2018), which are categorized into two general methods: steady-state and unsteady-state methods.

2.3.1. Permeability Measurements

The permeability measurement of tight core samples is always challenging due to their micro-/nano-pores and extremely low permeability. On the other hand, with the existence of micro cracks which usually are not captured during CT scanning, due to insufficient resolution, the validity of matrix permeability measurements becomes more challenging (Li et al., 2015). These experiments are often time-consuming and expensive where the flow rate is hard to control, and the measurements are overly sensitive to the type of fluids employed in the experiments. These factors can cause the permeability measurements to be uncertain and some representative methods ought to be used to estimate the permeability of such a tight formation as the Bakken Fm. (Liu et al., 2010; Cao et al., 2016).

Due to the laboratory implementation of Darcy's law, this method is considered a standard industry method for decades (Darcy, 1856; Gan et al., 2018). In several studies, such as Sinha et al., 2012, and Lasswell et al., 2013, the steady-state method for shale rock samples was utilized. These measurements were based on Darcy's Law, which would require a constant pressure gradient across the sample while monitoring the flow rate. This method requires two pore pressure intensifiers with automated recycling in order to create identical upstream and downstream pressures on opposite ends of the core plug. However, pressure stabilization happens over a long time, and this is one of the main disadvantages of steady-state method for unconventional samples. Besides, it can hardly measure the permeability of rocks up to 10^{-5} μm^2 (Trimmer, 1982; Andabily and Rahman, 1995). Although this type of test would take a long time to yield an accurate permeability estimate, it is still the mostly validated way to measure intrinsic permeability for liquid-rich reservoir rocks (Li et al., 2015).

Due to mentioned challenges for steady-state measurement, transient methods are considered as an alternative way of measuring permeability in tight rocks. Two common transient methods are pulse-decay and oscillating-pulse methods. The transient methods of permeability measurement include prescribing a transient pressure disturbance to the differential equation of fluid flow (i.e., diffusivity equation). The pore pressure at the top of the sample is controlled while the bottom side is attached to a fixed volume containing the pore fluid. The test starts by perturbing the pressure at the upstream. This perturbation of pressure (transfer function) travels through the core sample and is monitored at the downstream. This transfer function is related to a) the length and cross-sectional area of the sample, b) the permeability and specific storage of the sample, c) the viscosity and compressibility of the pore fluid, and d) the volume in communication with the downstream.

2.3.2. Pulse-Decay Method

In this method, at first, a pressure disturbance is applied on one side of the reservoir. Next, the propagation of the created pulse towards the opposite side of the reservoir will be observed with respect to time. The characteristics of a core sample, such as permeability, core size and test fluid, volumes of upstream and downstream reservoirs as well as the pore-fluid properties can affect the decaying time observed from the test. Darcy’s law cannot be applied directly to this method due to flow rate fluctuations and pressure differences in the experiment. Therefore, the mass conservation is adopted to analyze the pressure transient data in this method (Gan et al., 2018). In the work by Brace et al., 1968, they conducted permeability measurements by using the concept of transient flow method as given by Eqs.2-1 and 2-2.

$$(P_1 - P_f) = \Delta P \left[\frac{V_2}{V_1 + V_2}\right] \times e^{-\alpha t} \tag{2-1}$$

$$\alpha = \frac{kA}{\mu\beta L}\left[\frac{1}{V_1} + \frac{1}{V_2}\right] \tag{2-2}$$

Where V_1 and V_2 are upstream and downstream volumes, P_1 and P_f are upstream, downstream pressures. Permeability as a function of pressure decay (Eq.2-1) can be calculated after determining "α" from Eq.2-2, which is the slope of the line on a semi-log plot of Ln $((P_1 - P_f)(V_1 + V_2)/(\Delta p V_2))$ versus time. As Brace et al., 1968, mentioned, applying these equations to permeability measurements requires us to use small values of Δp for valid estimations. Dicker and Smits (1988) further improved the pulse-decay method by incorporating the compressive storage effects into the flow equation as given by:

$$\Delta p_D(a, b, t_D) = 2\sum_{m=1}^{\infty} \exp(-t_D\theta_m^2) . \frac{a(b^2 + \theta_m^2) - (-1)^m b\sqrt{(a^2 + \theta_m^2)(b^2 + \theta_m^2)}}{\theta_m^4 + \theta_m^2(a + a^2 + b + b^2) + ab(a + ab + b)} \tag{2-3}$$

Where "a" and "b" are the ratio of core sample pore volume to up-/down-stream volumes and "θ_m" is referred to the roots of this term:

$$\tan\theta = \frac{(a + b)\theta}{\theta^2 - ab} \tag{2-4}$$

To conduct a pressure measurement from these methods, the pressure between upstream and downstream containers needs to reach equilibrium. This process can take a long time, especially for tight core samples. To resolve this problem, Jones (1997) introduced a methodology that required applying smaller upstream and downstream pressures with smooth pressure gradients. He introduced a factor "f" given by $f=\theta_m/(a+b)$ to simplify the analytical solution where turned the pulse decay equation into:

$$\alpha = \frac{\mathrm{fkA}}{\mu\beta\mathrm{L}}\left[\frac{1}{\mathrm{V}_1} + \frac{1}{\mathrm{V}_2}\right] \tag{2-5}$$

Later, Cui et al., 2019, presented a method to use gas adsorption during the measurement, where gas transport in low permeability reservoir would result in more reliable and accurate permeability estimation. Also, Metwally, 2011, presented another pulse-decay method by considering a large upstream volume in order to make the ratio of up- to down-stream volumes (a/b) tend to infinity. This leads to a simplified solution for the pulse-decay calculations. Figure 2-4 describes the configuration of the experimental setup based on the work by Ling et al., 2013, and Assady et al. (2019). The equipment utilized is a servo-hydraulic operated system for triaxial measurements with software controlled arbitrary stress paths on rock specimens up to 50.8 mm (2.0 in) in diameter at in-situ stress conditions, pore pressures, and temperature.

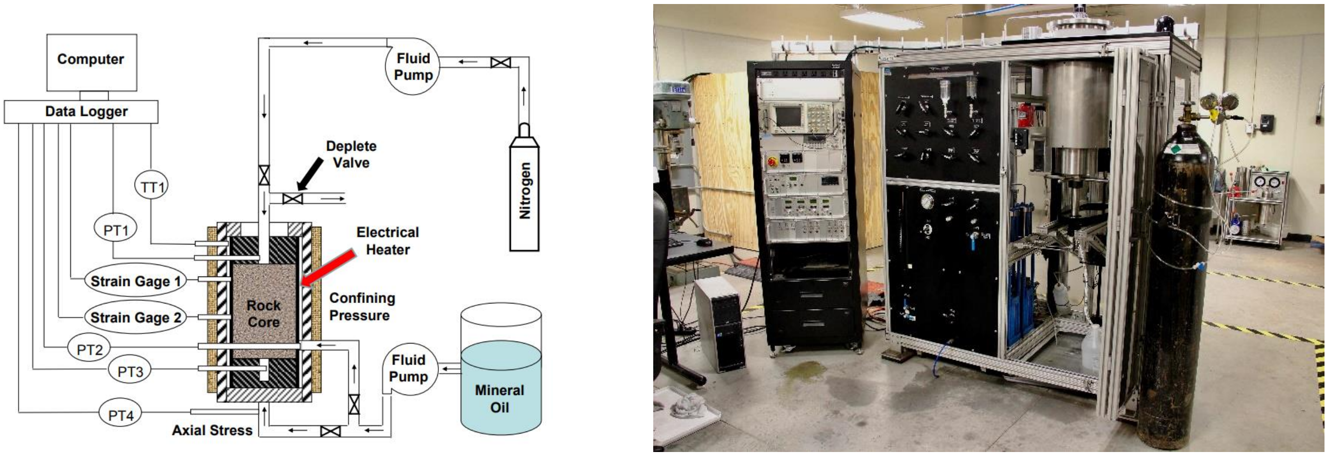

Fig. 2-4. Schematic (courtesy of NER) and Configuration of the permeability measurement apparatus (UND-PE lab)

It can measure permeability under steady-state and different transient methods, consisting of three main components: a) pressure vessels and four associated pressure intensifiers, b) electronics and control panel, and c) a computer system to analyze data. The core samples are cleaned through a vacuum process before running the tests. It is an essential task since the permeability is sensitive to core cleaning. After applying the pressure pulse and observing the response at the downstream reservoir, permeability can be estimated by fitting the response trend to the analytical solutions (Figure 2-5).

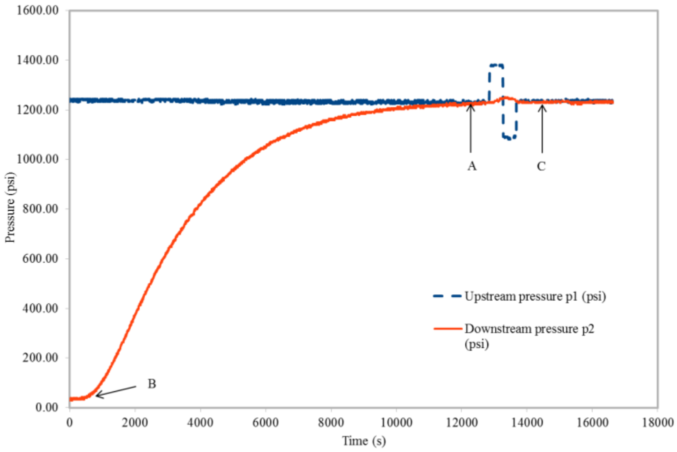

Fig. 2-5. An example from Ling et al., 2013 shows pulse decay analysis for a Middle Bakken core sample. Changes in upstream and downstream pressures during the experiment. Point 'B' marks the time that the pressure disturbance arrives at the downstream end of the core. Point 'A' marks the time that the upstream and downstream pressures reach equilibrium. Point 'C' represents the end of oscillating pulse.

Also, the absolute permeability can be estimated from the oscillating-pulse method which is faster and non-destructive as described below. Normally, permeabilities measured from different methods are not in good agreement (Bertoncello, 2013), however, among other faster methods the pulse-decay has shown closer results to the steady-state method (Wang and Hart,1993; Ling and He, 2013; Li et al., 2015).

2.3.3. Oscillating-Pulse Method

In this method, the first step is to stabilize the upstream and downstream pressures before running the experiment. Next, a sinusoidal pressure wave generated at the upstream propagates through the core sample. Then, permeability is measured by recording the amplitude attenuation and the phase shift of this pressure wave at the downstream (Ling et al., 2013). The relationship between the upstream and downstream propagation can vary based on the length, cross-sectional area, permeability, specific storage of the sample, the viscosity of the fluid, and the compressibility of the fluid. The measurable amplitude ratios “R” and phase difference are expressed in term of α and γ (Krantz et al., 1990):

$$\mathrm{R}^2 = \frac{4\alpha^2}{(2\alpha^2 + 1)\cosh 2\gamma + (2\,\alpha^2 - 1)\cos 2\gamma + 2\alpha(\sinh 2\gamma - \sin 2\gamma)} \tag{2-6}$$

$$\delta = \tan^{-1}\left(\frac{\tanh(2\alpha\tan\gamma + 1) + \tan\gamma}{\tan\gamma + 2\alpha - \tanh\gamma}\right) \tag{2-7}$$

Once “R” and “δ” are measured from laboratory experiments, “α” and “γ” can be calculated from Eqs.2-6 and 2-7 that yields permeability as follows:

$$\mathrm{K} = \frac{\mu c V_2}{A}\left(\frac{\alpha\omega L}{\gamma}\right) \tag{2-8}$$

A significant advantage of this method as compared to the pulse-decay is a shorter run time it takes for the measurements to complete. However, one of the main drawbacks of oscillating-pulse permeability measurement would be determining an optimum frequency of oscillation, which may vary from one sample to another (Krantz et al., 1990). Therefore, the estimated permeability cannot be valid under the condition of low signal-to-noise ratio measurements. Moreover, different analysis techniques may result in different values of permeability from the same experiment. For instance, using this method for Middle Bakken samples did not lead to consistent results (He and Ling, 2016 and Assady et al., 2019) owing to the above reasons. Also, He and Ling, 2016 inferred that the shape of a sine wave needs to be selected so that it matches the range of permeability understudy which, in turn, adds to the uncertainty of the oscillating-pulse method. All in all, the oscillating pulse method may not be the best option for measuring permeability in tight formations.

2.3.4. Stress-dependent Permeability

Permeability dependence on effective stress change (σ_{eff}) is well understood in the geomechanics area (Civan, 2017; An et al., 2019). The results of most experiments for Bakken core samples have documented the significant effect of confining stress change and pore pressure on permeability (Li et al., 2015; Karimi and Kazemi, 2017). This is due to the high sensitivity of permeability to effective stress in rock samples containing tight pores (Dong et al., 2010; Teklu et al., 2016). Ewy et al., 2012, presented the relationship between permeability and the change in pore pressure and effective stress in the form of:

$$\mathrm{k} = \mathrm{f}(\mathrm{P_c} - \alpha \mathrm{P_p}) \tag{2-9}$$

Where P_p is pore pressure, P_c is confining stress and α is Biot's coefficient. In most experiments conducted on Bakken core samples Biot's coefficient is considered unity which leads to the effective stress as the difference between applied confining pressure and the internal pore pressure (i.e., $\sigma_{eff}=P_c-P_p$) (Terzaghi, 1943). Based on the laboratory experiments conducted on core samples, the permeability relationship with effective stress can vary between exponential and power-law models, depending upon rock sample characteristics. The following is the exponential relationship (David et al., 1994):

$$\mathrm{k} = \mathrm{k_0} \exp\left(-\gamma\left(\mathrm{P_c} - \mathrm{P_p}\right)\right) \tag{2-10}$$

Where "k_0" is the ambient permeability (i.e., under atmospheric pressure) and "γ" denotes a material constant varying between 10^{-3} to 10^{-2} and is dependent on the rock type. Also, the following relationship can demonstrate the stress dependency of permeability, given by (Shi and Wang, 1986):

$$\mathrm{k} = \mathrm{k_0}\left(\frac{\mathrm{P_c}}{\mathrm{P_p}}\right)^{-\mathrm{p}} \tag{2-11}$$

Where “p” is representing a material constant varying between 0.1 and 2 for different core samples and under various effective-stress conditions. Therefore, different core samples may show different behavior under variable effective stress that requires us to plot permeability change under various cases of pore pressure and confining stress vs. effective stress (Ma and Zoback, 2016). In addition, Teklu et al., 2016, studied the impact of different parameters on permeability variations in tight reservoirs, such as temperature, net stress, pore pressure, and cyclic matrix and fractures. They showed that permeability decreases with elevating net stresses, in addition to a direct relation with temperature. They also illustrated that the major role of the stress dependency of permeability occur in nano-pore sizes rather than mirco-pore-size rock samples. This rock behavior is depicted in Figure 2-6, where Li et al., 2015, characterized Middle Bakken core samples and found the inverse relationship between permeability and effective stress.

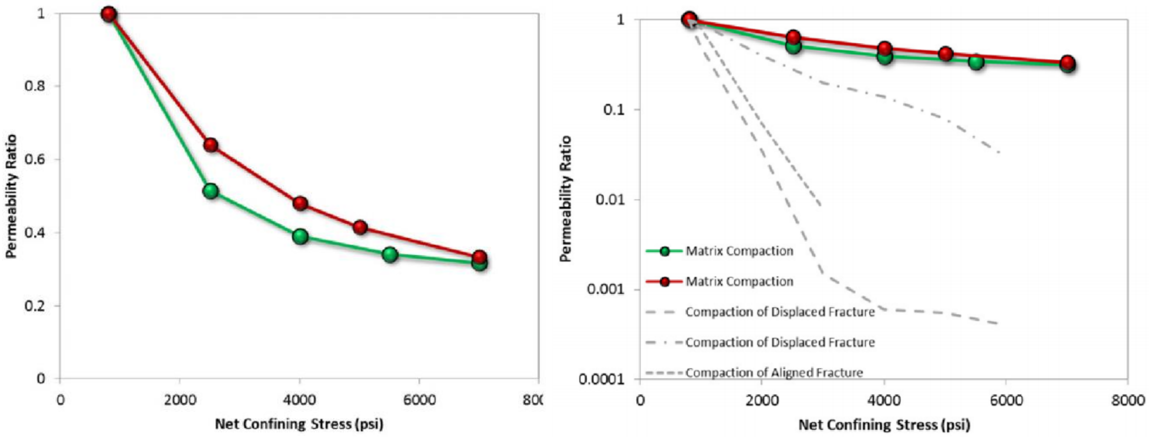

(a) (b)

Fig. 2-6. (a) permeability reduction for a MB sample under higher effective stress (i.e., net confining pressure); (b) stress-dependent permeability on logarithmic scale for matrix and fractured rock samples (Li et al., 2015).

These plots display an exponential-decline behavior for the permeability trends of Middle Bakken core samples. In these measurements the confining stress ranged from 2000 to 6000 psi meaning the variation of net confining stress being between 800 and 6000 psi which caused a permeability reduction by a factor of 2. applied confining stress range in this work is covering a typical stress cycle during the life of a Bakken well.

It is important to measure the permeability under conditions of realistic confining stress and quantify the change in permeability due to the pore pressure reduction during production. Basically, the production decline is dependent on the compaction behavior of hydraulic fractures (propped and unpropped), natural fractures, and matrix (Jones & Owens 1980). As the reservoir pressure decreases, the effective stress ($\mathrm{P_c - \alpha P_p}$) increases which, in turn, the formation permeability reduces due to the stress dependency as shown in the work by Chu et al., 2012, and Li et al., 2015.

In tight reservoirs, such as the Bakken Fm., the main path of fluid flow would be micro-cracks which can be closed from elevated stresses during the depletion. On the other hand, during stress unloading (e.g., injection) a portion of those collapsed cracks might not open thus giving rise to the concept of permeability hysteresis. This means that for minimizing permeability reduction, it might be necessary to inject at the early stage of production prior to the onset of formation damage from increased effective stress. Also, for better designing of multi-stage fracking and re-fracturing operations, a thorough understanding of the permeability hysteresis of the formation is of paramount importance. This work and previous research by Civan, 2005, and Teklu et al., 2016, present case studies for stress-dependent permeability during stress loading/unloading that can help us in reservoir management and optimal timing of workover/EOR operations.

Table 2-1 lists the measured permeabilities from an integrated characterization of Bakken core samples under low effective-stress and lab conditions as reported by several authors. Note that various approaches were employed to measure the permeability, including air permeability, Klinkenberg method, steady-state and unsteady-state liquid permeability as well as MICP methods (Li et al., 2015; He and Ling, 2016; Kurtoglu, 2013; Teklu et al., 2016; Karimi and Kazemi, 2017; Assady et al., 2019). This table shows that by combining and comparing the results from different measurement methods, one can better estimate matrix permeability in a tight shale play.

Table 2-1. Summary of permeability measurements for MB samples based on different methodologies

References	K_0(md)	Depth (ft)	Methods
Kurtoglu (2013)	10^{-5} to 10^{-4}	10,600 to 10,850.45	Steady-State
Ling and He (2015)	0.00007 to 0.0052731 0.00004 to 0.002	-	Pulse-Decay Pulse-Oscillation
He and Ling (2016)	0.0002 to 0.002	-	Pulse-Decay, MICP
Teklu et al. (2016)	0.01414 to 0.00563	10,400	Pulse-Decay
Karimi and Kazemi (2017)	10^{-3} to 10^{-2}	9,800-10,300	
Assady et al. (2019)	0.0006 to 0.0011 0.0005 to 0.0007	10,645.5 to 10,680 ft.	Steady-State Pulse-Decay

2.4. Digital Rock Physics for Rock Characterization

A recent modeling-based study shows that multiphase fluid behavior and flow in liquid-rich shales are significantly different in nanoscale pores compared to microscale pores as it highly depends on pore throat size, fluid viscosity, and density (Sorensen et al., 2016; Alharthy et al., 2013). As it is discussed in previous sections, obtaining internal parameters such as porosity, specific surface area, and pore size distribution is crucial to understand the nano-scale transport processes between pores in shale and fracture systems. Fluid flow knowledge within tight reservoirs would lead to design effective CO2 injection and EOR schemes and predict reliable hydrocarbon production within tight reservoirs (Chen et al., 2013). Consequently, accurate estimation of total hydrocarbon storage will improve reservoir management, economically and financially.

Several researchers have been studied on characterizing rock structures, specifically micro/nanostructure of rock with different resolution of 2D and 3D images (e.g., Doyen, 1988; Yoshino et al., 2005). Lindquist et al., 2000, used synthetic and low-resolution tomographic images to characterize pore network geometry, but their study did not contain physical properties for pore sizes less than 5 microns. Lock (2001) proposed a method for predicting sandstone permeability. He could obtain almost an exact procedure for predicting sandstone permeability in range of 10 to 100 md. In 2004, Okabe and Blunt determined permeability for reconstructed pore network by using Lattice-Boltzmann method (LBM).

With the development of advanced imaging technique and computation ability, Digital Rock Analysis (DRA) has been applied to various types of rocks such as carbonates and shales to study rock properties, e.g., elastic properties, relative permeability (Madadi et al., 2009; Kalam, 2012; Wang et al., 2016). Chen et al., 2013, showed most of the intra-kerogen pores are isolated and having relatively spherical morphology, by using image segmentation and separation. Their statistical results illustrated 92.7% of the total pore number is due to nano-pore with diameter less than 100 nm, while they make up only 4.5% of the total pore volume. Thomson et al., 2018, provided a detailed recipe for image processing, characterizing pore network geometry, and determining the permeability through connected pore space for Fontainebleau and Berea Sandstones. In general, pore scale characterization using digital rock analysis can facilitate capturing heterogeneity. It can illustrate the complex microstructure of the tight medium using imaging techniques such as FIB/SEM and Micro-CT (Cudjoe et al., 2019; Saif et al., 2017; Sondergeld et al., 2010). The digital rock approach (DRA) can provide a great amount of data in a short time specifically in ultra-low permeability reservoirs (Bautista. et al., 2018). It is accepted that DRA is a necessary complement of lab experiments, and it may be referred as virtual laboratory/experiments (Dvorkin et al., 2008; and Liu et al., 2018). Due to the heterogeneity and clastic layered rocks of shale plays, it is challenging to acquire core samples from the Bakken Fm. Thus, Digital rock analysis (DRA) can be substantially helpful to replace the use of conventional cores as it can readily capture pore geometries and fluid flow behavior.

In this section, the characterization of micro-CT/FIB-SEM Bakken core samples is presented, using Digital Rock Analysis. The goal of this effort is to employ an integrated DRA workflow to Bakken samples, resulting in accurate capturing heterogeneity and characterization of nanopore space within tight core samples. The integrated workflow contains the basic digital rock physic procedure to determine substantial nano-scale properties (Figure 2-7). To analysis reconstructed 3D volume of core samples, few pre-processing on images, such as removing noises and artifacts are applied. Then grains and pores are separated using one of the common methods of segmenting different phases, namely marker-based watershed algorithm. After completing pre-processing and processing steps (i.e., various filtering, de-noising and segmenting pore/grains) connected pores and calculated total and effective porosity, and absolute permeability are identified. The characterized micro-CT/FIB-SEM results with MICP for porosity, and pulse decay method with absolute permeability are validated.

2.4.1 Processing

Segmentation (i.e., binarization) of sample images is crucial step in characterizing pores to extract the geometrical information of all individual pores inside the 3-D domain. Accurate segmentation can be defined as extracting isolated individual phases with same brightness and color (Thomson et al., 2018). There are no exact and same procedures for all images and each image has its own specific method to determine adequate output. However, numerous approaches are introduced for image segmentation. Improper discretization of pores and grains can generate imprecise or wrong results during pore characterization. Therefore, High image resolution, valid pre-processing and exact pore/grain segmentation are the key to the success DRA. Accurate visualization and measurement of connected pores are necessary for obtaining gas and oil storage, optimizing hydraulic fracturing, and CO_2-EOR.

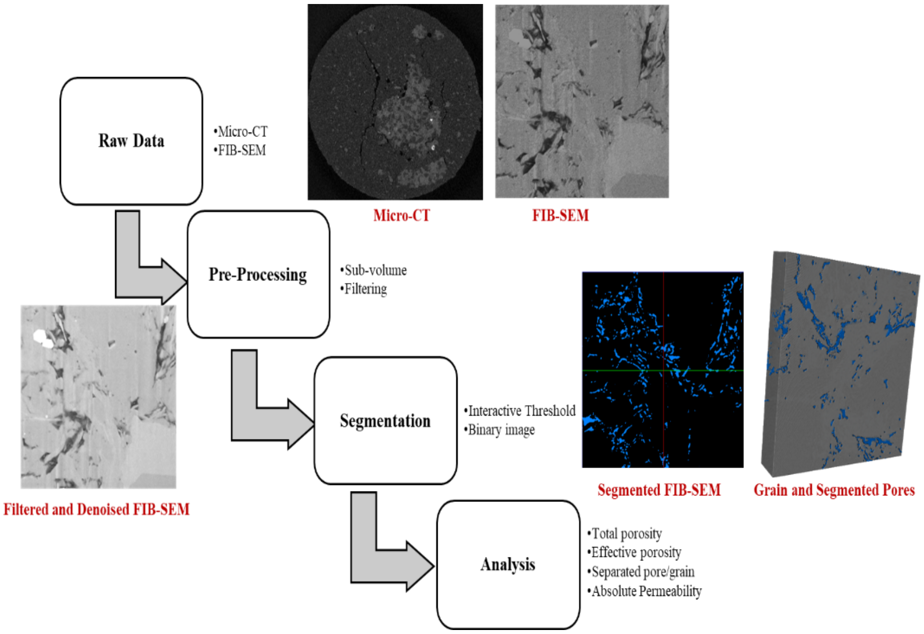

Fig. 2-7. An integrated digital rock workflow used in this study.

We utilized thresholding visually, manually, and automatically based on the image gray scale values and tried to get the closest match by checking the results. For doing so we used different algorithms based on computational analysis and different common methods for image analyzing. For some type of stacks like FIB-SEM which have similar density for pores and organic matters, simple thresholding can cause error for adequate pore/grain separation. To reduce this error, it recommended by many authors to use marker-based water-shed segmentation to enhance labeling the image (Cudjoe et al., 2019). The major idea of water-shed segmentation is based on the concept of topographic representation of image intensity (Gonzales and Woods, 2002; Seanger et al., 2011). The concept behind this algorithm is to simulate the flooding from a set of labeled regions in 3D images. Figure 2-7 shows marker-based watershed segmented pores carried out for FIB-SEM Bakken sample.

2.4.2 Porosity Determination

There are plenty of methods (e.g., experimental and well logging) for determining some physical properties such as porosity. However, these methods can give users the total porosity without considering the degree of pore connectivity (Ellis and Singer, 2007; Thomson et al., 2018). Therefore, we utilized DRA to calculate and obtain effective porosity which can help us to evaluate its impact on fluid flow within tight oil reservoir such as Bakken samples. For determining connected pore spaces, we applied axis connectivity modulus to the labeled images (or segmented images). This tool within the commercial DRA software extracts a binary image that includes all connected pores in two planes inside the 3D domain (i.e., each two parallel planes). In this case, all floating pores will be removed. Then, porosity for total and connected pores based on volume fraction were calculated. The results indicate that pores are dispersed and isolated within the Middle Bakken core samples, causing remarkable difference in total/effective porosities. This can be accounted as one of the major reasons of low oil recovery in unconventional reservoirs (Assady and Jabbari 2020). The procedure of obtaining connected pore space is shown in Figure 2-8. The results for calculated total porosity and connected porosity are shown in Table 2-2.

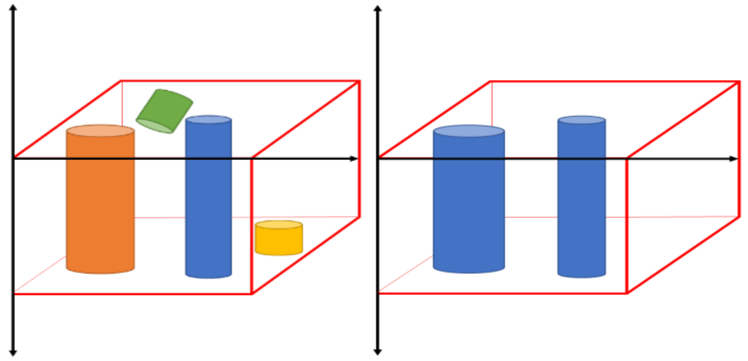

(a) (b)

Fig. 2-8. Calculating connected pore algorithm; (a) Input data (b) Result of Axis connectivity with z-axis orientation (courtesy of Thermo-Fisher Scientific)

2.4.3 Absolute Permeability Measurement

Absolute permeability as an intrinsic property indicates the capability of rock to transfer a fluid. To determine absolute permeability, a commercial simulator was used for modeling single phase fluid flow through the 3D images of the connected pore space discussed above. To calculate effective permeability for infinite medium, the applied software uses average volume form of the Stoke equations. A change of scale is necessary to get equations valid on the entire volume. Volume averaging is a technique that applies when there is a change of scale. It can smooth equations (Whitaker, 2013) and leads to develop a closure problem which transforms the Stokes equations into a tonsorial problem. It remains similar to the stokes equations, despite the fact it is a higher order problem (Eqs. 2-12 and 2-13):

$$\vec{\nabla}.\vec{\vec{D}}=\vec{\vec{0}} \tag{2-12}$$

$$\nabla^2.\vec{\vec{D}}-\vec{\nabla}\,\vec{d}=\vec{\vec{I}} \tag{2-13}$$

Where:

$\vec{\vec{D}}$ Tensor as the source of the spatial deviation of the velocity (velocity perturbation field)

$\vec{d}$ A vector as the source of the spatial deviation of the pressure (pressure perturbation field)

$\vec{\vec{I}}$ The unit tensor

By solving Eqs. 2-12 and 2-13, the mean value of $\vec{\vec{D}}$ over the system volume is calculated, and the permeability tensor is given by:

$$\vec{\vec{k}}=\frac{1}{v}\int_v \vec{\vec{D}}\,dv \tag{2-14}$$

For tensor calculation no slip condition is applied at the fluid-solid interfaces. The sample represents a macroscopic, infinite material (Figure 2-9). This method can give permeability value along any direction of space.

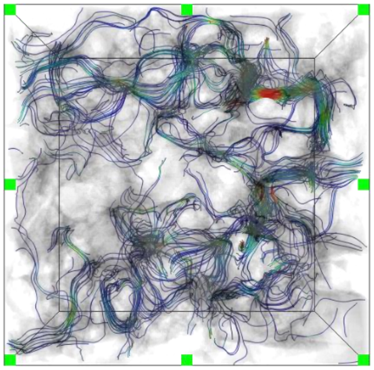

Fig. 2-9. Velocity streamlines in the calculation of intrinsic permeability tensor

As mentioned by Chen et al., 2013, in order to match the simulation model with production data, matrix/fracture permeability were adjusted to higher values, which seemed not representing the properties of the real reservoir. This uncertainty in reservoir properties led to the difference between numerical simulation and real-field data. In recent decade, scholars have put efforts on using modern characterization methods on the nano/micro scale to better understand the fluid flow in tight shale plays. This can help to understand the nan-scale fluid properties and dominant fluid flow mechanisms in tight formations (Sorensen et al., 2017; Chen et al., 2013). The deviation of digital rock analysis (DRA) is reported to be significant for some sample from experimental works. This is attributed to the voxel resolution of images (Saenger et al., 2011) where it may not be possible to distinguish the pores smaller than the resolution of images, or it can be due to inaccurate pore/grain segmentation from noise and manual errors (Jouini et al., 2015; Soulaine et al., 2016; Devarapalli et al., 2017). On the other hand, a major limitation of DRA method is the small zone of investigation (a few millimeters) compared to the size of a core plug or the real reservoir. This shortcoming can be addressed either by running several simulations on different images of rock samples (Baustista et al., 2018) or by applying a proper upscaling method in order to estimate flow properties at the macro/reservoir scale. Reliable properties lead to more accurate well/reservoir modeling and thus optimizing well spacing, completion strategies, and wiser development planning.

2.5. Summary

This work briefly explains the main methods of reservoir characterization and how/where we can collect and acquire proper data for unconventional reservoir properties estimation. the purpose of this integrated characterization workflow is to provide the necessary data for building geologic models and/or analyzing well/reservoir performance in natural depletion and EOR operations. Indeed, a thorough reservoir characterization can help companies to compare different EOR scenarios and to choose best ones from a list of scenarios to execute. Below are a few key points from this review:

- Pulse decay would be the most common method for permeability measurements due to its reliability and close match with the results from steady-state method.
- The exponential decline of permeability vs. effective stress is due to existing of ultra-small pore sizes in tight Bakken core samples. Permeability continuously declines upon loading the sample and does not fully retrieve during unloading; therefore, permeability hysteresis can occur.
- Acquiring core samples can be costly and time consuming. In case of unconventional reservoirs, such as the Bakken Fm., it is even more challenging due to the heterogeneity and clastic layered rocks of these shale plays. To tackle this hurdle, one would use DRA (digital rock analysis), a powerful tool, which may replace the use of conventional core samples, and can readily capture the heterogeneity, pore geometries and fluid flow behavior within the formations.

CHAPTER 3

ASSESSMENT OF PERMEABILITY HYSTERESIS DURING LOADING/UNLOADING IN BAKKEN FORMATION

3.1. Introduction and Review

Effective stress exerted on porous rocks can increase during reservoir developing due to formation pressure decreasing. Consequently, an increase in elastoplastic deformation, permeability/porosity reduction and less production can occur (Sang et al., 2017). Fluid injection (i.e., water or gas) can mitigate formation pressure reduction and maintain formation pressure during development process in tight rock reservoirs. However physical parameters, such as permeability or porosity cannot be fully recovered, this nature of rock is characterized as stress sensitivity or hysteresis (Li 2008, Nai and Gang 2018), and this characteristic is more significant in unconventional tight plays, due to very low porosity and connectivity, compared to that in conventional reservoirs (Lui et al., 2011). Permanente permeability change which known as formation damage has an outmost impact on recovery in tight oil reservoirs (Chen et al., 1999). Therefore, increasing the knowledge of permeability hysteresis during loading/unloading pressure, can help to understand the role of the different stresses, pore structures and fractures on rock hydrocarbon production (Elhaj et al., 2018). Many studies focused on the hysteresis phenomenon during loading and unloading to analyze permeability stress sensitivity, mathematically and empirically (Kranzz et al., 1979; Bernabe 1987; Selvadurai, 2015). However, obtaining empirical or deriving consistent formulas for permeability calculation under different stress condition is not fully achieved yet. This is due to the complex nature of such phenomenon. Therefore, most published results and equations are not in agreement with each other and there are shortcomings with using such models (Civan, 2017).

In 1985, Wissler and Simmons, analyzed the degree of reversibility of stress-dependent permeability. Bernabe (1987), investigated the stress-sensitivity hysteresis effect on rock properties through laboratory experiments. He observed that the rock stress sensitivity hysteresis effect would be insignificant or minimized after aging treatment and its impact would be diminished after multiple aging treatment, because rock would no longer follow the original stress path. Also, Warpinski and Teufel (1992), proposed that the stress-sensitivity hysteresis would disappear after multiple aging cycles of rock samples. Morris et al., 2003, applied theoretical models to analyze the porosity and permeability evolution of Berea sandstone during effective stress changes. They used simple material model in which the original pores and induced pores were considered separately. Maiti et al., 2008, illustrated hysteresis path for different particle porosity in trickle-bed reactors (TBRs). This study could show the importance knowledge of hysteresis behavior in particle porosities.

As several authors mentioned in their work, an exerted stress to core samples can lead to the permeability reduction by various mechanisms such as closing microcracks, rearrangement of grains and crushing of existing pores (Morris et al., 2003; Civan, 2017). In opposite, it might improve permeability by creating new cracks and opening conduit paths in core samples (Zoback and Byerlee, 1975; Paterson, 1978; Morris et al., 2003; Civan, 2017). Ghabezloo et al. (2009) applied a conceptual pore-shell model, to represent the influence of the effective stress on permeability. In 2010, Dong et al., concluded that compaction in both sandstone and shale formations was not reversible during permeability hysteresis. Also, he showed that rock type is one of the significant parameters that can affect this phenomenon. However, they did not see any rock type impact on porosity hysteresis. Later, (Teklu et al., 2016), studied on different parameters, such as temperature, net stress, pore pressure, cyclic matrix, and fracture in tight reservoirs. They showed that as net stress increases permeability decreases, while permeability has direct relation with temperature changes. Also, they investigated on cyclic hysteresis for both matrix and fracture and concluded that new micro cracks can be created at each time of injection, which can improve hydraulic fracturing technique. In the same year (Ma and Zoback 2016), presented the effect of pressure loading/unloading on ultra-sonic velocities and geo-mechanics properties and considered their dependency on confining and pore pressure. They disproved the accuracy of applying simple effective stress law in high P_c and P_p. In 2017, Civan theoretically illustrated the effect of pore elasticity on hysteresis of permeability and porosity, which is more accurate than common empirical correlations. Besides, he indicated using the kinetics-based phenomenological models would help to analyze porosity and permeability stress dependency, precisely (Civan 2017). He made an attempt to investigate and develop theoretically consistent approaches in describing the rock properties as a function of the effective stress in a manner to honor the shock effect and slope discontinuity that occur at a critical effective stress. As Civan 2017 mentioned in his paper, at critical effective stress, a sharp alteration in contribution of matrix and fracture permeability happens, in which fractures/micro-fracks seized or open leading to a slope discontinuity at the critical effective stress. He considered the effect of slope discontinuity at a critical effective stress in his calculation and indicated that correlating pressurizing/de-pressurizing data using same equation for a whole range of data is not accurate. He noted to correlate data separately over the regions below and above the critical effective stress. This is due to the different role of fracture in the hysteresis path before and after critical effective stress (Civan, 2017).

In this work, permeability hysteresis and damage over the tight formation, Bakken, Williston Basin, ND are investigated. Confining pressure and pore pressure are applied to two different pore size Middle Bakken core samples and measured permeability using the pulse decay method. Digital rock physics (DRP) was used to extract information on the rock structure and pore-size distribution (PSD) of the Bakken samples. Porosity and absolute permeability in non-confined reservoir condition were determined. Then, pulse decay method for permeability and Mercury injection capillary injection (MICP) data for PSD was used to validate our procedure and the obtained properties. Based on laboratory measurements, it is illustrated the influence of stress loading/unloading and effect of pore pressure, stress range and pore size distribution on permeability damage for Middle-Bakken core samples. Permeability damage and average permeability damage for whole data sets, before and after critical point are calculated. Mathematical models such as exponential and power law models are used to fit to the experimental results and facilitate permeability damage calculation. This approach can help to get a better insight into the impact of mentioned parameters on permeability hysteresis path and permeability evolution under different effective stress by considering critical points.

3.2. Description of Rock Sample

Three Middle Bakken core samples were drilled from Mountrail County, Williston Basin, ND. Raw samples were selected from well#24779, Sanish filed, provided by University of North Dakota core library (Figures 3-1 (a) and (b)), for the current study. In most area of Bakken Formation, Middle Bakken formation is bounded above by shale member of Bakken, Upper Bakken and below by Lower Bakken. The fine-grained clastics and carbonates of the Middle

Bakken core samples are representative of a tight, fractured rocks that count as main path of fluid transmitting in reservoirs. The Middle Bakken Member typically comprises between three and seven distinctly different lithofacies that range from silty carbonates to calcite/dolomite-cemented siltstones and light to medium gray in color (Sorensen et al., 2017).

The rock samples for this study were taken from depths between 3120 to 3123.5 m. Selected samples were cut cylindrically by a laboratory coring machine using 20- and 25-mm drill bit (cooling with water), with smooth ends by polishing machine (Figure 3-1 (c)). Based on North Dakota Industrial Commission core data, conventional plug analysis within selected depth shows porosity varies from 2.77 to 8.31%, and air permeability ranges from 10^{-3} to 10^{-2} md (measured under 5 MPa net confining pressure) and average grain density of 2.7 g/cm^3. To ensure we are measuring intact core samples, plug sampling was performed carefully with minimum micro-crack creation. This is important because if core sample contains fractures in which two ends of sample connect to each other, measured permeability would not represent matrix permeability (Gan et al., 2018). Before starting experiments, samples were cleaned, and oven dried at 60 ºC for more than a week. The core plug samples are shown in Figure 3-1 (c). Also, two samples with sample lengths less than 3 mm were selected for Micro-CT/SEM observation after permeability experiments.

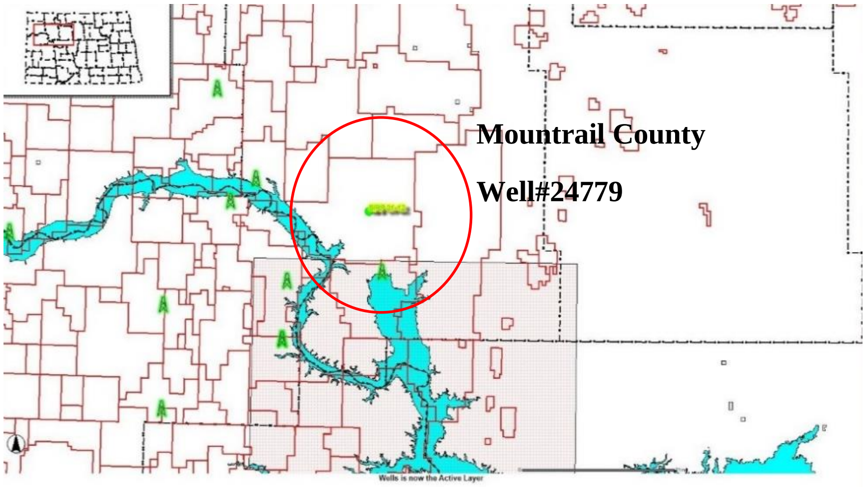
Mountrail County
Well#24779
Wells is now the Active Layer

(a)

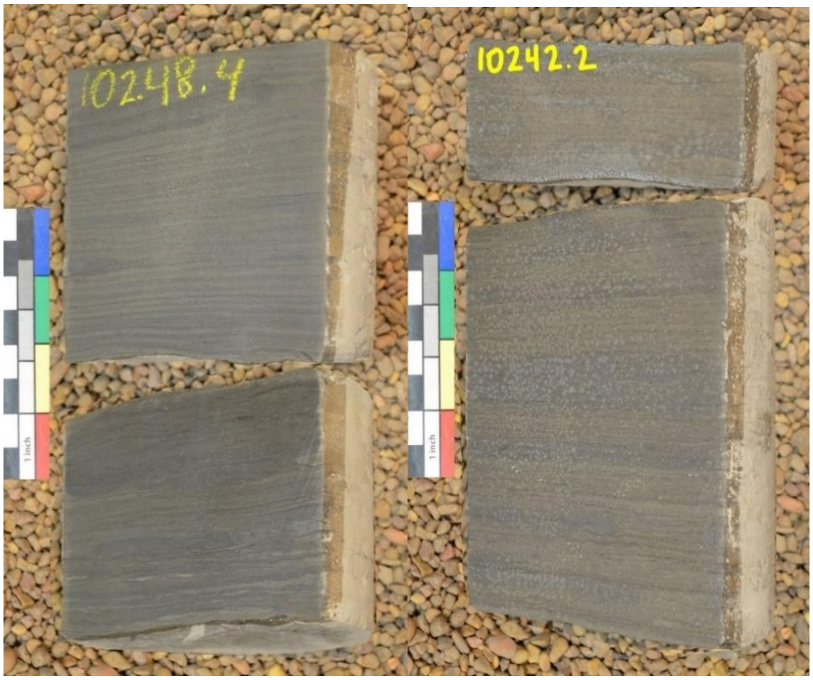
10248.4
10242.2
1 inch
1 inch

(b)

(c)

Fig. 3-1. Middle Bakken core samples used in this study (a) Sampling well location, Mountrail County (b) Raw core samples (c) Prepared core samples

3.3. Permeability Measurement

The equipment used for the measurements in this study is a servo-hydraulic operated system for triaxial measurements with software controlled arbitrary stress paths on rock specimens up to 50.8 mm (2.0 in.) in diameter at in situ reservoir-stress conditions, pore pressure, and temperature. It can measure permeability under steady state and different transient methods, consisting of three main components: (i) Pressure vessels and four associated pressure intensifiers (ii) Electronics and control panel (iii) Computer system to analyze data. The core samples are cleaned through a vacuum process before running the tests. It is an essential task since the permeability is sensitive to core cleaning. Figure 3-2 illustrates the configuration of permeability measurement apparatus. To obtain more accurate data points, the experiments for each core sample were repeated at least 3 times (Assady et al., 2019).

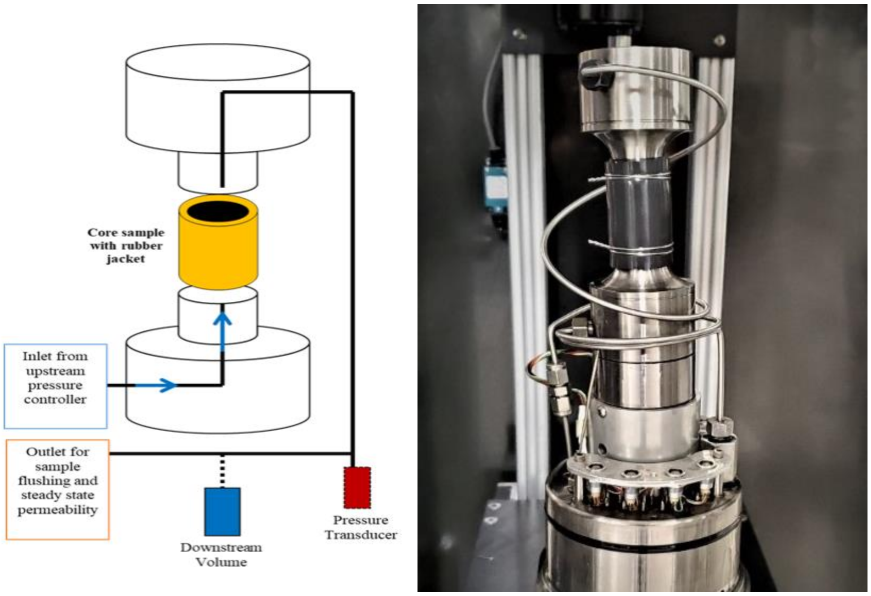

(a) (b)

Fig. 3-2 (a) Configuration of permeability measurement apparatus (b) Permeability measurement assembly (Assady et al., 2019)

The sample in the core holder communicates with both upstream and downstream reservoirs and the system is initially at equilibrium with uniform pressure. When a pressure pulse (disturbance) is applied at the upstream reservoir, it propagates through the core, travels towards the downstream reservoir while it decays over time. The decay profile depends on the characteristics of the core sample; on parameters, such as permeability, size of the sample, volumes of upstream and downstream reservoirs, and pore-fluid properties. The decay characteristics of the pressure are used to determine the reservoir permeability by analyzing the pressure behavior through the core sample given by the mathematical model of permeability in Figure 3-3:

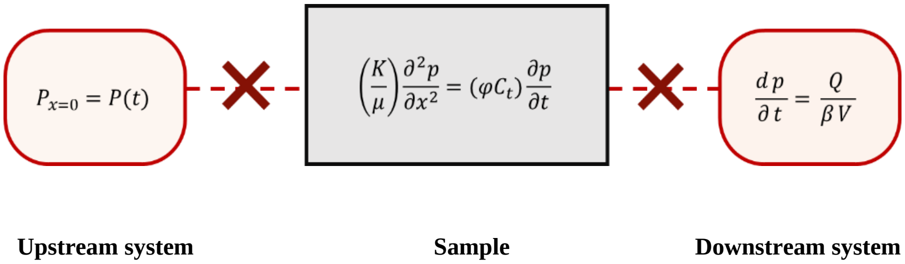

Fig. 3-3. Boundary condition applied in pulse-decay configuration (from left to right Eq. (3-1), (3-2) and (3-3))

Where "*P*" is the pressure (MPa), "*x*" is the distance along the length of the measured rock sample (in.), *k* is the permeability of the measured rock sample (μm^2), "*μ*" is the dynamic viscosity of the fluid (10^{-3} Pa.s), "*φ*" is the porosity, "C_t" is the total compression coefficient (MPa^{-1}). With boundary condition:

$$\frac{dp}{\partial t} = \frac{Q}{\beta V_2} \tag{3-4}$$

Also, "*β*" is fluid compressibility (MPa^{-1}), based on Figure 3-3. Since the medium in this experiment is tight, Jones' method is applied by Auto-Lab software to reduce the permeability measurement time (Jones, 1997). Jones' method is a simplification of a mathematical model for the transient pulse method. The analytical solution of the permeability turned to Eq. (3-5):

$$\alpha = \frac{fkA}{\mu\beta L}\left[\frac{1}{V_1} + \frac{1}{V_2}\right] \tag{3-5}$$

Where "*f*" is a factor as $f=\theta_m/(a+b)$; "*a*" and "*b*" are the ratio of core sample pore volume to up stream (Vs/V_1) and down stream volume (Vs/V_2), respectively. "θ_m" is refered to the root of following Eq. (3-6):

$$\tan\theta = \frac{(a+b)\theta}{\theta^2 - ab} \tag{3-6}$$

After reaching the desired confining and pore pressure, a pressure pulse (i.e., increase upstream pore pressure) would apply to core sample. By observing the response at downstream reservoirs, the permeability can be computed by fitting the response to the analytical solutions (Figure 3-4) (Van Oort, 1994; Zhou et al., 2016). In this work, each permeability experiment at specified effective stress, ran at injection rate of 0.1 cm^3 /min. The test will be proceed to next data point after observing pressure stabilization in the core samples.

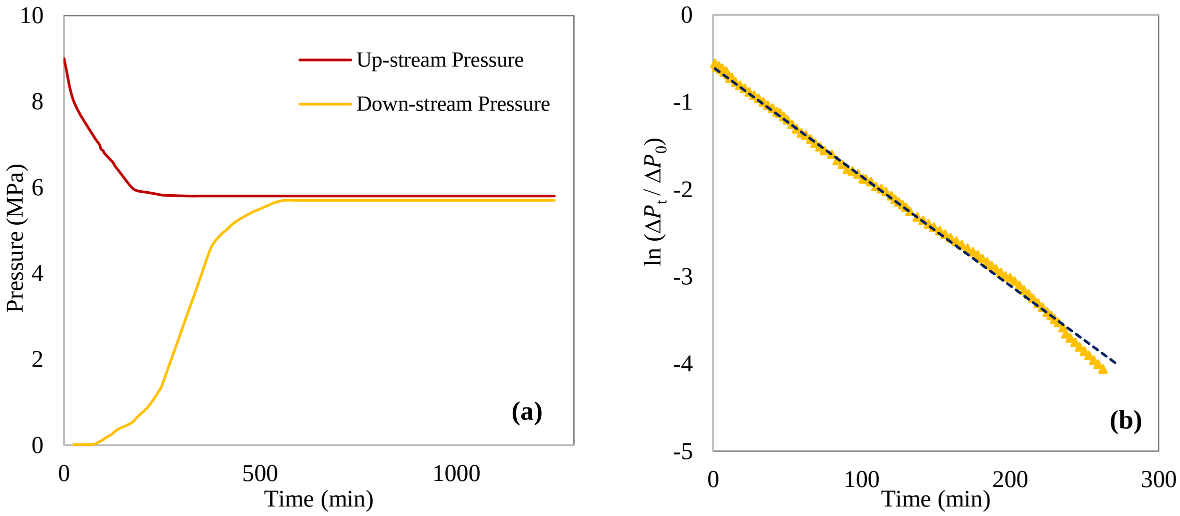

Fig. 3-4. An example of pulse decay analysis for Middle Bakken core sample (a) Changes of the upstream and downstream pressure during experiment (b) ln ($\Delta P_t / \Delta P_0$) vs. time plot

3.3.1. Permeability Measurement Validation

To validate the permeability measurement using pulse decay method, a steady state experiment for a Middle Bakken core sample was ran and compared the measured permeabilities (Assady et al., 2019). This method requires two pore pressure intensifiers with automated recycling in order to create identical upstream and downstream pressures on both opposite ends of the core plug. The two pumps in the experimental setup use distilled water as the pore fluid. Each test was performed by applying different confining pressures under a low pore pressure. This is because the higher the pore pressure, the longer it takes for pore pressure to reach equilibration. The major issue with steady-state method is the long time that it takes for pressure stabilization. For the samples used in this work, it took almost 7 days for the stabilization period. Then, the permeability was measured based on Darcy's Law vs. time as shown in Figure 3-5. The permeability is normally estimated as the average during the plateau when the permeability trend flattens and stops fluctuating.

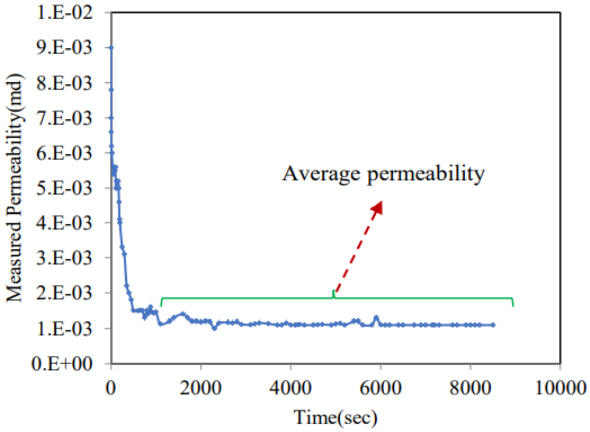

Fig. 3-5. Steady-state permeability measurement (Assady et al., 2019)

Although the steady-state permeability measurement is the most accurate, it seems not to be a method of choice for tight core samples (Li et al., 2015). Aside from being an expensive test, running steady state experiment is time consuming and requires days and a month to achieve few data points. Moreover, long time downstream and upstream pressure equalization become harder with increasing confining and pore pressure (Morrow et al., 2014; Assady et al., 2019). That being said, only five permeability values under limited effective stress ranges were determined (e.g., 6.8, 7, 7.5, 17.2 and 25 MPa) due to time consuming procedure (Assady et al., 2019). This helped us to validate and crosscheck the results obtained from pulse-decay method under same condition, which as Figure 3-6, it confirms that the pulse decay method results under this range is consistent with steady state permeability values.

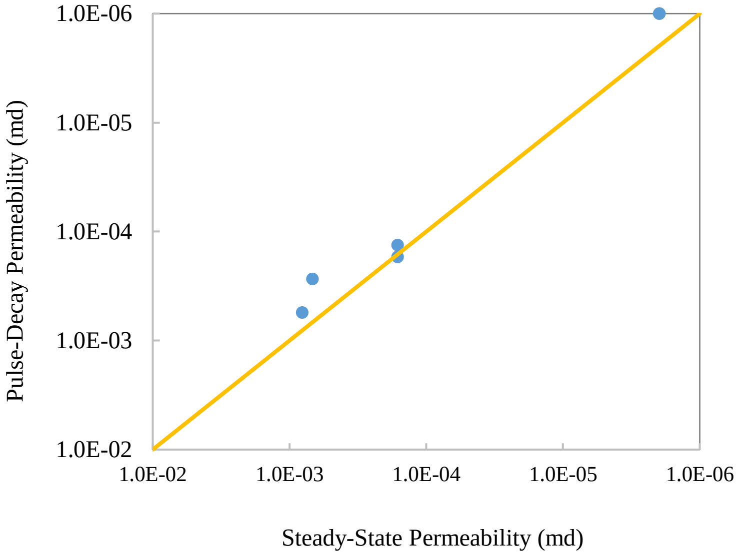

Fig. 3-6. Measured permeability using steady-state and pulse-decay methods

Therefore, the employed pulse-decay method is preferable— especially for our tight core samples— as it is quick, affordable, and economic if compared with steady-state method. To facilitate the experiments regarding to required time, this work will be continued using pulse decay permeability measurement.

3.4. Digital Rock Analysis

As Civan (2000) and other researchers mentioned in their studies, among different types of pores (i.e., interconnected pores, dead-end pores, and isolated pores), fluid transport occurs only in interconnected pores. Consequently, measuring the interconnecting pores or effective porosity, and its impact on permeability, is an essential task. In addition, permeability depends on the capability of fluid transport of both the interconnected pores and micro-cracks. Therefore, the permeability variation trends versus effective stress for interconnected pores and micro-cracks are not equal (Sigal 2002). Obtaining petro-physical properties for reservoirs with small pore sizes, is important for analyzing the porous medium behavior and future oil pattern design (Assady and Jabbari 2020).

In this study, micro-CT Bakken core samples were characterized using digital rock physics to extract pore size distribution and effective porosity. The digital rock approach (DRA) can provide a great amount of data in a short time specifically in ultra-low permeability reservoirs (Bautista. et al., 2018). Digital rock analysis is a powerful tool which cannot only reduce the necessity of the use of conventional core samples, but also can readily capture pore geometries, fluid flow behavior and helps to have better internal vision of rock structure. First, rock properties (e.g., porosity, and pore size distribution) were calculated. Then, absolute permeability was obtained and compared with the available experimental data (e.g., pulse decay, steady state). Since the Bakken samples contain nano to meso size pores, image analysis requires high accuracy and iteration to get the exact binary images. Thomson et al., 2018, provided a detailed recipe for image processing, characterizing pore network geometry, and determining the permeability through connected pore space for Fontainebleau and Berea Sandstones.

To get the validated pore size distribution from reconstructed 3D volume of core samples, pre-processed the images, by removing noises and artifacts was performed. Then grains and pores are separated using commercial DRA software. Segmentation (i.e., binarization) of sample images are crucial step in characterizing pores to extract the geometrical information of all individual pores inside the 3-D domain. Accurate segmentation can be defined as extracting isolated individual phases with same brightness and color (Thomson et al., 2018). Thresholding visually, manually, and automatically based on the image gray scale values was utilized and tuned to get the closest match by checking the results. For doing so different algorithms based on computational analysis and different common methods for image analyzing were used. For some type of stacks with similar density for pores and organic matters, simple thresholding can cause error for adequate pore/grain separation. To reduce this error, it recommended by many authors to use marker-based water-shed segmentation to enhance labeling the image (Cudjoe et al., 2019). The major idea of water-shed segmentation is based on the concept of topographic representation of image intensity (Gonzales and Woods 2002; Seanger et al., 2011). The concept behind this algorithm is to simulate the flooding from a set of labeled regions in 3D images. After completing pre-processing and processing steps (i.e., various filtering, de-noising, and segmenting pore/grains) connected pores were identified to extract pore network models for obtaining total and effective porosity, absolute permeability, and pore size distribution.

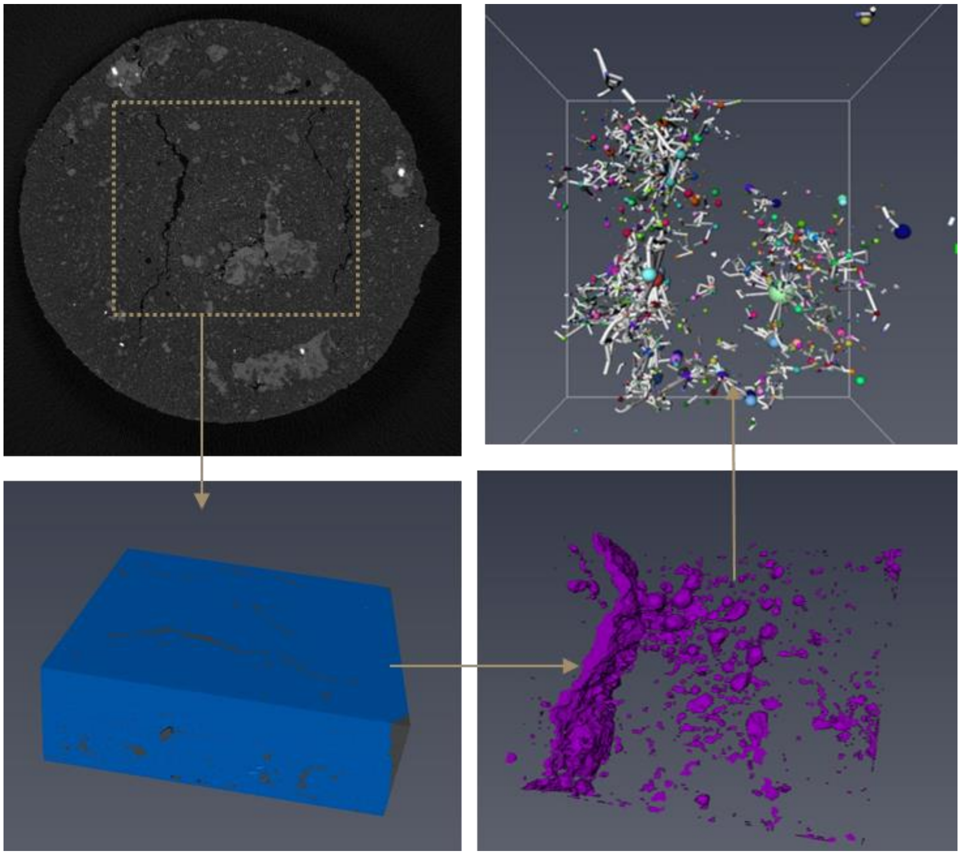

Fig. 3-7 Digital rock analysis procedure; extracting a sub-volume, segmentation, pores, extracting pore network model; core sample#1

The procedure with available data such as MICP and pulse decay results were validated. It is shown that porosity and pore size distribution are consistent with lab results. It implies the segmentation process is reliable. However, permeability is overestimated and does not fully satisfy the lab results. This can be because of the limited region of interest and finite investigated medium, or not capturing all pores during imaging due to improper image scale. Hence, there should be some modification and further investigation for permeability calculation. But in this section, the focus is on obtaining different PSD types. The results are reliable enough to analyze our data. That being said, two different core samples from the Middle Bakken Fm. were considered. After acquiring micro-CT for each core sample, pre-processing and segmenting steps were completed in order to extract required data. Total, connected and isolated pores, for core sample#2 is shown in Figure 3-8. Also, porosity and effective porosity value for each sample are brought in Table 3-1.

Table 3-1 Calculated total and effective porosity

Sample	Pore Volume Fraction	Porosity	Effective Porosity	Experimental Porosity
Case 1	0.063	6.3%	2.4%	5.55%-6.25%
Case 2	0.079017	7.9%	6.5%	

As it can be seen in Figure 3-9, two different types of PSD are dominant, one sample is more homogenous and unimodal, meaning pore sizes are almost in the same range, while the second sample has wide pore size distribution. Also, as the results indicate effective porosity varies from sample 1 to 2. Sample#1 possesses lower effective porosity which implies that fluid transport occurs harder than sample#2. Therefore, it is expected to have lower permeability for sample#1 (Assady and Jabbari 2020).

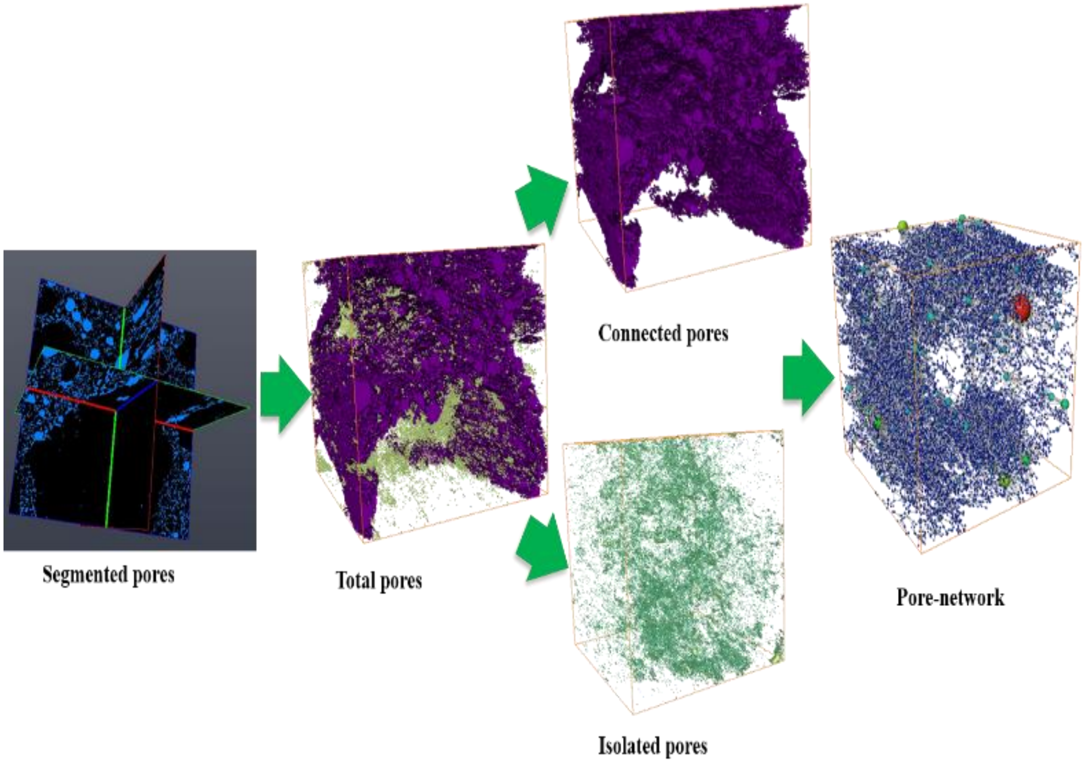

Fig. 3-8. Example of one sub-volume segmentation, total porosity, effective and isolated pores, 3D pore-network; core sample#2

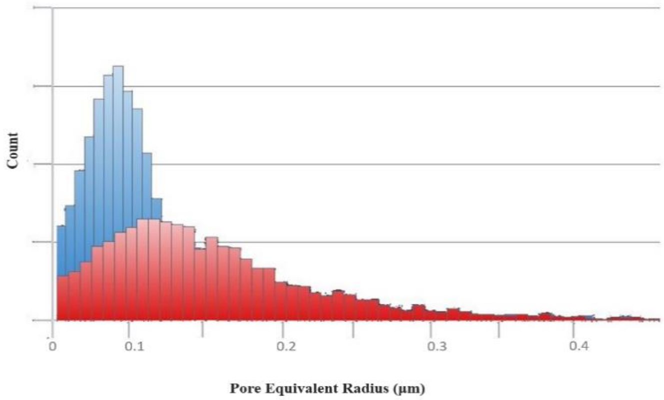

Fig. 3-9. Pore size distribution determined from 3-D pore networks of sample 1 and 2

3.5. Stress-Dependent Permeability

To describe and analyze pressure dependency of permeability, it is important to derive the relationship between permeability and effective stress which would represent reservoir depth.

This is important to analyze and understand essential phenomena such the permeability hysteresis due to its remarked impact on petroleum production (Wang and Civan, 2005). However, due to experimental limitations such as time-consuming tests, cost and limited lab conditions, mathematical models can help to describe and predict the hysteresis phenomenon and rock behavior under reservoir circumstances. This is important to relate rock characteristic in the manner of pressure dependency of reservoir permeability. Although, several complicated processes play a role on permeability hysteresis, such as elastic and plastic deformation, contraction, shearing, compaction and the like, during pressure loading/unloading (Civan, 2017), the most attempts to determine permeability pressure dependency relationship were focused on confining pressure. This is due to large impact of confining pressure on permeability alteration in noticeably short time. Permeability dependence on effective stress change (σ_{eff}) is well known in the geomechanics area. Specifically, most of the permeability experiments for Bakken core samples showed this significant effect on the reservoir permeability by changing confining and pore pressures. Existing ultra-small pore sizes in tight core samples such as Bakken cores can cause high effective stress sensitivity of permeability (Dong et al., 2010; Teklu et al., 2016). Therefore, modeling permeability by relating to effective stress was the main focus on numerous studies. Ewy et al., 2012, presented the relationship between permeability and change in pore pressure and effective stress in the form of Eq. (3-7):

$$k = f(P_c - XP_p) \tag{3-7}$$

Where, “P_p” is pore pressure (i.e., internal stress), “P_c” is confining stress (i.e., external stress) and “X” is effective stress coefficient (i.e., Biot’s coefficient) that relates stress and pore pressure. If X is close to 1, then stress alteration will change permeability by the equal and opposite change in pore pressure. Some researchers estimated X to be less than one (David and

Darot, 1989) and others consider it as not to be constant (Warpinski and Teufel, 1992). Generally, X can be greater than one for high pore pressure and lower than one for higher confining pressure. The actual behavior of permeability can be modeled more accurately if measure it under various cases of pore pressure and confining stress (Ma and Zoback, 2016), and then plot it vs. effective stress. For the sake of simplicity and similar to existing experiments on Bakken core samples (Warpinski and Teufel, 1992), Biot's coefficient is considered unity in our calculations. This leads to effective stress as the difference between applied confining pressure and the internal pore pressure (i.e., $\sigma_{eff}=P_c-P_p$) which is known as Terzaghi's effective stress (Terzaghi, 1943).

In general, regardless of the flow direction or type of fluid, a nonlinear reduction in permeability with increasing effective pressure occurs during loading the samples. However, the rate of reduction can vary from sample to sample. This reduction in permeability with increasing effective pressure or the reverse, i.e., increasing permeability with decreasing effective stress (or unloading) can be explained by the flow through microcracks model (Walsh, 1981; Kwon et al., 2004; Metwally and Sondergeld, 2011). Based on the experimental results permeability relationship can be varied to exponential or power-law, depending on the rock sample characteristic. The exponential relationship for the stress dependent permeability based on David et al., 1994, and Evans et al., 1992, is as follows:

$$k = k_0 \exp\left[-\gamma\left(P_c - P_p\right)\right] \tag{3-8}$$

Where "k_0" is permeability under atmospheric pressure and "γ" denotes material constant which can vary between 10^{-3} to 10^{-2} MPa^{-1} depending on the rock type. Eq. (3-8) has the advantage of being mathematically simple, however it is a phenomenological relation without any micromechanical basis (David et al., 1994). On the other hand, a power-law relationship to demonstrate stress dependency of the permeability based on Shi and Wang (1997) can be considered as:

$$k = k_0 (\frac{P_c}{P_p})^{-\lambda} \tag{3-9}$$

In this equation "λ" is representing material constant which can be obtained empirically. Based on Shi and Wang, 1997, and Dong et al., 2010, the λ can change from 0.1 to 2 for different core samples under various effective stress conditions. Therefore, each core sample can show different behavior under variable effective stress, hence modeling the actual behavior of permeability requires plotting permeability under various cases of pore pressure and confining stress vs. effective stress (Ma and Zoback, 2016). Numerous studies used these presented relationships to express permeability-pressure correlation. For instance, Jones & Owens,1980, presented the relationship between the permeability and the effective stress as:

$$(\frac{k}{k_0})^{1/3} = log(\sigma - \alpha P) \tag{3-10}$$

Also, Teklu et al., 2016, suggested the relationship between effective stress and permeability of fractured cores should follow a power-law, based on the laboratory permeability measurements. They presented, a mathematical model to define the hysteresis phenomenon in permeability and employed it in most of their calculations:

$$k = \frac{\mu_g(P_{avg}) c_g(P_{avg}) V_d L}{A} \frac{\Delta \ln(\frac{p^2_{upstream} - p^2_{initial}}{p^2_{upstream} - p^2_{(l,t)}})}{\Delta t} \tag{3-11}$$

Where "L" and "A" are core length and cross-section area, "μ_g" and "c_g" are gas viscosity and compressibility at average pore pressure "P_{avg}" during a time interval Δt. In more recent studies based on Civan's (2011) work, compressibility of matrix, solid and fracture were incorporated in the model he presented. He introduced a novel mathematical formula as Eq. (3-12):

$$k = k_{\infty} + (k_0 - k_{\infty})\left(\frac{\sigma_{eff} - \sigma_{cr}}{\sigma_{eff,0} - \sigma_{cr}}\right)^{A_2(c_0 - c_{\infty})} \tag{3-12}$$

Where "A_2" is an empirical parameter, "k_0" and "k_{∞}" are the permeability at lowest and highest critical effective stresses. The enormously important concept of Civan's work, is critical effective stress which mostly appears in the hysteresis permeability path as a discontinuity. As stated earlier, a slope discontinuity at a critical effective stress during loading/unloading can be attributed to:

(i) opening and closing of micro cracks,
(ii) matrix porosity change beginning to contribute and dominate the fracture porosity change,
(iii) crushing and reorganization of the grains of rocks (Civan, 2017).

Civan, 2017, indicated that ignoring breaking points in developing mathematical relationship between permeability and pressure would cause substantial errors and inapplicable mathematical models for whole data sets. As he mentioned, in different effective stress regions with different deformation mechanism, petrophysical properties need to be modeled, separately (Civan, 2017 and 2018).

Thus, the loading/unloading experimental data are conducted to calculate permeability damage over the whole data, and the two sets of data points. One set of data point lower than the critical effective stress and one higher, to indicate the errors caused by ignoring the discontinuity at a critical effective stress. Also, this can help to provide physical insights into the nature of stress dependency of rock and changing rock deformation mode. In next section the employed approach and average permeability damage concept will be explained.

3.6. Permeability Damage Calculation

To calculate formation damage (i.e., permeability alteration) due to stress changes, we integrated both loading and unloading permeability vs effective stress plots. The difference of the integrated values would give the space gap between two plots representing as permeability evolution. The region above the loading curve would be considered negative since permeability increases. A schematic of damage calculation is shown in Figure 3-10, the shaded area presents the overall permeability damage during a loading/unloading cycle.

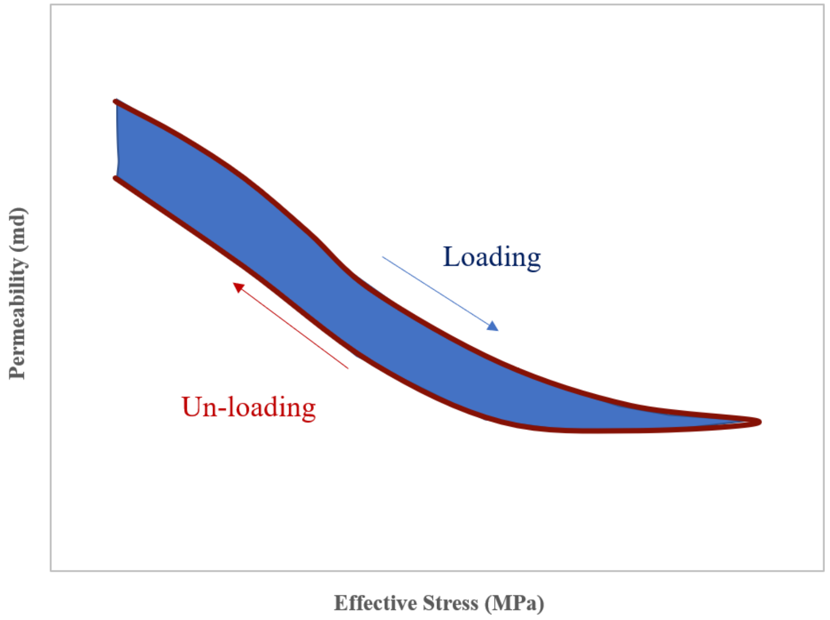

Fig. 3-10. Shaded area between loading and loading path represents permeability evolution

The shaded area for three different regions (Figure 3-11) are measured. First, loading/unloading path with no discontinuity (σ_1 to σ_2) is considered. Second, the curves are separated into two parts including a region before reaching to critical point (σ_1 to σ_{cr}) and after the critical point (σ_{cr} to σ_2) region. Then average damages for each region are compared to check the results with and without considering the breaking points on loading/unloading paths. Also, this will help to shed light on the pressure dependency permeability before and after approaching the critical effective stress, where it is expected that majority of microcracks and pore alterations happen (Civan, 2017).

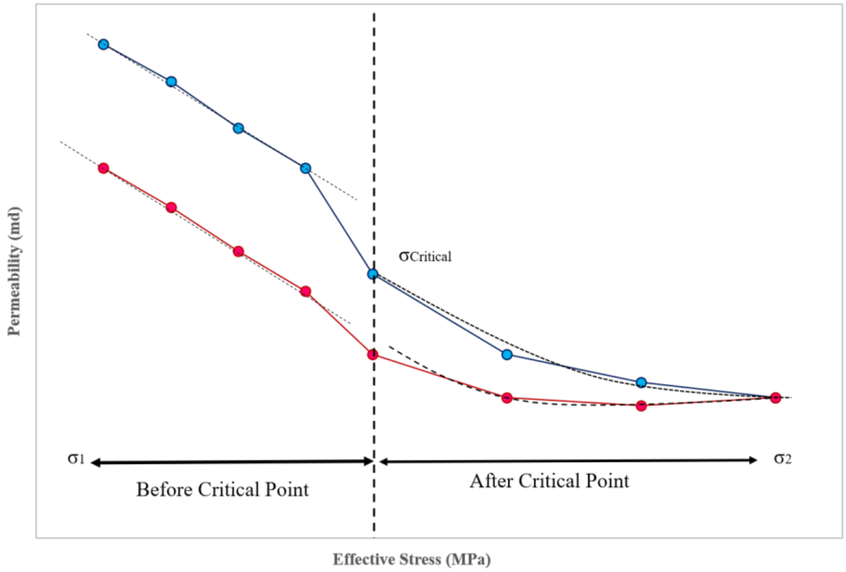

Fig. 3-11 Dividing permeability hysteresis path to two separated regions; before and after critical effective stress

Furthermore, two common curve fitting methods in permeability hysteresis calculation, power law and exponential (Dong et al., 2010), are employed. Thereby, formation damage calculation using each proposed matched curve and results validation with real damage measured during the loading/unloading path are performed. The real damage value is defined as area under a plotted curve with trapezoidal rule. The better fitted model will help us to analyze different experiment cases (e.g., hysteresis length, pore pressure and pore size distribution) and be able to predict the damage under higher effective stress ranges. To compare the results, average permeability damage concept based on Fan and Liu, 2019, was used to illustrate permeability evolution under investigated experimental cases. They introduced an average permeability damage concept to show the effects of maximum stress, loading path, holding time, and gas type on coal permeability alteration. Average permeability damage represents the average effect of unit stress on permeability within loading/unloading stress range. This can be calculated based on the Eq. (3-13) to determine the area of shaded region shown in Figure 3-10 (Fan and Lui, 2019).

$$k_d = \frac{\int_{\sigma_1}^{\sigma_2} k_l \, d\sigma - \int_{\sigma_1}^{\sigma_2} k_{ul} \, d\sigma}{\sigma_2 - \sigma_1} \tag{3-13}$$

Where "k_d" is average permeability damage during the cyclic loading range from σ_1 to σ_2; σ_1 is initial applied stress which in this study has different values depend on the experimental cases (5 MPa, 12 MPa), σ_2 is maximum stress at each period, "k_l" is permeability during loading process; and "k_{ul}" is permeability during the unloading process.

To calculate permeability alteration using fitted curves, core sample#2 from 5 to 55 MPa with 0.1 MPa pore pressure was pressurized/de-pressurized and plotted measured permeability on semi-log plot as shown in Figure 3-11. The curve discontinuity found on this graph is almost 25 MPa, which this pressure was picked as critical effective stress point (σ_{cr}) for this core sample with no pore pressure. As showed in Figure 3-11 the curve divided into two regions and four curves:1) Loading before critical point; 2) Loading after critical point; 3) Un-loading before critical point and; 4) Un-loading after critical point. Therefore, permeability damage based on Figure 3-11 can be split to two regions: a) Shaded area between σ_1=5 MPa to σ_{cr}=25 MPa loading/unloading path and; b) Shaded area between σ_2=55 MPa to σ_{cr}=25 MPa loading/unloading path. First, permeability damage based on Figure 3-10 and trapezoidal rule for whole continuous loading/unloading curve, before and after critical point regions calculated to validate mathematical models presented in next step. Determined permeability damages for three mentioned regions are 0.0041 md, 0.0032 md and 0.00085 md, respectively. Next, the best match to the data points were found by applying exponential and power-law method as shown in Figure 3-12 and Table 3-2.

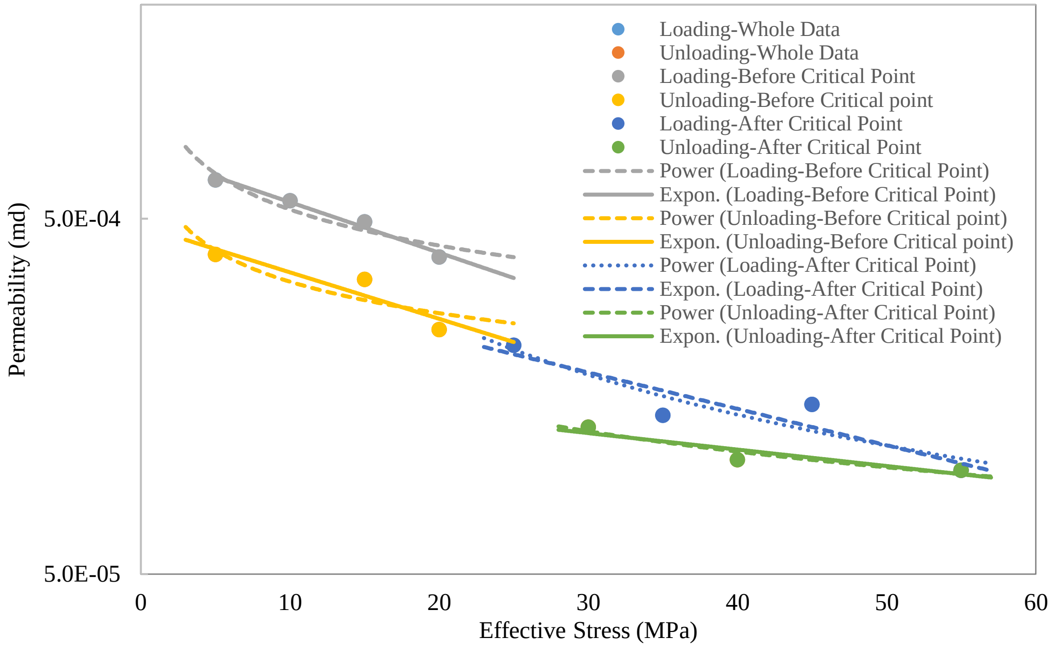

Fig. 3-12. Exponential and power-law models fitted to first experiment data points for core-sample#2 with no pore pressure effect. Each model is fitted to the loading and unloading curves divided into two regions: before and after critical point (25MPa)

Table 3-2 Summary of fitted curves for whole data sets, before and after critical point

	Exponential Method					
	Whole		Before critical		After critical	
	Loading	Unloading	Loading	Unloading	Loading	Unloading
K_0	0.0008	0.0005	0.0009	0.0005	0.0004	0.0002
ɣ	-0.04	-0.032	-0.04	-0.029	-0.024	-0.011
R^2	$R^2 = 0.9324$	$R^2 = 0.8897$	$R^2 = 0.9756$	$R^2 = 0.8594$	$R^2 = 0.843$	$R^2 = 0.8488$

	Power-law Method					
	Whole		Before critical		After critical	
	Loading	Unloading	Loading	Unloading	Loading	Unloading
K_o	0.0035	0.0014	0.0012	0.0007	0.0038	0.0006
λ	-0.841	-0.663	-0.337	-0.294	-0.896	-0.457
R^2	$R^2 = 0.8812$	$R^2 = 0.8573$	$R^2 = 0.8993$	$R^2 = 0.7532$	$R^2 = 0.8459$	$R^2 = 0.9048$

Integrating matched curve models with Eq. (3-13), we compared final average permeability damage within experiment effective stress range for whole data sets, before and after critical point using exponential, power law and real permeability damage. Figure 3-13 illustrates calculated average permeability damage for each proposed method.

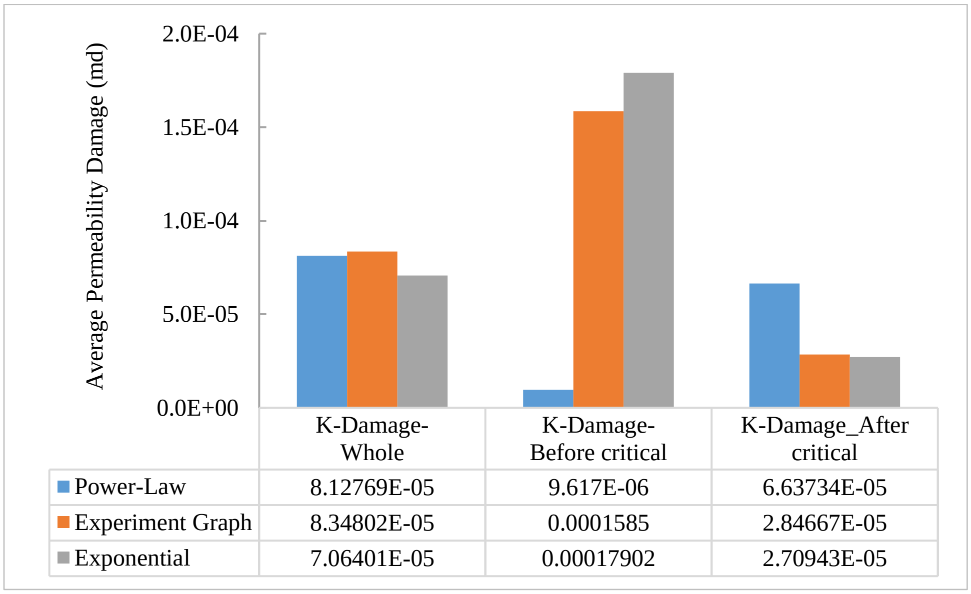

	K-Damage-Whole	K-Damage-Before critical	K-Damage_After critical
🟦 Power-Law	8.12769E-05	9.617E-06	6.63734E-05
🟧 Experiment Graph	8.34802E-05	0.0001585	2.84667E-05
⬜ Exponential	7.06401E-05	0.00017902	2.70943E-05

Fig. 3-13. Average permeability damage: power-law match, exponential match, experiment graph, based on the loading/unloading curve (5 to 55 MPa) for core sample#2

Based on Figure 3-13, although power-law shows acceptable average damage for whole data sets compared to real value, it gives wrong trend and high error in both, before and after breaking points damage. However exponential relationship gives reasonably close value to the calculated experimental average damage in all three investigated regions during loading/unloading. Therefore, based on our laboratory work, for our core samples, exponential relationship is superior to power-law method for describing the stress dependency of permeability of the rock samples and further average permeability calculations. That being said, the rest of the experiment data analysis will be based on exponential curve matching.

3.7. Experiments and Results

3.7.1 Stress Range

In the first set of experiments on core sample#2, the sample was pressurized up to 20 MPa and depressurized to 5 MPa with zero pore pressure (0.1 MPa). Based on Figure 3-14, it can be seen that during loading the confining pressure, permeability decreased around 50%, and after unloading 33% of permeability remained irreversible. Then loading pressure was increased up to 55 MPa, which is close to the in-situ reservoir condition. Figure 3-14 indicates permeability reduction to 82%, and around 38% of permeability remained irreversible. This experiment suggests that the length of pressurizing has a slight effect on hysteresis path. It can be concluded that as the effective stress goes higher, the probability of closing cracks and fractures increase, and this phenomenon makes fractures opening harder. In other words, formation damage directly increases with effective stress, and consequently permeability hysteresis becomes larger. Also, after loading to 55MPa, the critical effective stress point (or discontinuity in data points) is observed to be appeared in this experiment. Based on Figure 3-14, at the beginning of pressure loading there is a sharp permeability decrease, but this reduction will be smooth after a certain increasing value. After reaching critical point (which in our case is around 25 MPa) there will be less closing micro cracks, and permeability reduction lowers to around 20%, while this value before the critical point is around 78%. So, most changes for permeability occur before reaching the critical point. Besides, after approaching this point, the hysteresis path will not change significantly. This implies that significant stress dependency for core sample#2 should occur below 25 MPa. As explained earlier, and based on David et al., 1994, basically there are two important dominant mechanisms during loading/unloading the cores:

(i) Compaction process and its opposite impact on permeability alteration with increasing the effective stress. Grain re-arrangement, pore space collapsing, clogged pore throat with debris or closed induced microcracks during the operation are the main ones (Zhang et al., 1990a; David et al., 1994; Dong et al., 2010; Civan, 2017). After fracture pore or micro-crack deformation occurs, a dramatic decrease in permeability would appear as a discontinuity in data points. The only physical process which cause permeability reduction above the critical point, is matrix deformation which can be controlled by the pore shape and size (Teklu et al., 2016).

(ii) Permeability enhancement due to existent micro cracks expansion or creating new ones under applied stress.

The net effect of these two mechanisms would appear during the experiment. That being said, the observed permeability reduction in our tests, suggests the first mechanism is the dominant in our core samples.

To show this rock behavior in more details, permeability damage based on the Eq. (3-13) and exponential fitted model to data points were calculated (Figures 3-15 and 3-16). As it was mentioned, in the first set of experiments, hysteresis length performed in short and long stress range. In the shorter stress range, the employed effective stress range (5 to 20 MPa) did not exceed the critical point. As it is expected permeability damage would increase with increasing effective stress range, however, after reaching the critical point of the core sample, the damage increment will lessen. In the experiment with the shorter pressure cycle without reaching the critical point, the average permeability damage was determined to be 0.000109 md. For long hysteresis cycle, as it is illustrated in Figure 3-17, permeability damage before critical stress is slightly higher than the short one (0.00017 md), while damage decreases noticeably to 2.7×10^{-5}

md after reaching the critical point. In other words, high portion of the permeability damage (i.e., irreversible permeability) belongs to permeability changes before approaching the breaking point where the majority of rock closure happens.

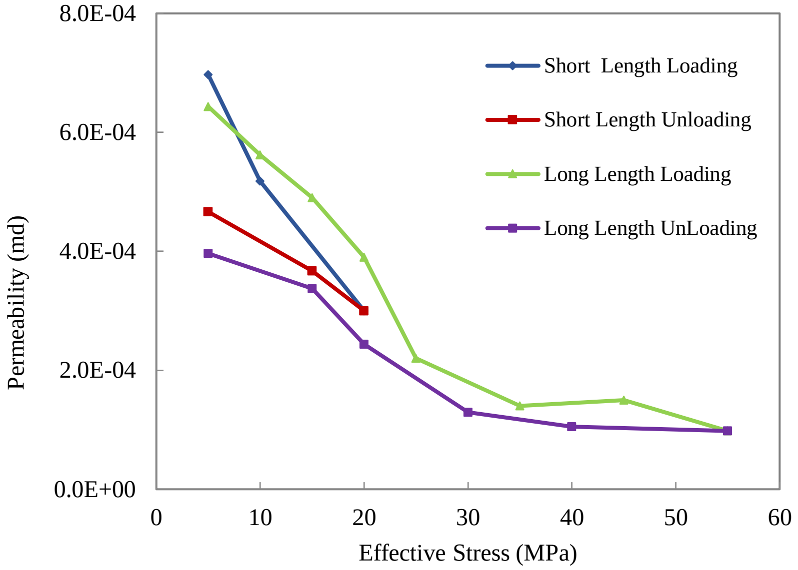

Fig. 3-14. Comparing long and short loading/unloading pressure

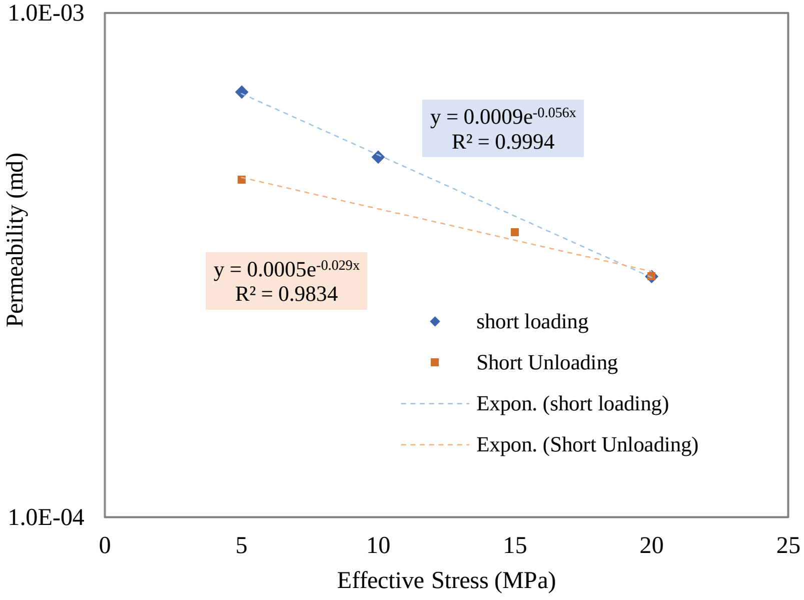

Fig. 3-15. Short length stress loading/unloading and exponential fitted model

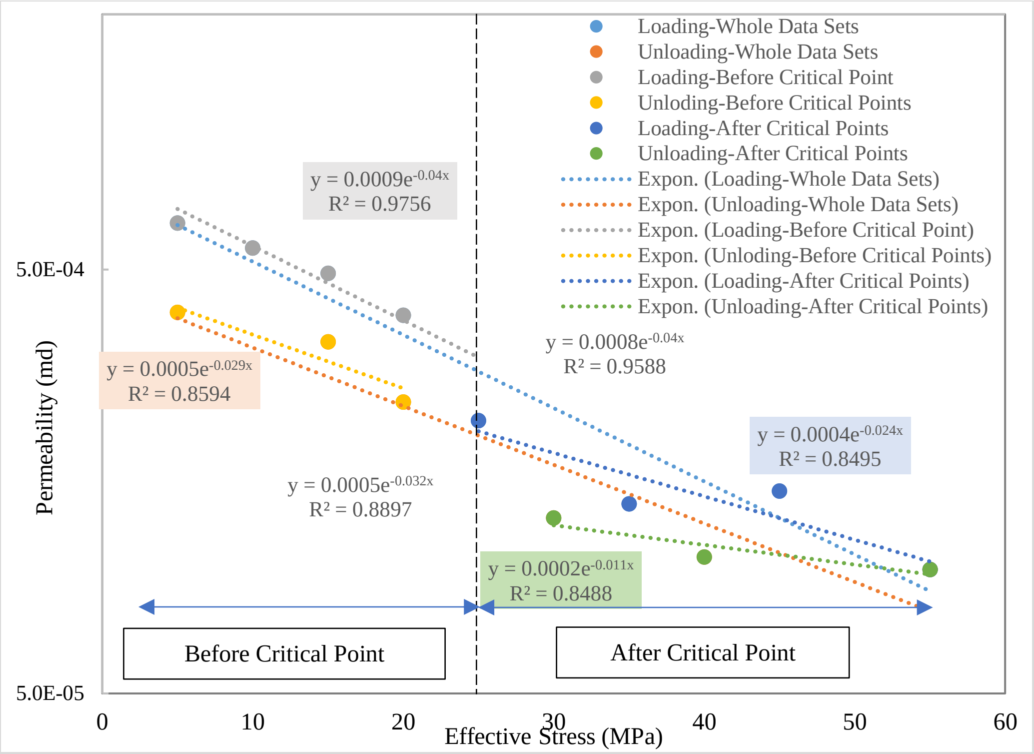

Fig. 3-16. Dividing the data points into two regions and fitting exponential model on semi-log plot; core sample#2

Another important point arises when continuous whole data set in permeability relationship was used to calculate average damage within the applied stress range. Based on Figure 3-17, at first glance it appears the average damage for shorter loading/unloading path is higher compared to longer stress range. However, since in short length hysteresis, the rock does not approach its critical effective stress, it should be compared with permeability damage at maximum critical point (i.e., 25 MPa for our test).

Furthermore, in Figure 3-17 the calculated average damage for the whole data sets within the long pressure cycle case appear to be lower than the short one. The result is not consistent with our experiment permeability curves in which the damage within the short stress range is lower than the long case. This invalid calculated damage can happen when data sets are not separated based on the plot discontinuity. Hence it shows the wrong application of curve fitting with not involving critical point in permeability-pressure models. Consequently, less accurate fitted model with no reliable results leads to high errors in rock behavior calculation and hysteresis effect on permeability evolution.

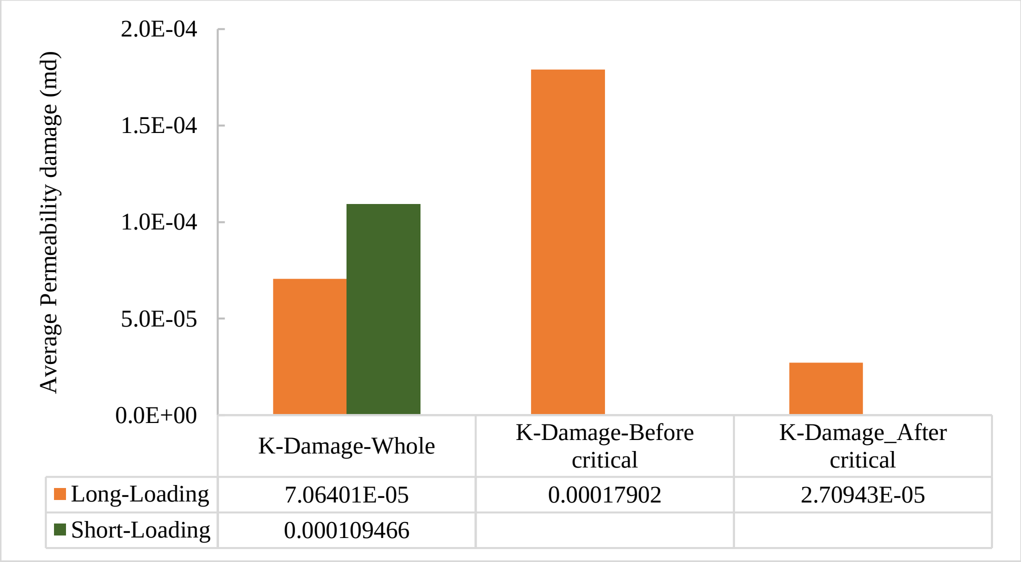

	K-Damage-Whole	K-Damage-Before critical	K-Damage_After critical
🟧 Long-Loading	7.06401E-05	0.00017902	2.70943E-05
🟩 Short-Loading	0.000109466		

Fig. 3-17. Calculated average permeability damage for short and long hysteresis path; core sample#2

Also, this can be explained by comparing the γ values for both loading/unloading paths, illustrated in Figure 3-18. Based on Dong et al., 2010, and Eq. (3-8) the slope of the straight-line in the semi-log plot is proportional to the pressure sensitivity coefficient (γ). In our experiment, γ halved after reaching the critical point where it possesses steeper length and shorter intercept in Figure 3-16. This implies that permeability pressure dependency is not significant after approaching this point and the small amount of damage can only be due to primary deformation (i.e., compacting due to grain movement) and not mechanical deformation or microcrack closures (David et al., 1994; Walsh et al., 1965; Nai and Gang, 2018). Therefore, γ differences for each defined region, are related to the dominant compaction mechanisms.

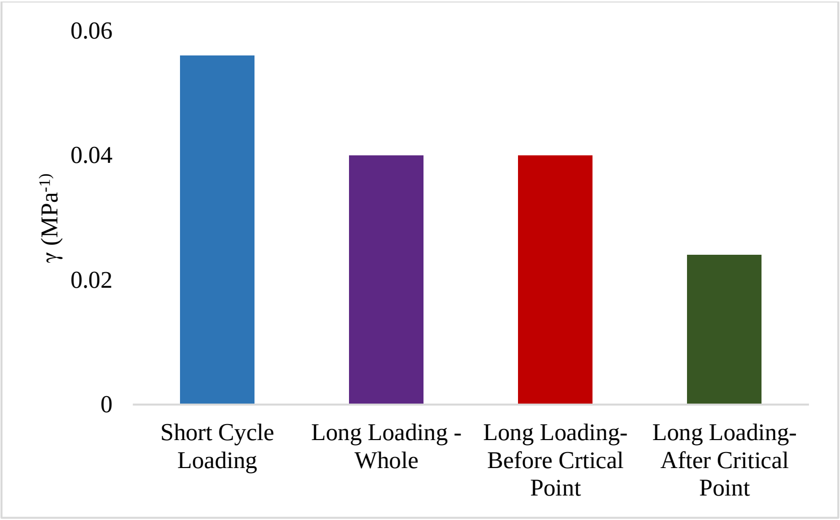

(a)

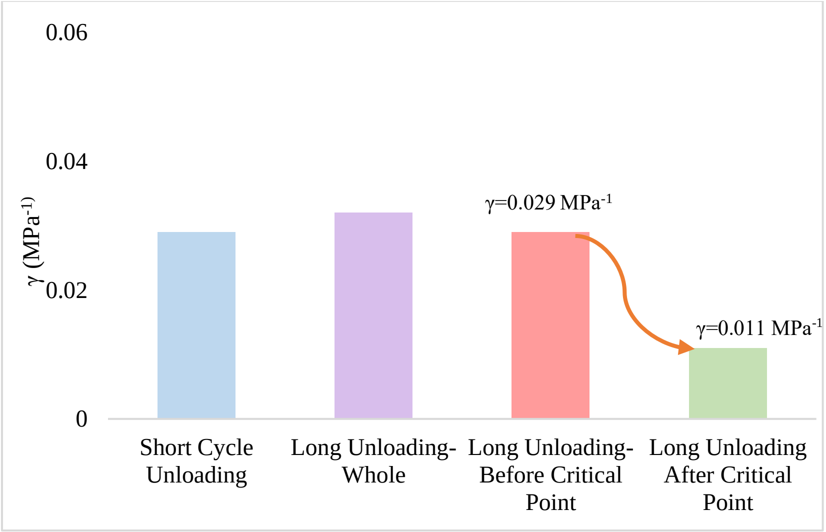

(b)

Fig. 3-18 Material constants for short and long hysteresis paths; (a) Loading (b) Unloading

Another noteworthy point based on sensitivity coefficient (Figures 3-16 and 3-18) is comparing loading and unloading path. Before reaching the critical point, unloading coefficient decreases slightly from loading, which is observable in our data set as permeability hysteresis. Whereas stress sensitivity coefficient, *γ,* after critical point unloading, decreased sharply to almost half value (from 0.029 to 0.011 MPa^{-1}). Comparing to Dong et al (2010)'s introduced range for silty shale, it can be considered as notable low value (i.e., 16.78 to 43.47 $\times 10^{-3}$ MPa^{-1}). This implies decreasing effective stress until certain value cannot retrieve any amount of permeability loss, therefore majority of permeability recovery method by changing pressure (e.g., injection) should be done before reaching the critical point due to the existence of high stress sensitivity before this point.

By comparing pressure dependency for the short hysteresis plot with long one, it implies that, different stress ranges can change the obtained pressure sensitivity coefficient for the same core sample. The impact becomes paramount after reaching the observed discontinuity on plots or effective critical stress. Dong et al., 2010, mentioned if the exponential relationship is used to fit the data points for a lower stress range, γ, will be greater than that obtained from the data points for a higher stress range. Consequently, the experimental stress range plays an important role in determining the parameters of permeability-pressure models. This is due to the existence of critical point where the stress sensitivity can change significantly based on dominant mechanism.

That being said, predicting permeability change using mathematical models requires to run the test under sufficient stress range and achieve the critical point before developing any permeability relationship formula. To show the effect of stress range, predicted permeability damage and hysteresis using short and long cycle equations under 120 MPa effective stress are plotted in Figure 3-19. The predicted model using short stress range relationship, overestimates permeability reduction after reaching to core sample critical point (25 MPa). Also, it does not contain any sharp changes or discontinuity in critical effective stress. This is because high and same pressure dependency coefficient is employed after reaching to core sample critical point. In other words, it does not involve particle crushing and pore collapsing in the compaction mechanisms after critical point which leads to significant error in both predicted permeability and average damage values. Therefore, except an overestimated unloading value between 25 to 60 MPa, permeability reduction become constant in exceptionally low value under higher effective stress than obtained experimental data. Based on predicted permeability hysteresis path for two models, it can be seen from Figure 3-19 that choosing wrong stress range would suggest false high permeability reduction and pressure dependency (γ), after reaching the real critical point. However, employing discrete model after the critical point would predict a significantly slow permeability reduction, which is close to real experimental data.

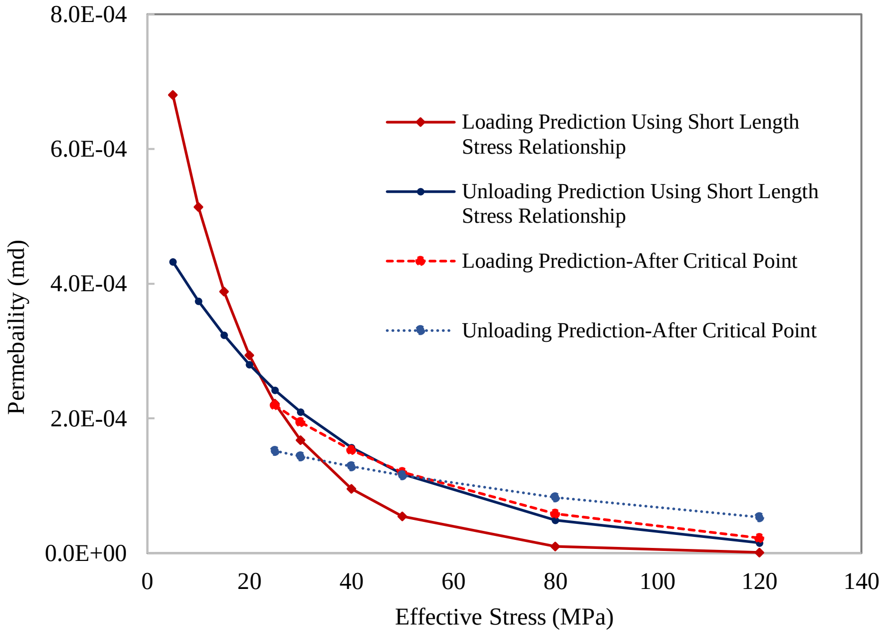

Fig. 3-19. Comparing prediction hysteresis path using short and long length stress exponential relationship

Therefore, it is important to determine exact permeability alteration during loading/unloading under high effective stress, as lab conditions can limit experimental ranges. In case of wrong prediction, due to inaccurate models or insufficient experimental data, it can cause wrong decision for early injection to retrieve the permeability.

Comparing pressure sensitivity coefficients in both exponential and power law method in our experiment stress range shows, power law coefficient predicts the pressure dependency incorrectly and opposite of real behavior of the rock. As it is shown in Figure 3-20 material constants, λ, which represent rock pressure sensitivity (David et al., 1994), increased after critical point for both loading and unloading path. However, as it was illustrated permeability changes after this point is small and insensitive to pressure changes. Therefore, as stated earlier, power-law model for our experiment data cannot represent permeability pressure dependency model.

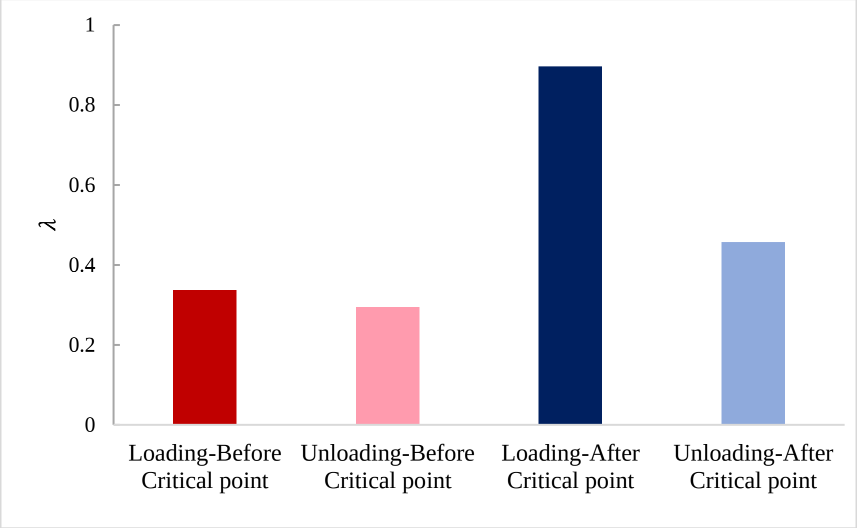

Fig. 3-20. Material constant using power law model

In general, before approaching the critical effective stress on experimental data, high pressure sensitivity and permeability reduction were observed. Based on many researchers work microcrack closure, particle rearrangement, grain crushing, existing pore channels and pore shape are the dominant mechanisms controlling the evolution of rock permeability with the effective confining pressure (Walsh, 1965; David et al., 1994; Kwon et al., 2001). However, rock deformation will become smooth after certain point and mentioned phenomena will not be effective anymore. Therefore, permeability approaches a low and stable value with small changes under elevated effective stress.

Furthermore, pressure dependency can vary depending on the stress range of the experiment. Thus, it is important to find the proper material constant, γ, before developing pressure dependent models. Based on average permeability damage, pressure sensitivity and permeability hysteresis, it is shown that separating the experimental data with respect to critical points are essential for predicting and calculating permeability evolution. Therefore, detecting the critical effective stress for any formation is a necessary task before proceeding with permeability calculation. Indeed, each breaking point differs from one formation to another; hence, it is important to obtain the range of possibility critical stress and ensure reaching the point during permeability hysteresis measurement. In the next experiments we checked the effect of pore pressure and porosity in case of damage, sensitivity and changing critical points.

3.7.2. Pore Pressure

In the second experiment different pore pressures (i.e., zero, low, high) were investigated to check its impact on permeability measurement results during loading/unloading the core sample. It is shown in Figure 3-21, during loading in low effective stress, as pore pressure increases, initial permeability values rise, and pore pressure shows a direct relationship with permeability measurement. However, increasing the effective stress (i.e., higher confining pressure) causes two noticeable changes on the permeability trend:

(i) As it can be seen in Figure 3-21, critical effective stress for same core sample with different pore pressure is almost in the same range (25 to 30 MPa). However, increasing the effective stress with higher pore pressure, would increase permeability reduction rate. Therefore, approaching critical stress point would occur with faster slope and lower permeability value.

(ii) At the beginning of loading, where effective stress is low, higher permeability was measured in elevated pore pressure. However, the effect of pore pressure will be diminished by continued loading. Thus, permeability goes down and the direct relation between pore pressure and permeability switches to opposite. This indicates the significant effect of confining pressure on formation behavior and low impact of pore pressure under high exerted confining pressure.

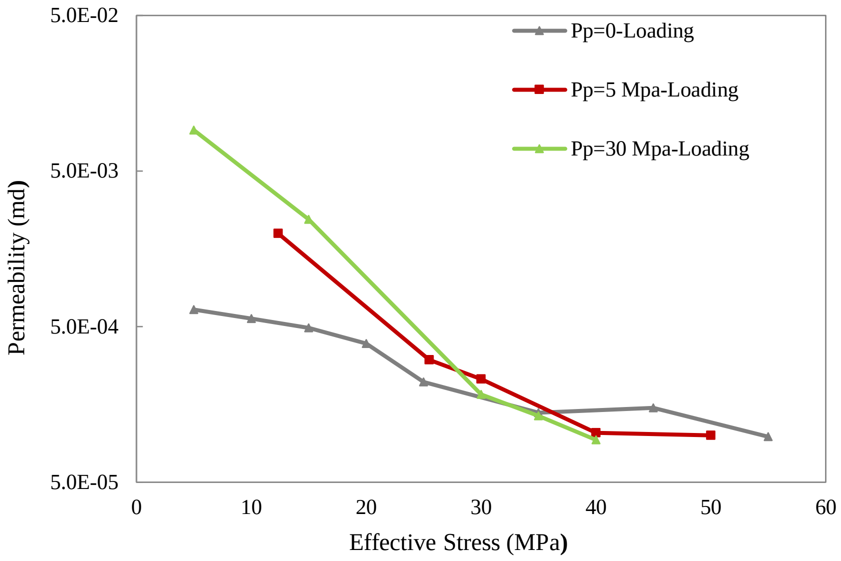

Fig. 3-21**.** Effect of pore pressure during loading the sample

Continuing the test with unloading the sample for various pore pressure amounts, low permeability retrieves for high pore pressure comparing to two other cases (i.e., zero and 5 MPa pore pressure) was observed (Figure 3-22). In other words, pore pressure effect appears in extremely low confining pressure (here is 5 MPa) similar to the loading path, thus average permeability damage expects to be high in presence of pore pressure. Moreover, the results for high pore pressure loading/unloading path suggest that there is a delay in reaching the rock critical effective stress during unloading (Figure 3-24). This behavior is not observed in the presence of low or zero pore pressure.

In Figure 3-23 the results from P_p=30 MPa can be found in more detail. In low effective stress (P_c=35 MPa) permeability ratio during loading/unloading is around 8%, which shows high pore pressure can barely mitigate formation damage, even in low effective stress. The situation exacerbates in higher confining pressure in which pore pressure cannot overcome confining pressure after minor increasing and permeability ratio halved (3.5%).

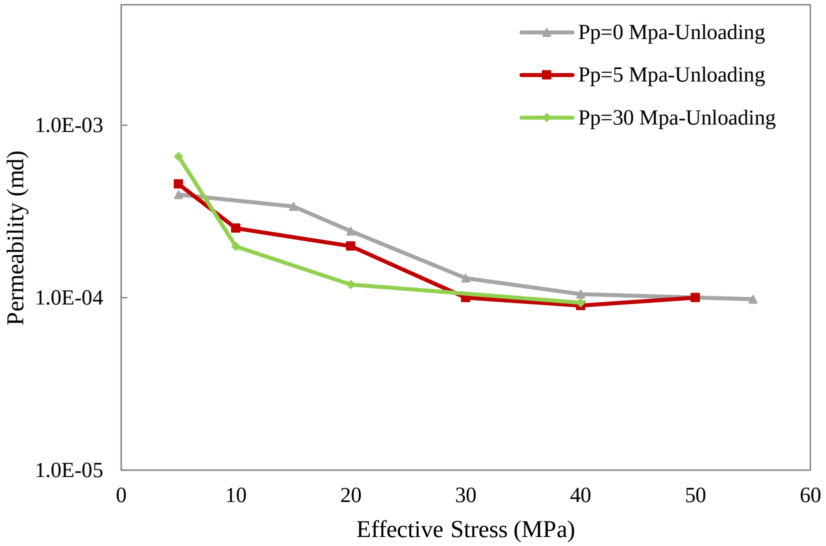

Fig. 3-22. Effect of pore pressure during unloading the sample

As it is appeared in Figure 3-23 there is a noticeable reduction in permeability after unloading the sample in the presence of pore pressure. In this case, the formation damage and permeability hysteresis remarkably increased.

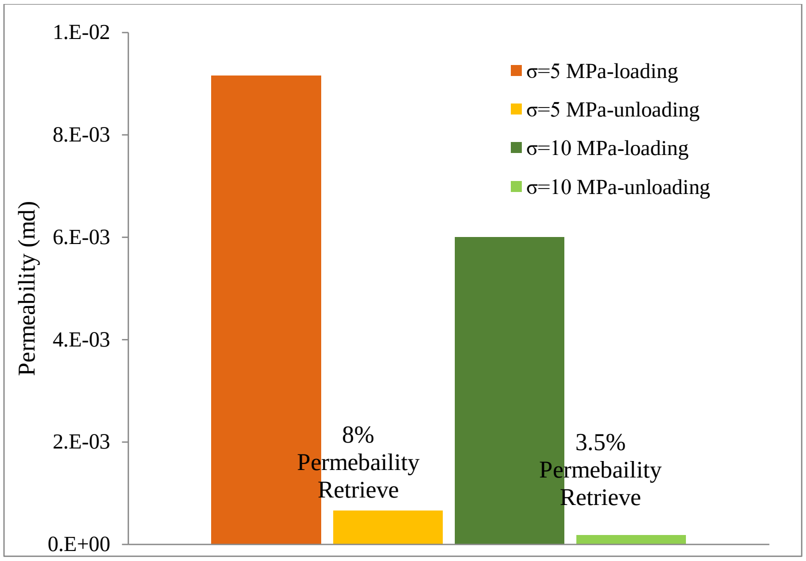

Fig. 3-23. Comparing permeability values for different pore pressure and constant effective stress

To analyze the exact value of permeability damage same as employed approach for stress range section, average permeability concept after fitting data with exponential models was used for both cases with 5 and 30 MPa pore pressure. Thereby, the effect of increasing pore pressure on permeability evolution and pressure sensitivity coefficient can be seen. The average permeability damage for three cases with zero, 5 and 30 MPa on Figure 3-25 are compared. It can be seen that as pore pressure increases, permeability damage before reaching the critical point, increases to significantly higher value. Average permeability damage for pore pressure with 30 MPa is almost 0.002 md, comparing to 0.00074 and 0.00017 md for P_p=5MPa and zero, respectively, is one order higher. This high negative effect of pore pressure can be related to the observed delay in reaching critical point after unloading the sample as shown in Figure 3-24. This can be possibly explained by creep unloading behavior of rock, which becomes noticeable in presence of significant water. Considering the permeability measured using distilled water, one possible explanation for the lower permeability is the swelling of clay in the presence of water which leads to gradually permeability recovery or creep unloading (De Jong et al., 2014; Noort and Yarushina, 2018).

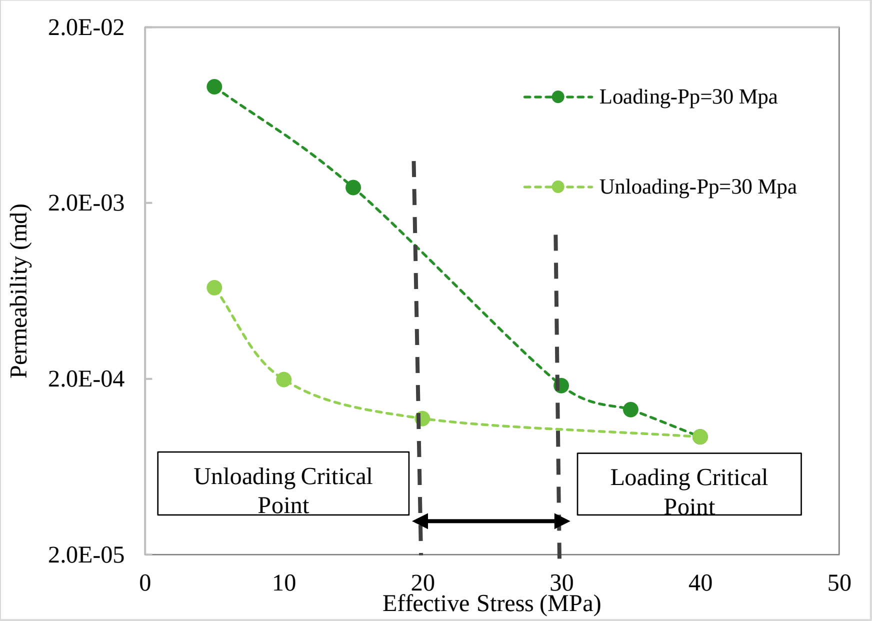

(a)

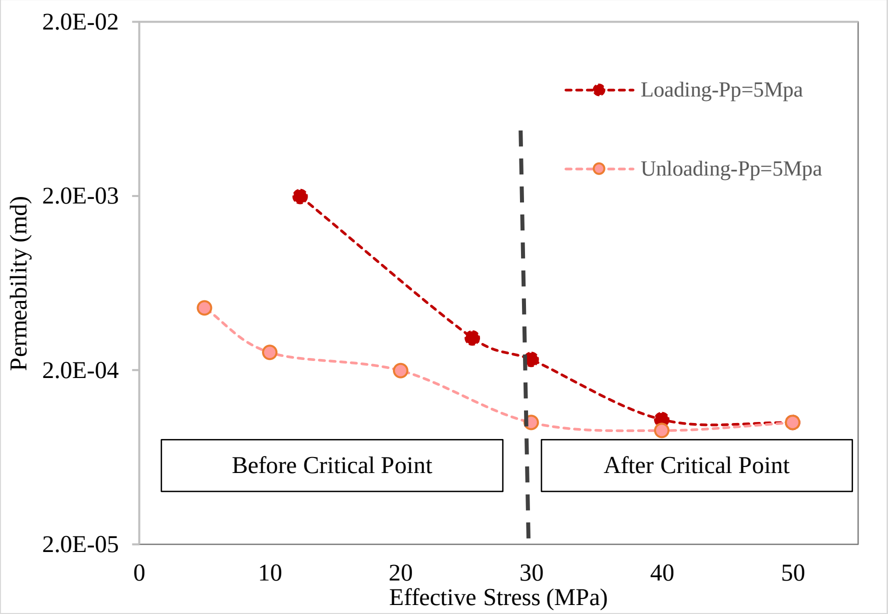

(b)

Fig.3-24. Dividing the loading/unloading path for experiment data points with non-zero pore pressure. (a) P_p=30 MPa, as it is appeared critical effective stress for unloading data point is delayed up to 10 MPa and shown with black array (b) P_p=5 MPa

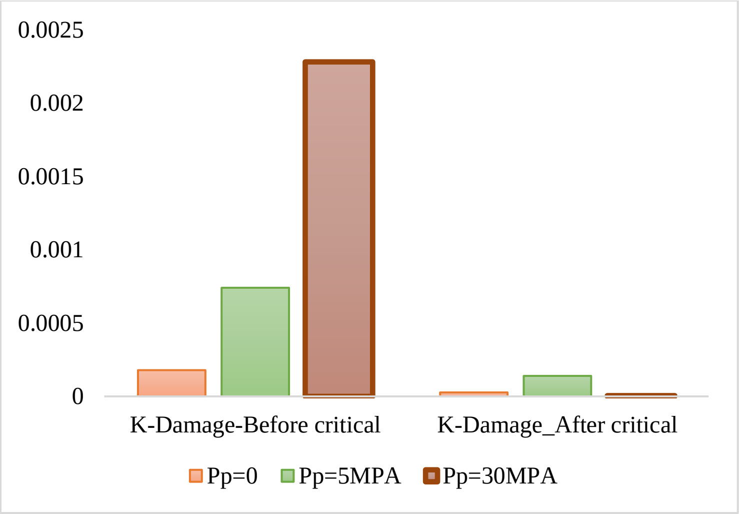

Fig. 3-25. Comparing average permeability results for second experiment (pore pressure effect)

We did not conduct XRD for our core samples in this work. However, XRD results based on Lui et al., (016 and 2019, for several Middle Bakken core samples shows clay percentage can vary from 13.6% to 63%. Therefore, existence of clay is feasible in the samples which can be the reason of low permeability recovery during unloading, especially for core samples with low effective porosity and tight pore throats. On the other hands if the clay amount is not significant, this cannot be attributed lower permeability in high pore pressure to clay swelling. Another explanation based on Noort and Yarushina, 2018, is that attractive forces between mineral surfaces increase in the presence of water. Under the high confining pressure, these forces can be brought close together, therefore, fluid flows harder and causes a further permanent decrease in permeability. If the attractive forces between the surfaces are large enough to hinder fluid flow and to keep the pores closed, the reduction cannot be retrieved by decreasing the confining (Vigil et al., 1994; Noort and Yarushina, 2018).

As David,1994, noted, the permeability of porous media mainly depends on the rock characteristics, such as porosity, pore throat geometry, tortuosity, pore connectivity, and more. If the fluid is reactive to the rock, other factors, such as wettability of the fluid, swelling of clays and other minerals, and the chemical interaction between the rock and the fluid, also affect the permeability. Based on the data available, it is not possible to discriminate whether surface tension and rock wettability or fluid-dependent pore shape caused the lower measured permeability in the samples (Noort and Yarushina, 2018).

Considering the stress sensitivity coefficient based on exponential fitted models to data points (Figure 3-26), it can be seen the average value for loading/unloading curves shows straight relationship with increasing pore pressure for both before and after critical point. However, the slope of stress sensitivity increment, decreases to more than half of the before critical point slope. In other words, it can imply that in term of increasing or decreasing pore pressure (e.g., fluid injection), permeability value should not change significantly after passing critical point. That being said, pore pressure would not cause permeability change or retrieving the permeability loss until a certain point. Figure 3-27 is comparing the average permeability change with stress sensitivity coefficient for three pore pressure cases (i.e., P_P=0 ,5 and 30 MPa).

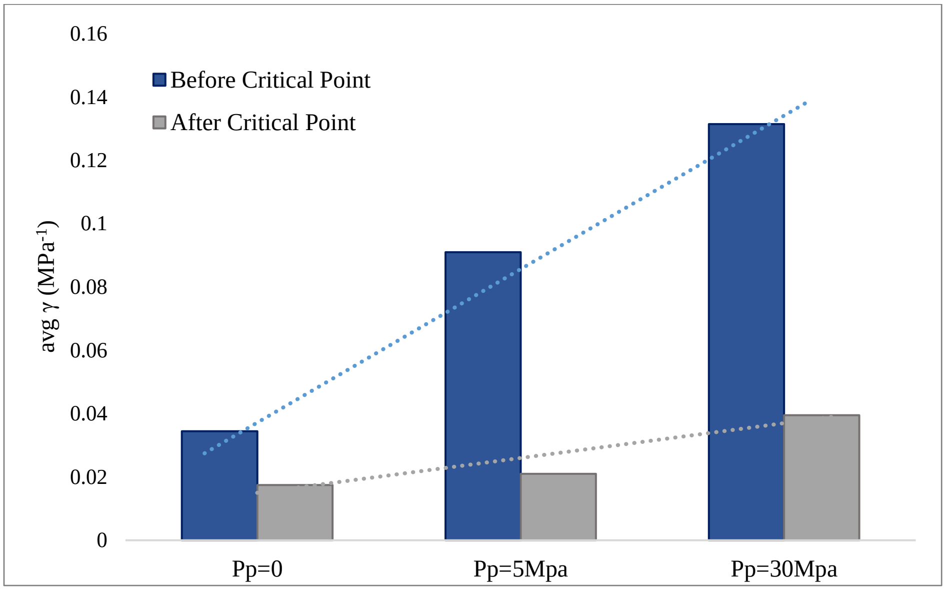

Fig. 3-26. Loading/Unloading average stress sensitivity coefficient based on pore pressure change, after and before critical point

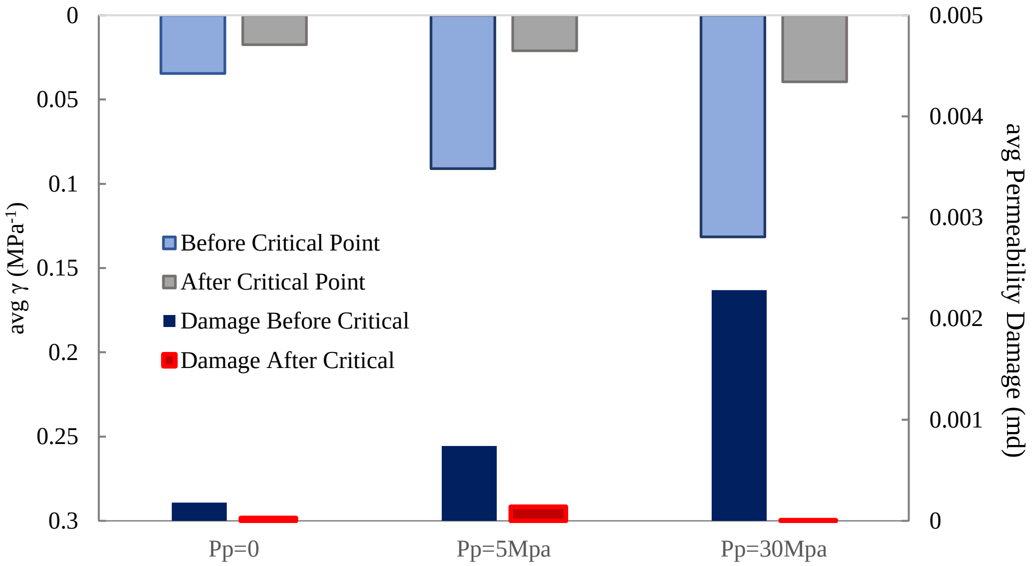

Fig. 3-27. Comparing average permeabilities with stress sensitivity coefficients before and after critical point for three different pore pressure values

Before reaching the critical point for each case, average permeability damage shows direct relation with effective stress dependency, however there is no clear correlation between permeability pressure dependency and the final average permeability after the critical pressure. This can be explained as effective stress is not the only parameter controlling the permeability damage after this point. Based on Noort and Yarushina, 2018, it might be related to the possible available mechanisms in presence of water during permeability measurement. Stronger decrease in permeability is expected during loading if water could mechanically weaken the rock sample. Therefore, based on the results, water did not increase pressure dependency, directly. However, as discussed earlier, the low permeability at high confining pressure with increasing the pore pressure can be due to hard fluid movement in blocked pore throats and narrow fractures. This could cause a delay in retrieving the permeability damage. That being said, average permeability damage, which represent the permeability change over stress unit, would be almost zero after critical point.

3.7.3. Pore Size Distribution

In the last experiment, two core samples with different PSDs (Figure 3-28) were compared. It is illustrated that for relatively homogenous PSD (core sample#1), the hysteresis gap decreases (31%), and the formation damage (i.e., irreversible permeability) improves. Core sample#2 with relatively heterogeneous PSD indicates higher difference in the loading/unloading path (38%) and this value can rise with increasing pore pressure as it is showed in second experiment. However, permeability reduction in the homogenous sample is slightly higher than the heterogeneous one, which can be related to pore sorting and pore sizes. As several authors mentioned in many cases interconnected pores (i.e., effective porosity) play critical role on controlling the fluid flow path. Consequently, distribution of large pores, cracks and pore shape distribution can control the permeability variation with pressure in core samples. (Walsh, 1965; David,1993; Civan, 2007).

Based on obtained PSDs (Figure 3-9), the percentage of large pores in sample#2 is higher than in sample#1. Critical point for sample#1 is almost same as other core sample, since they are obtained from same formation within certain depth (~3120 m). However due to high heterogeneity, pore size distribution was not same for the core samples. As it is well known, smaller pores and pore throats are sensitive to stress. The reason is that smaller pore throats can easily lose their connectivity during an increase of stress, while the probability of closing larger pore throats is low. In other words, large pore sizes can reduce but not close completely, therefore, displaying less sensitivity to stress (Dong et al., 2010; Teklu. et al., 2018).

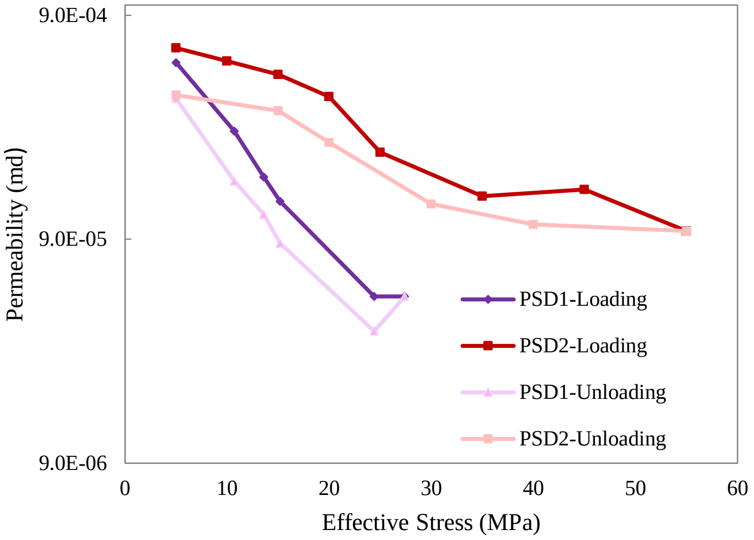

Fig. 3-28. Comparing measured permeabilities for two different PSDs

Calculated average permeability damage and stress sensitivity coefficient, γ, are in consistent with explained core sample behavior as well (Figures 3-29 to 3-31). Although permeability recovery in low confining pressure for two cases is slightly different (7%), average permeability before critical point is noticeably higher for core sample#2. This can be related to heterogenous pore size distribution for core sample# 2. However, permeability damage after reaching the critical point for core sample#1 is close to core sample#2. This shows the effect of matrix pore contribution for smaller pores, which cannot open easily comparing to larger pores and would not retrieve fully, as it was expected and explained.

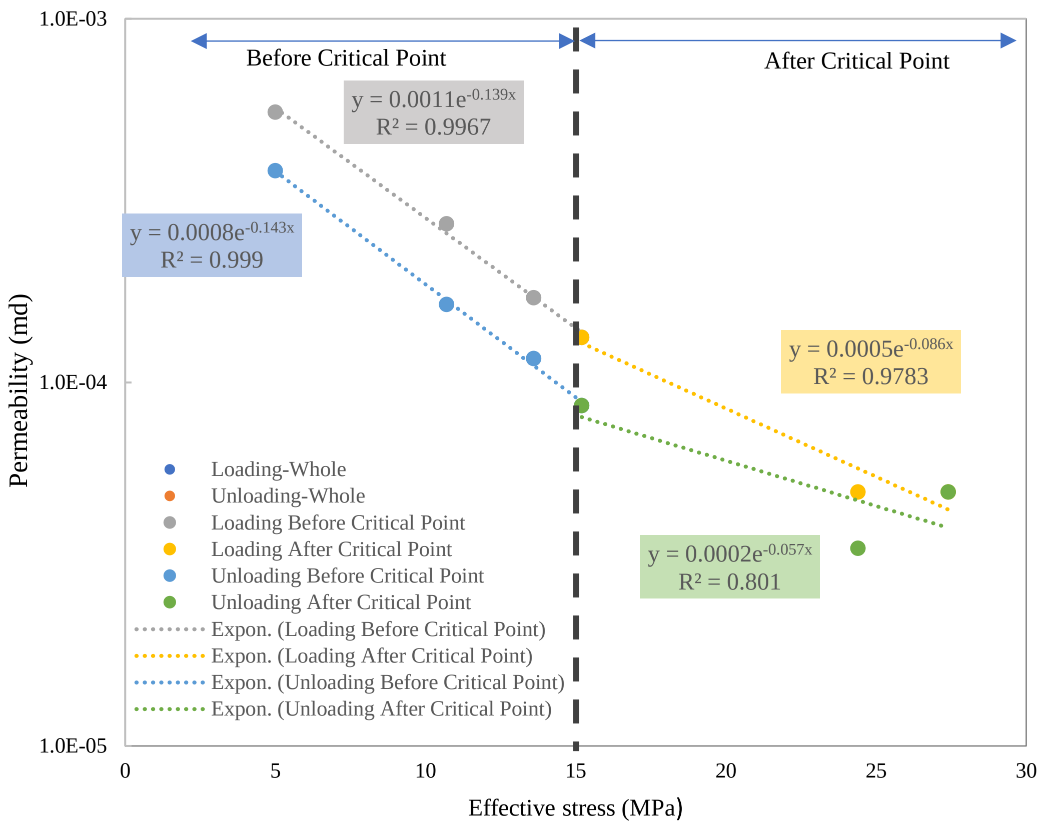

Fig. 3-29. Dividing the data point into two regions and fitting exponential model on semi-log plot; core sample#1

Also, it can be seen in Figure 3-31 for core with lower pore size (core sample#1), γ increases in both before and after critical point which correspond to a sharper decrease in permeability with pressure. As it is mentioned smaller pores show more permeability stress sensitivity which leads to the deformation of interconnected pore spaces and consequently, lower permeability (Xu et al., 2017).

In contrast with pore pressure experiment results, the data show an opposite correlation between γ and average permeability damage for small effective porosity core sample (Figures 3-30 and 3-31). While average sensitivity coefficient is higher for core sample#1, average damage before and after critical point is smaller than core sample#2.

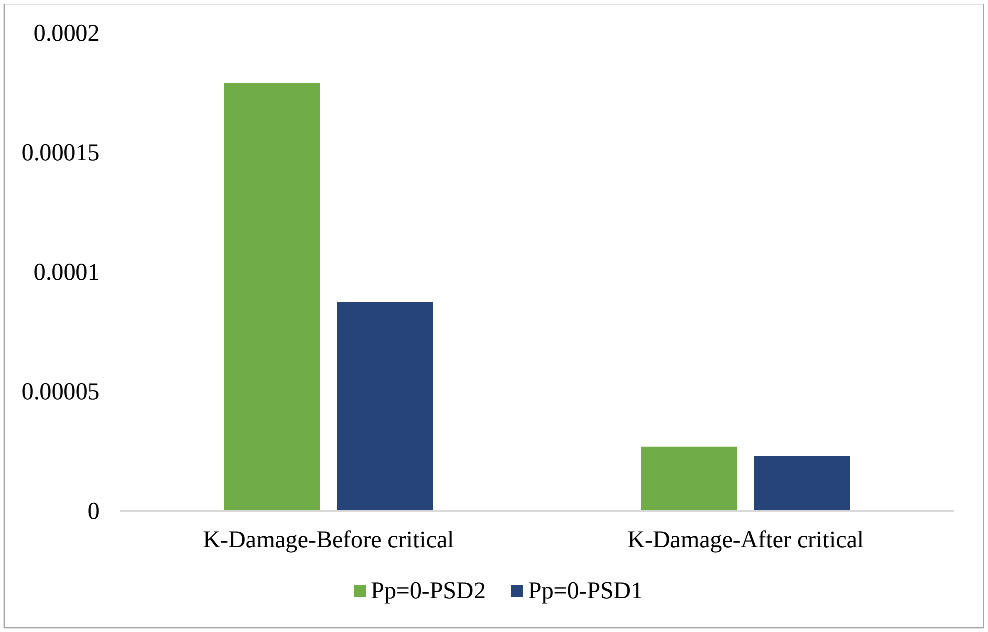

Fig. 3-30. Average permeability damage for both core samples

Thus, it implies that, stress sensitivity is not the only parameter controlling the permeability evolution. However, it is difficult to interpret the data further in the absence of information on the porosity sensitivity and it requires more investigation of pore size distribution and heterogeneity contribution on permeability damage during loading/unloading process.

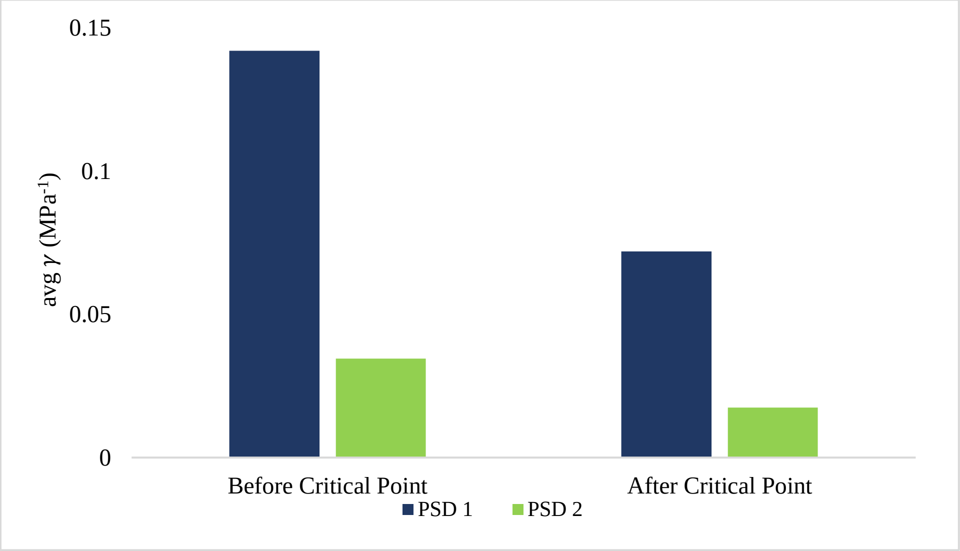

Fig. 3-31. Average stress sensitivity coefficient for both core samples

Therefore, in such tight unconventional reservoir it is recommended to calculate several core samples critical point, and permeability damage to get wide range of rock pressure dependent property alteration. For the core samples, critical points are between 15 to 30 MPa, γ changes from 0.158 to 0.012 MPa^{-1} which is in consistent with David et al., 1994, results for tight rock sample with γ>0.002 MPa^{-1} and permeability varies from 10^{-3} to 10^{-4} md based on different test conditions and core sample pore size distributions.

3.8. Summary and Conclusions

In this study, the permeability of some Bakken core samples was measured under various cases of loading/unloading effective-stress conditions. The permeability-stress sensitivity, critical effective stress and average permeability damage were evaluated under short- and long-stress ranges, different pore pressures and effective porosities. Below is the summary and conclusions drawn from this work:

- The effective porosity of core samples was determined through digital rock physics (DRP) and the permeability was measured by means of pulse-decay method.
- The exponential permeability model was able to well describe the permeability measurement data of Bakken core samples through straight lines on the semi-log plot of permeability vs. effective stress.
- Phenomenological mechanism of permeability sensitivity and permeability damage according to the exponential permeability-stress relationship is discussed.
- From such plots, observations were made to identify the impact of critical effective stress on the permeability sensitivity and average formation damage.
- Permeability continuously declines upon loading the sample and does not fully retrieve during unloading. The rate of permeability reduction changes beyond a

certain point referred to as critical effective stress. Moreover, the experiments revealed that the span of loading/unloading stress has a direct impact on the hysteresis distance and average permeability damage. However, after the critical effective stress there would be no significant change in the permeability and hysteresis and permeability recovery is almost zero. In other words, injection of fluids at any high pressure would not help the collapsed cracks and crushed grains to re-open, thus leading to lower production. Therefore, it is recommended that the critical effective-stress be determined in the lab which helps us better design, optimize, and execute successful and timely-planned pressure maintenance and EOR treatments.

- The effect of pore pressure on the permeability hysteresis was also investigated in this research. The results showed that at early stages of production in unconventional reservoirs where pore pressure is higher (i.e., lower confining stress), the relapse of permeability has a better chance than that during late time after the depletion has started. In higher effective stress increasing pore pressure showed negative impact on improving formation damage. This observation again highlights the significance of early-time injection for better EOR outcomes.
- From the experiments a 50% reduction of stress-sensitivity coefficient was observed, during both loading and unloading, when the applied stress approached the critical effective stress. Comparing stress sensitivity during loading with unloading results, show reduction permeability stress dependency during un-loading. Also, higher pore pressures before reaching the critical effective stress may cause greater sensitivity of permeability to effective-stress change.

- Before approaching the critical points, direct relationship between stress dependency and permeability damage was observed, for same core sample with varying pore pressure. However, this relationship would flip for core sample with different porosities. This implies that stress sensitivity is not the only parameter controlling the permeability evolution.
- With regards to the pore-size distribution, permeability hysteresis becomes more notable as the heterogeneity of samples is more significant. Comparing two different cores with various PSDs, proved that heterogonous sample has slightly larger hysteresis. However, low effective porosity and pore sizes in homogenous sample caused lower measured permeability and higher permeability reduction rate. Therefore, the permeability stress-sensitive behavior in Middle Bakken core samples is mainly controlled by the pore size distribution, heterogeneity, and micro cracks.
- Due to limited laboratory conditions, stress sensitivity evaluation is not fully reflecting the reservoir conditions where stress relief or drilling induced fractures can happen. Besides, the hysteresis phenomenon occurs based on several complicated processes, such as elastic and plastic deformation, contraction, shearing, compaction, and the like. Therefore, for a more accurate investigation, actual reservoir conditions need to be simulated as much as possible. Knowing the hysteresis phenomenon process and the caused permeability damage can improve controlling and managing reservoir production by proper operation decisions.

CHAPTER 4

PERMEABILITY MODELING USING MACHINE LEARNING

4.1. Introduction

Currently, the most challenging issues involve the collection and processing of a large set of data for multiple investigations related to addressing industrial problems. Applying conventional analyses may not be suitable for extracting useful information due to the increased complexity of the process. For this reason, a significant amount of research was devoted to addressing these issues through the incorporation of data mining as a key idea for the more precise treatment and interpretation of a variety of results (Sharma and Sharma, 2018; Angra and Ahuja, 2017; Dey et al., 2015). The practice of removing particular information from a database that was concealed and not explicitly available to the user using machine learning (ML), is known as data mining. While employing someone to identify the finest basketball centers is data mining, teaching someone how to play basketball is ML (Raschka, 2017). ML algorithms employ data mining to discover connections between diverse nonlinear relationships. ML is described as the application of various algorithms to train computers to detect patterns in data, which may then be utilized for future prediction and forecasting or as a quality check for performance improvement. ML enables computers to learn without being explicitly programmed. In summary, data mining is concerned with finding specific information, whereas ML is concerned with executing a specific task. Consequently, machine learning has received a growing amount of attention, particularly in the field of petroleum engineering. This technique entails identifying the correlations and rules that best characterize the behavior of outputs in response to the anticipated change in input attributes. However, many algorithms were developed for general objectives and subsequently applied to specific oil production enhancement and petroleum engineering domain research (Khan, Alnuaim, et al., 2019; Hegde and Gray, 2017). In this work, machine learning (ML) methods was employed, more specifically, an artificial neural network (ANN) algorithm, to the permeability-stress data to determine the general model that can describe the variation in permeability as a function of net confining stress for several core samples. Thereby, permeability evolution using the proposed matched curve was calculated and the results were validated with experimental permeability measured during the loading path. Using linear regression approaches (e.g., power-law and exponential correlations), the generated model covers a narrow range of study and cannot predict the change in permeability as a function of stress with introducing density, porosity, and grain volume. Hence, the implantation of ML to forecast the change in permeability versus stress for new data points can lead to major improvements, including the reduction in time effort and the cost of sampling. In the ML approach, the entire area of study can be covered by training a general model through few runs on a narrower range of variation. The developed ML algorithms were used in this work to find the general relation between permeability and the effective net stress accounting for different rock properties as inputs. Assuming a general model that can be parameterized under the most typical change in attributes of neighboring wells in a specific region is highly recommended as an alternate strategy that can limit the implementation of real core analysis in the non-exploitable area. To do this, it is vital to use valid algorithms to make these predictions. From the concept of decision tree regressor, it can be revealed that it is a high-level generalization algorithm because it is based on single-point decision making.

4.2. Machine Learning Workflow

It is critical to grasp standard ML workflows before discussing ML techniques and types. A typical ML workflow includes the following steps: (1) data gathering and integration, (2) data preprocessing, which includes (a) data visualization, (b) outlier detection, and (c) normalization/standardization, (4) model development, (5) optimization, and (6) finally, implementing the trained model (Book: Machine Learning Guide for Oil and Gas Using Python). Figure 4-1 summarizes the machine learning roadmap.

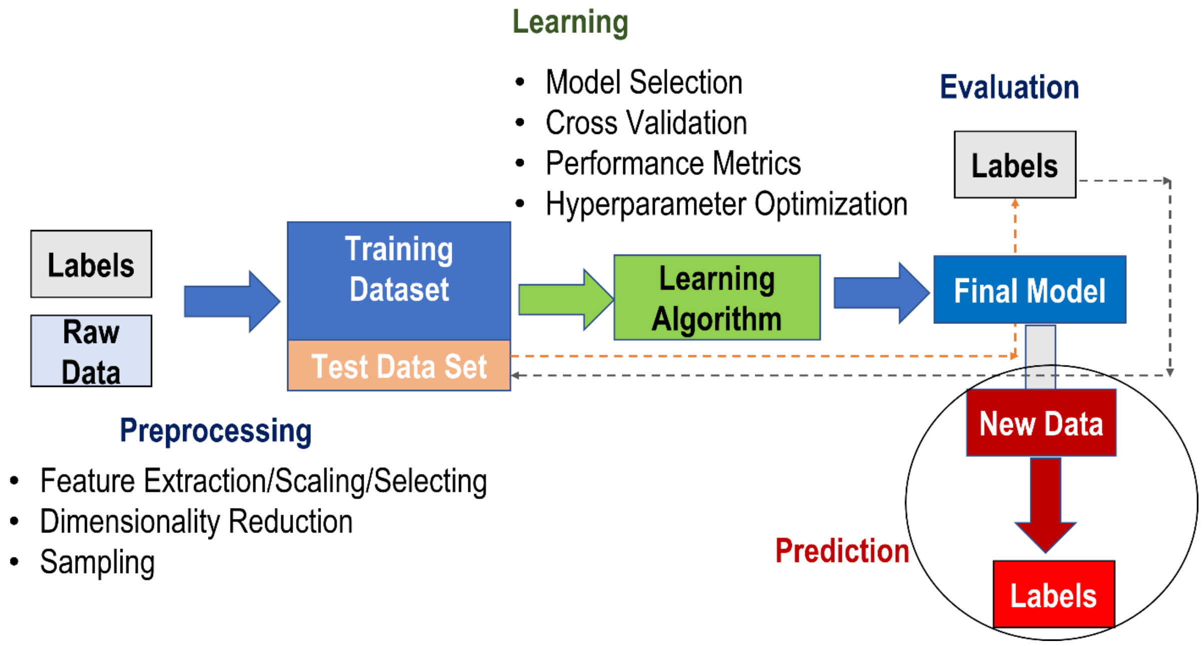

Fig. 4-1. Machine learning roadmap (Raschka, 2017)

4.3. Data Gathering and Integration

The available core data, such as permeability and porosity, was compiled under a wide range of net confining stresses from 90 core samples of the "Debrecen 1-3H" well in the Bell field. We picked this well since its core analysis input and output data are available in a way that enables us to execute the machine learning job (Boualam, 2019). Based on the reported results by Boualam et al., 2020, power-law and exponential models (Figure 4-2) for several data points at different depths were investigated under a small range of variation. Also, recovered permeability by unloading is lower than that of the initial permeability due to the hysteresis effect. The proposed range can vary based on sampling depth for each core sample under limited applied stress in the lab.

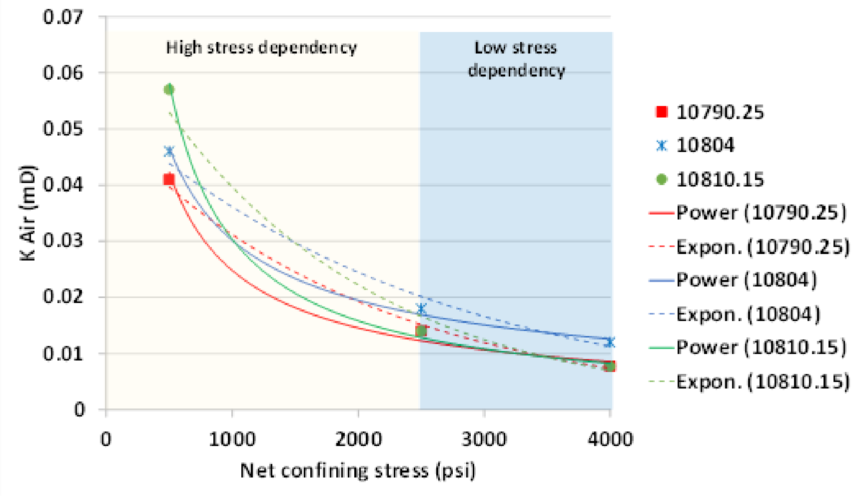

Fig. 4-2. Permeability versus net confining stress of rock samples from Middle Three Forks formation, well Debrecen 1-3H (Courtesy from NDIC data)

Therefore, each core sample can show different behavior under variable effective stresses. Hence, modeling the actual behavior of permeability requires plotting permeability under various cases of pore pressure and confining stress versus effective stress (Ma and Zoback, 2016).

4.4. Data Pre-processing

The selected inputs for the model are net confining stress, porosity, rock density, and grain volume, and the output is rock permeability. The input dataset must be treated and preprocessed before any machine learning algorithm can be executed. Raw data rarely comes in the form and shape that is necessary for the optimal performance of a learning algorithm. This includes imputing outliers which can cause overfitting of the model and therefore a reduction in accuracy. In some circumstances, it is vital to examine the contribution of outliers to the formulation of the final conclusion. Numerous functions were performed so as to not erase the influence of the outlier, since it may provide important information. By default, an outlier is a value that is more than three scaled median absolute deviations (MAD) from the median. However, if the data is not normally distributed and the imputation of outliers must not be restricted to a small deviation from the median, the quartiles method with clip function can be more effective in detecting local outliers and preserving the general effect by reducing the variation between the outlier and the median. In this study, the quartiles method was used to detect and fill outliers with the upper threshold. According to Figure 4-3, 404 outliers' permeability data points were deemed to be outliers.

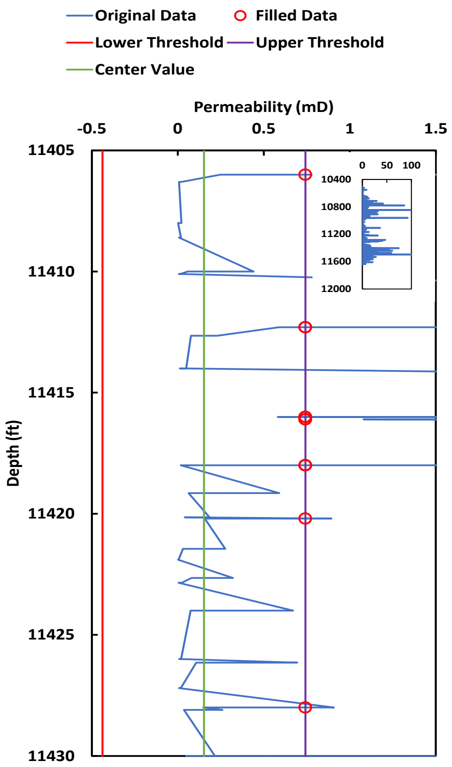

Fig. 4-3. Graphical detection of permeability outliers based on the quartiles method

As the success of machine learning models is dependent on the input data, it is essential to visually inspect the correlations of the input to prevent highly correlated inputs and a biased impact that is disproportionately large. Figure 4-4 pictures the relationship between the inputs.

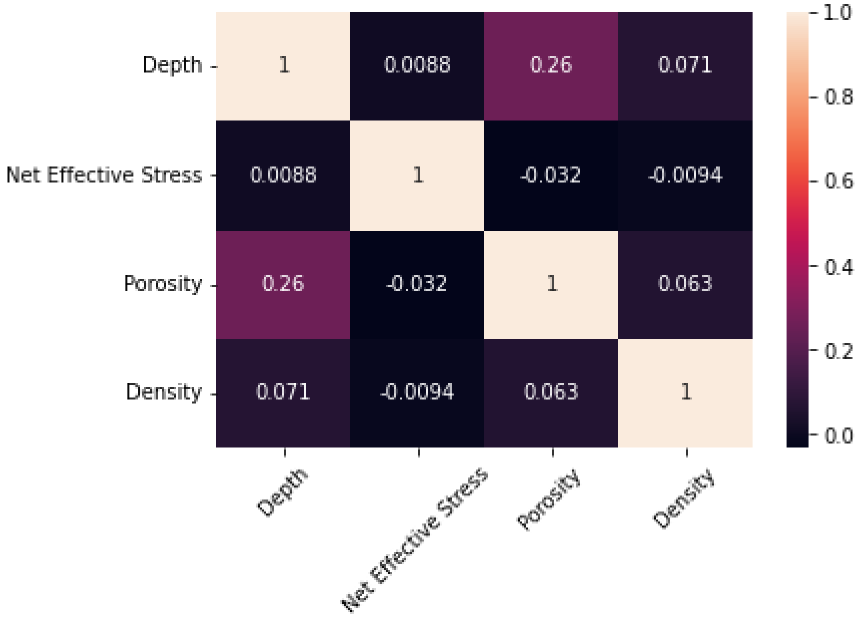

Fig. 4-4. Correlation matrix for regression inputs

These plots can provide a close look at the features that are redundant and must be removed from the input data. In fact, a coefficient close to one is a sign of the presence of a strong correlation between features and this can result in discarding one of them or using some analytical methods such as principal components analysis to reduce the dimensionality of features. Depth was considered a feature only in case that are generalizing the prediction model on a larger dataset that includes different wells. If the single well is used for model development, then depth is not carrying any information to the output and should be assigned as an index. No relationship between inputs is observed upon analysis of the plot.

In addition, the inputs must be rescaled to lessen the dominance of certain characteristics on the overall contribution to the prediction of outputs. This step will limit the variance range for each data set. Scaling with normalization was done on all features in this study using the following formula:

$$x_N = \frac{x - x_{min}}{x_{max} - x_{min}} \tag{4-1}$$

where x_N is the normalized observation, x_{min} is the minimum observation, x_{max} is the maximum observation.

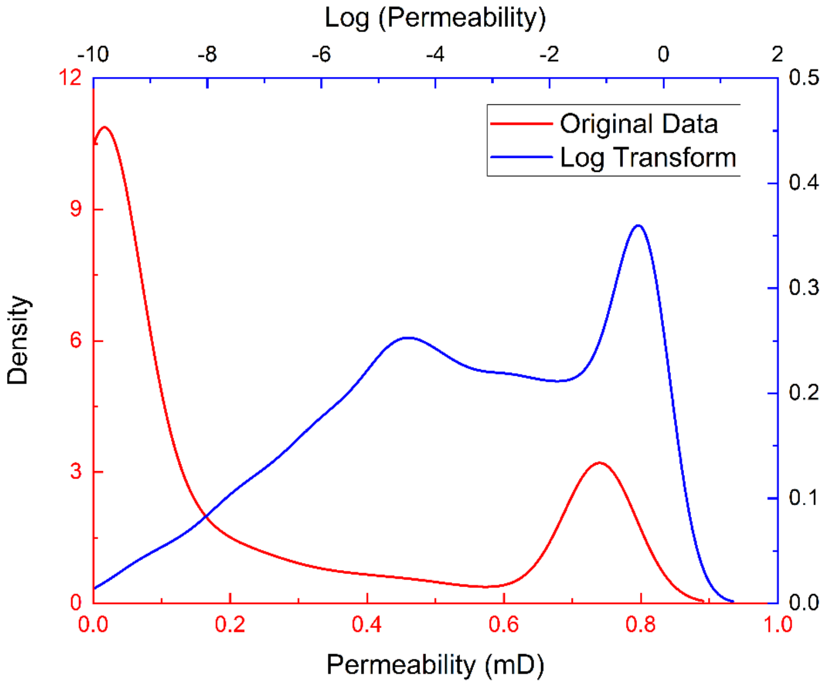

Fig. 4-5. Log transform of the output (permeability)

Log transform (Figure 4-5) is used to reduce the skewness of the output data. This can prevent the model from being trained on a certain range of data more than the rest of the data. Hence, this creates a high uncertainty in the prediction performances. The preprocessing of the data is one of the most crucial steps in any machine learning application. In practice, it is essential to compare at least a handful of different algorithms to train and select the best-performing one. But before doing that, a decision needs to be made upon a metric to measure performance. After selecting the model that has been fitted to the training dataset, the test dataset can be used to estimate how well it performs on this unseen data to estimate the generalization error. If the performance is satisfying, the model can be used to predict new (future) data. To assess if the machine learning algorithm not only performs well on the training dataset but also generalizes well to new data, R^2 is measured for both datasets. A model that seems to perform well during training but badly during testing is overfitted to the training dataset since it does not generalize effectively.

4.5. Machine Learning Model Description and Setup

Model development requires the construction of a representative subset of data after data pretreatment. Data points are partitioned into a training set, a validation set, and a test set. The training set consists of the assortment of observations used by the algorithm to identify the interplay between the inputs. The validation set is used to update the trained model's hyperparameters. The purpose of the test set is to assess the validated model by predicting fresh data blindly. At this stage, while dividing the data, additional considerations must be taken into account, including a rigorous assessment of the model's performance under a given ratio of the test set. The model must be well trained utilizing a substantial amount of data. Twenty percent of the observations were chosen for algorithm testing, while the remaining eighty-five percent were split 85:15 for model training and validation, respectively. After dividing the preprocessed data, two algorithms with distinct architectures were constructed. In this work, ANN is the first technique utilized to calculate the permeability regression because to its broad applicability. This algorithm's design was influenced by the structure of the nervous system. Therefore, the ANN was constructed by implanting several artificial neurons inside various sorts of layers. Here, the assumption is that the initial and final sets of neurons correspond to the input and output layers, respectively, and that the neurons formed between these two sets may be grouped into several hidden layers. The number of hidden layers may be adjusted based on the number of neurons necessary. In this work, the number of neurons has been optimized, and a single hidden layer has been used (Figure 4-6). In addition, the Levenberg-Marquardt training function is performed in order to maximize the weight and bias values. In order to evaluate the performance of ANN, the mean square error is computed using the following formula:

$$MSE = \sum_{i=1}^{n} \frac{1}{N} (y_P - y_R)^2 \tag{4-2}$$

Where y_P is the predicted output and y_R is the real output for n data points. The error was performed using the MSE function on MATLAB.

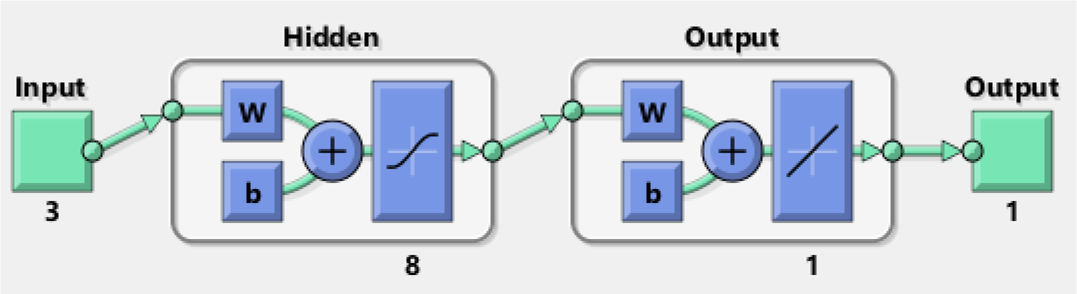

Fig. 4-6. Artificial neural network structure

The decision tree regressor is another algorithm that was used on the more generalized dataset. ANN can be applied to only a single well while a decision tree regressor can be used on multi-well permeability prediction. The concept of the DT algorithm is based on branches that constitute plausible decisions, which can be taken concerning a specific relation between inputs. The regression using this algorithm can provide a clear explanation of the reasons behind a regression of certain values by setting conditions at each lower range separative node.

4.6. Results and Discussions

Using the ANN method, the following regressions of permeability was determined. Using various metrics and a graphical representation, the derived findings were compared to the actual data. Each inquiry has been supplemented with an optimization section that identifies the optimal available parameters for enhancing algorithm performance.

4.6.1. Low-level Generalization (Single Well)

Successful training relies on a complicated combination of numerous accessible factors. First, the model's variance and bias are impacted by the model's complexity and input features selection. The input characteristics for each variable have been chosen based on the formulas provided. Secondly, the dimensionality of the inputs dictates the number of neurons in the hidden layer. Due to the algorithm's operating concept, there are no correlations or recommendations that can be used to estimate the optimal number of hidden neurons. If attempting to execute the algorithm numerous times under certain beginning circumstances yields varying outcomes for each execution, the answer is to do a post-optimization based on the resulting mistakes. Figure 4-7 depicts the variation MSE in relation to the hidden neurons. The findings reveal that 3, 5, and 8 hidden neurons are the best amount for developing a high-performance algorithm.

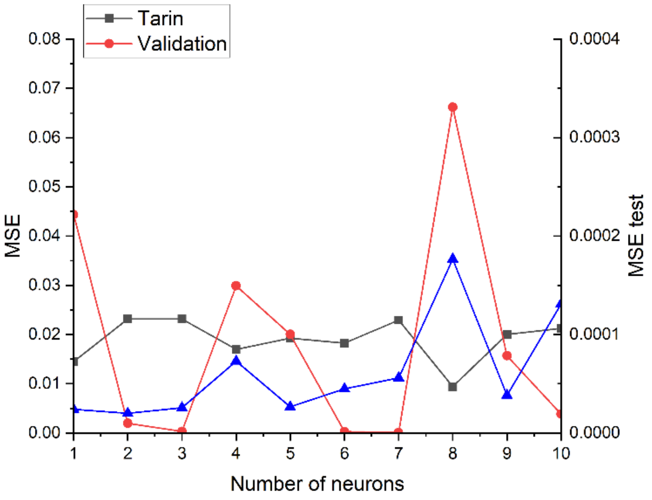

Fig. 4-7. Evolution of mean squared error as a function of the applied number of neurons for the training set, the validation set and the testing set

MSE is only a point estimate taken from the distribution of feasible MSEs, and the precise data included in the training set versus the test set impacts this point estimate. It is recommended to determine the shape of the underlying distribution in order to be able to judge which of the three optimization points can be trusted when the model is used for different data sets. An uncertain model is defined by the training MSE being considerably greater than the test MSE. This is done by taking the training set and randomly selecting 80% of it for a new sub-training set and the remaining data points represent the new sub-test set. MSE was recorded for both of these sub-training and sub-test sets. Then the process was repeated many times to plot the distribution. As seen in Figure 4-8, ANN with 8 hidden neurons increasing the number of neurons may lead to overfitting. This may be attributed to the significant number of errors that were anticipated during the testing phase.

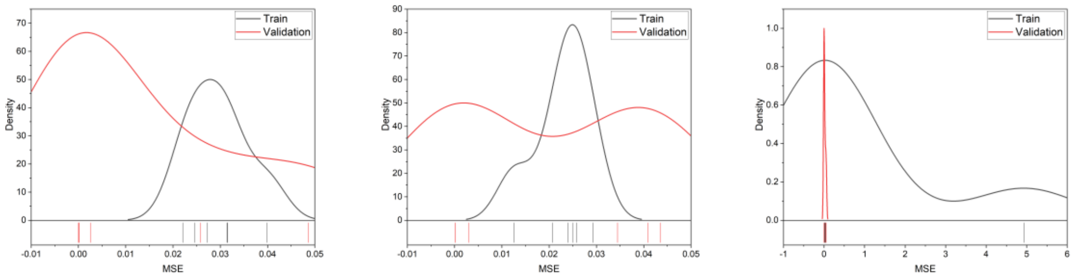

Fig. 4-8. MSE distribution along the data subset for validation and training, 8 hidden neurons (right), 5 hidden neurons (center), and 3 hidden neurons (left)

It can be seen that the predicted permeability using the ANN model shows a reasonable match with the 90 real permeability data at different depths (Figure 4-9). The use of this model in constructing the compaction table should present a better trend than the exponential model to predict the stress-induced permeability.

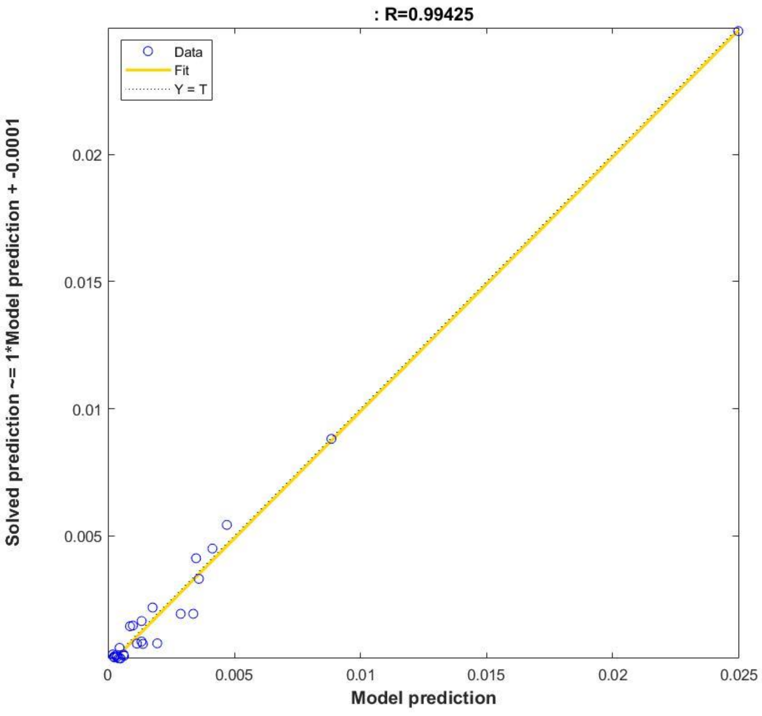

Fig. 4-9. Linear fit of predicted permeability with the real permeability data (ANN model – Single Well)

It was reported (Boualam et al., 2020 and Assady et al.,2020) that the change in permeability beyond a certain stress level (~25 to 30 MPa) becomes barely remarkable. This behavior could be observed only in the ANN model. An exponential model shows a continuous decrease in permeability at high effective stress where it should remain constant or show a slight decrease. This inconsistency in exponential model results makes the ANN model a better choice for predicting the permeability trend in the Bakken/Three Forks Formations (Figure 4-10). The experimental core data collected from well Debrecen 1-3H (Boualam et al., 2020) was used to verify the validity of the ANN model. The permeability model for the Bakken formation was also developed using an ANN (Figure 4-11). Most of the data points fit better to the ANN model. Based on Figures 4-10 and 4-11, the exponential model does not show the critical stress point (i.e., where permeability change approaches a plateau), and it is not representative of permeability change at higher effective stresses. This erroneous prediction can be explained by the correlation coefficients, which are taken from one depth only. In contrast, the ANN model was trained on core samples taken from different depths and covered a wide range of investigations.

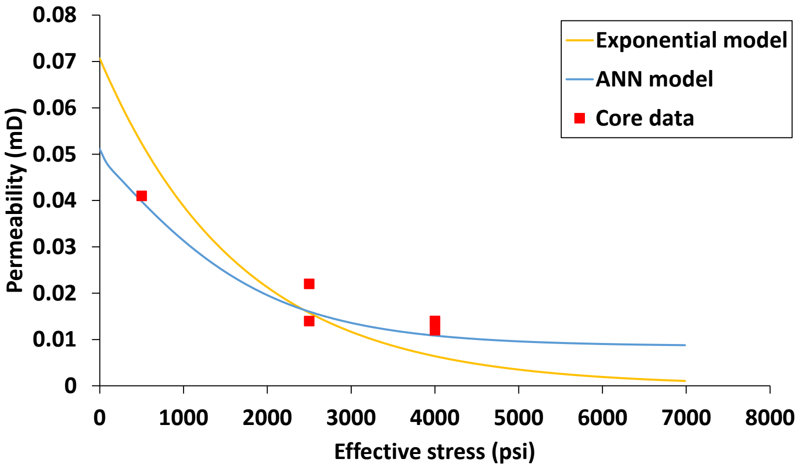

Fig. 4-10. Comparing permeability-stress models matching with the experimental core data (Boualam et al., 2020) for Three Forks formation

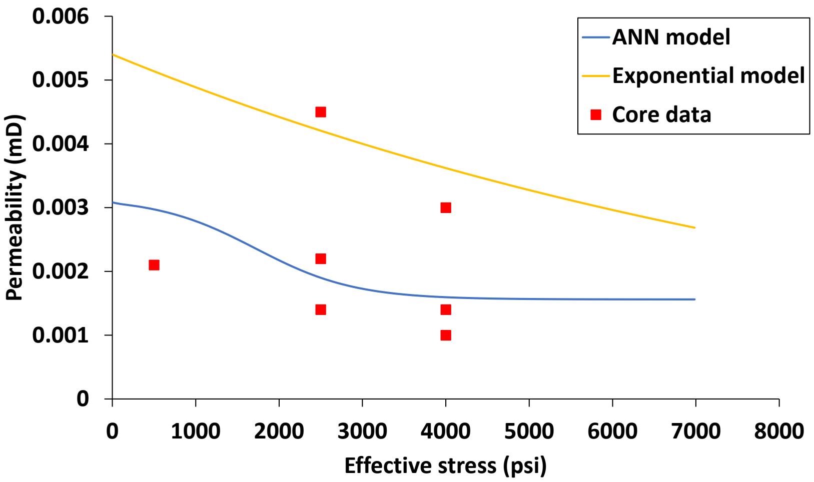

Fig. 4-11. Comparing permeability-stress models matching with the experimental core data for Bakken formation

4.6.2. High-level Generalization (Multiple Wells)

Although the ANN algorithm over one set of well data showed promising results and accurate permeability prediction, the error between predictions and actual permeability data obtained from including several wells for the training is not good. This could be explained by the fact that we have a lot of fluctuation in the permeability data which makes it hard for the model to catch a trend between inputs and outputs. Trying manually to remove these fluctuations and splitting the data into smaller ranges did not solve the problem of getting good R^2 but a large normal difference between prediction and actual data (error). The other factor that could play role in causing biasing of the model is the non-equal distribution of data. Even the split of data into ranges couldn't eliminate the clustering of permeability values towards smaller values (Figure 4-12).

This clustering of data has caused the overestimation of low permeability values and underestimation of high permeability values. Based on the Decision tree regressor working principle, it can address this problem (Figure 4-13).

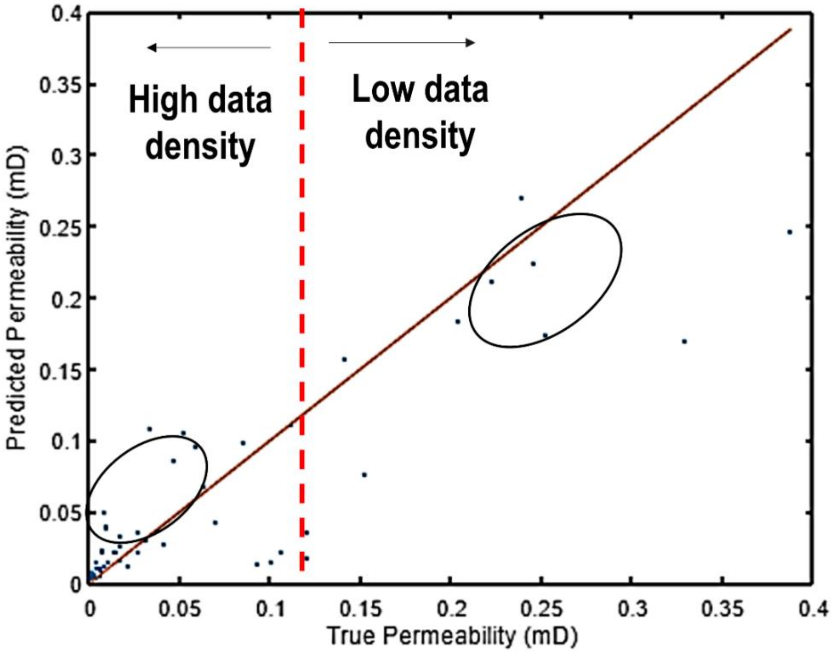

Fig. 4-12. Non-equal distribution of data, overestimation/underestimation of permeability data

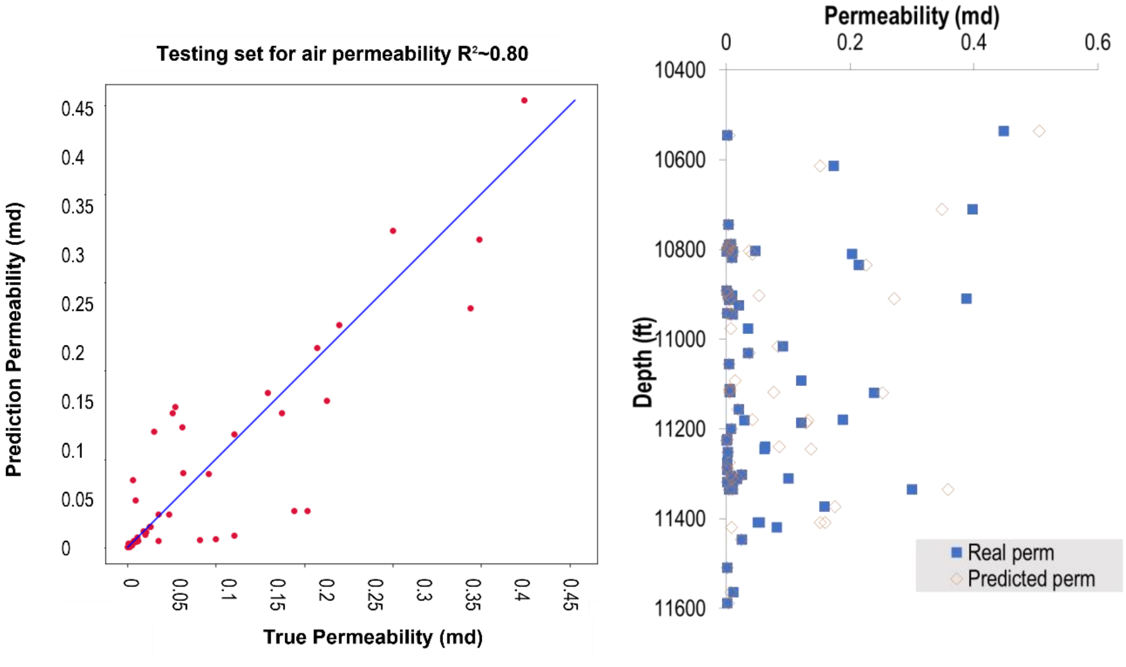

(a)

(b)

Fig. 4-13. (a) Linear fit of predicted permeability with the real permeability data (Decision tree model – Six Well). (b) Predicted permeability vs. true permeability for tested well

The decision tree regressor split the data to intervals (range) that represents the leaf of the tree. This leaf could carry one data point. Hence, the prediction could be made on widely smaller range of data point, and this might solve the problem of the non-equal distribution of data. More investigation of the process is out of the scope of this work.

4.7. Conclusions

- A machine learning technique, specifically, an artificial neural network (ANN) algorithm, was employed over the entire set of formation depth. The model was trained over the variation of core samples properties, including rock density, porosity, and grain volume, to improve the permeability-stress correlation. This approach generated a model that can accurately predict the permeability change versus effective stress for entire depths, using only one equation.
- After the critical stress point, permeability change is not significant, which could be captured using a ML model. In contrast, an exponential model shows a continuous decrease in permeability at high effective stress. This inconsistency in exponential model results makes the ML method the best choice to obtain an accurate permeability-stress correlation in tight oil reservoirs.
- Although the ANN algorithm over one set of well data showed promising results and accurate permeability prediction, the error between predictions and actual permeability data obtained from including several wells for the training is not good. The Decision tree regressor can address this problem.

CHAPTER 5

SIMULATION MODELING AND EVALUATING EOR PERFORMANCE

5.1. Introduction

Over the recent decade, a rise in global oil demands forced the oil and gas industry to consider unconventional reserves that were deemed uneconomical before. Such developments of unconventional resources in North America became possible using advanced technologies in horizontal drilling and multi-stage hydraulic fracturing along with new EOR practices. Although North Dakota contributed over 1.2 MMbpd of crude oil to the United States oil production (NDIC, 2021), only 2% of 600 billion (bbl) OOIP is recovering (Nordeng and Helms, 2010). The Bakken and Three Forks Formations are considered a major source of oil production and play a critical role in increasing oil recovery factors. The sharp decline rate of production from Bakken and Three Forks formation leads to the low primary recovery factor. It requires an efficient enhanced oil recovery (EOR) method to increase oil production. Recently, produced HC gas has been employed in several unconventional plays. Eagle Ford, as an unconventional reservoir and similar geologic conditions, reservoir properties, and production history to the majority of Bakken wells, showed a successful gas EOR pilot with outstanding oil production of a 30% to 70% increase (Hoffman, 2018; Grinestaff and others, 2020; Pospisil and others, 2020). The results are encouraging in the possibility of improving EOR performance in the Bakken/Three

Forks wells with more stabilized oil rate production. Many researchers are exploring the mechanisms behind such higher recoveries and whether those gains can be sustained long enough to add reserves and cash flow to the unconventional tight shale plays.

The following sections briefly summarize the key lessons learned from history of Bakken EOR tests from 1994 to 2018, the impact of permeability change during reservoir pressure change, and related curves are discussed. At the end of this chapter, two different simulation models with variable well and stimulated region pressure are presented. Gas injection scenarios are evaluated to find an optimum time of injection.

5.2. Historical Bakken Tests

Bakken pilot EOR attempts have been employed since 1994. The overall nine pilot efforts include CO2, water, and rich gas injection in North Dakota and Montana portions of the Williston basin, which were performed to address injection feasibility and incremental oil production. Two pilots were performed via water injection, four CO2 injections, one propane, and two field gas injection shown in Table 5-1.

Table 5-1 – Summary of the historical Bakken EOR pilot tests (Pospisil et al., 2022)

Pilot	Operator	Year	EOR Scenarios
1	Meridian	1994	13Mbbl Water injection
2	EOG	2008	30.7 MMscf CO2 injection
3	Enerplus	2009	45 MMscf CO2 injection
4	EOG	2012	38 Mbbl Water Injection
5	EOG	2014	88.7 Mscf field gas injection
6	Whiting	2014	3.4 MMscf CO2 injection- Vertical well
7	Hess	2017	9.5 MMscf C3H8 injection- Vertical well
8	XTO	2017	1.7 MMscf CO2 injection – Vertical well
9	Liberty	2018	160 MMscf Rich gas injection

5.2.1. Water Injection Tests

The first pilot in Bakken was a water injection test conducted by Meridian Oil in the Bicentennial Field, McKenzie County. Approximately 13,200 barrels of fresh water were injected into a horizontal well in the Upper Bakken Shale in 1994. The well was shut-in for two months, after which oil production remained below pretest rates for the rest of the well's operational life. In 2012 the first huff and puff water injection pilot was conducted by EOG. Two cycles of produced water with the rate of 1200 bbl/D were injected in Parshall Field. The results showed that although injectivity was not a problem, no incremental oil production was achieved. The third test was conducted from 2012–2013 by EOG in the Parshall Field. This unit was later selected for a field gas injection test. Water was injected in two cycles. First cycle with the injection rate of 1350 STB/D for several months, increased the injector BHP to 6000 psi. Water production increased significantly from offset wells and zero incremental oil production was observed. The second cycle started after six months, with a water injection of only 380 STB/D and maintaining the injection well BHP at 5500 psi. There was no significant increase in water production from the offset wells with no incremental oil production from any of the four wells (Sorensen and Hamling, 2016; Nagarajan and others, 2020).

5.2.2. Gas Injection Tests

In late 2008, EOG conducted a CO2 injection test in the Parshall Field, Mountrail County. CO2 injection of 30 MMscf within 29 days with a huff and puff approach was performed. Later, The Elm Coulee Field pilot test was conducted jointly by Continental Resources, Enerplus, and XTO Energy in the Burning Tree-State in the Bakken Formation in 2009. Huff and puff approach with 45 days of injection and 64 days of soaking was used in this test in early 2009. Approximately 45 MMscf of CO2 were injected at rates as high as 3 MMcf/d. In 2014, a huff and puff pilot with CO2 injection in an unfractured vertical well was implemented in the Bakken formation in North Dakota. Due to an early gas breakthrough in an offset well 900 feet away, CO2 injection ceased within four days of injection. The total injection volume was 3.4 MMscf. In 2017, XTO Energy operated a vertical well CO2 injection test designed jointly by XTO and the EERC. The total injection took place over four days with a 1.7 MMscf CO2 injection. In the continued two cycles of water injection in 2014, EOG conducted field gas injection using the four-producer for a gas injection test. The enriched injection gas with 55% methane, 10% nitrogen, and 35% C2+, was injected at a rate of 1.6 MMSCF/D for 55 days. The objective of water injection with gas injection was to improve gas conformance in the fractured system, and higher pressure builds with less gas injection volume. A total of 88.7 MMscf of field gas was injected during the process.

All gas injection tests demonstrated injectivity is not a limiting option in Bakken, but gas conformance control could be challenging in fields with a high degree of natural fractures, such as Parshall Field. Most of the tests showed zero to slightly incremental oil during the operation. The slight increase in oil production could be related to the pressure build-up and miscibility of gas and oil (Sorensen and Hamling, 2016; Nagarajan and others, 2020).

In 2017 Hess conducted a propane injection test in a Red Sky Nelsons Farm DSU. The objective of this test was to demonstrate propane injection performance. Propane can be efficient due to first contact miscibility with the Bakken oil and less operational requirement. Propane could be pumped into the injection well without needing a compressor due to its liquid form in field conditions (Nagarajan et al., 2020). A total injection of 19 MMscf propane was employed for seven months of 2 cycles. The production well was kept shut-in during injection and put back into production after a long soaking period. The well showed a sharp oil rate increase during production and then declined and steady at a higher pre-injection value for over four months. As pilot results showed, injectivity was not an issue, and propane could permeate into the matrix and interact with oil, thus swelling and mobilizing it (Nagarajan et al., 2020).

In 2018, Liberty Resources conducted a multi-well rich gas EOR pilot in the Stomping Horse Complex in Williams County, North Dakota. The pilot test was deployed using produced gas from the pads and mainly consisted of C1 through C3. The main objective of the pilot was to determine the technical feasibility of produced gas injection and the impact of incremental production due to gas/oil miscibility. Also, evaluate and optimize injection methods for EOR and assess injection conformance control (Pospisil et al., 2020). In total, ~160 MMSCF of gas was injected over ten months. Approximately 90% of the injected gas was produced with no incremental oil production. Although no dramatic incremental oil was observed, the pilot test indicated that higher bottom hole pressure is required to achieve higher MMP and miscibility, which require substantially higher gas rates and volumes, especially when pressure is below the bubble point (Pospisil et al., 2020).

5.3. Reservoir Pressure Regions

As per chapter 4 and the current chapter, reservoir pressure plays crucial rules in the effectiveness of gas injection. It is important that during the injection scenarios offset the to stress-dependent permeability reduction, as well as achieve the target minimum miscibility pressure (MMP). Both scenarios could improve the production from tight oil reservoirs. The reservoir gradually loses its original pore pressure during production, increasing reservoir net effective stress. Therefore, a reduction in reservoir properties such as permeability or porosity can occur in response to net stress change within the pores due to the withdrawal of the fluids from the reservoir. With that, it is essential to include all possible mechanisms during the modeling of the reservoir and capture the dynamic fluid flow before designing the test. In order to conduct and evaluate injection scenarios, three important regions during reservoir pressure change are defined. Figure 5-1 illustrates the general divided regions for a reservoir with an initial pressure of 7000 psi and a critical point of 3500-4500 psi (possible range of Bakken critical points). Assuming Biot's coefficient of unit and based on Eq. 3-7, the reservoir pressure regions would be as Figure 5-1.

The timely reservoir pressure is divided into region 1 where the pressure is above possible critical pressure and higher than MMP. Region 2 works as a transition zone where the reservoir is close/or at critical pressure where still MMP is achievable. The third Region is related to the time that reservoir pressure is beyond a critical point and injection gas is not miscible with oil anymore.

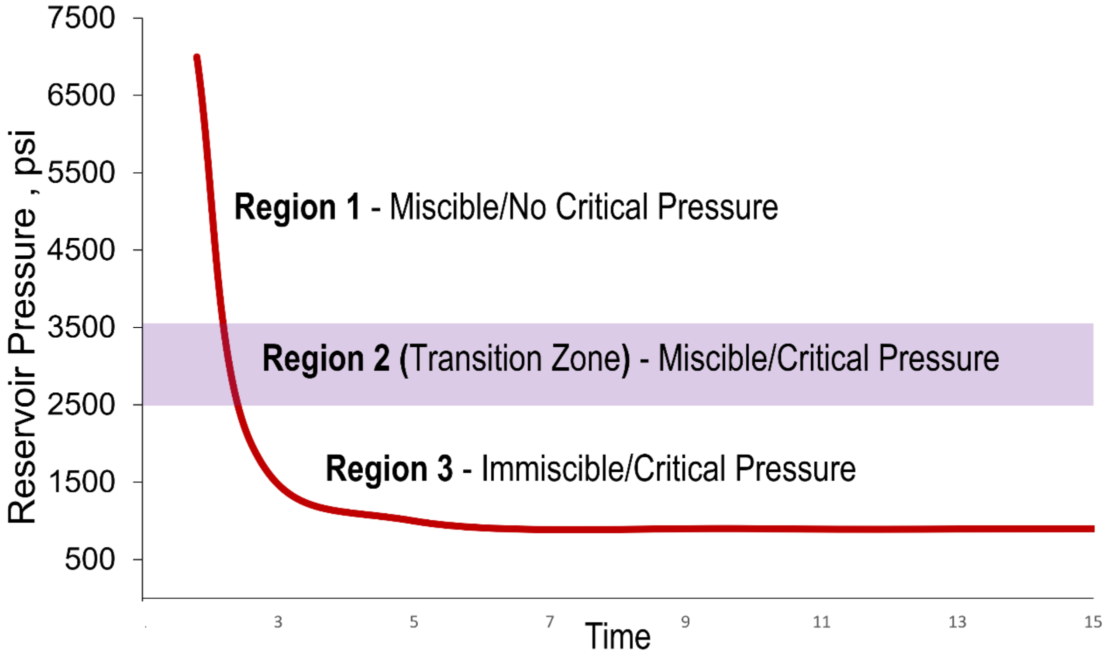

Fig. 5-1. Reservoir pressure vs. Time and respective regions

The region ranges can be changed based on the injection gas and critical effective point. Therefore, considering these three major regions and integrating them into the reservoir simulation modeling can improve the EOR evaluation based on the injection time.

The rest of the chapter will discuss reservoir simulation modeling by considering the defined regions for stimulated space unit (DSU) and well bottom hole pressure. The first set of modeling discusses the model with a depleted well condition and variable DSU pressure. The second simulation efforts evaluate a model close to real field data with variable well BHP region.

The Table 5-2 shows the regions of investigation based on the pressure of DSU and around the well. Note that BHP is always less than DSU pressure. Therefore DSU-region 2 with BHP-region 1 or DSU – region 3 with BHP – regions 2 and 3 cannot occur in the reservoir.

Table 5-2 – Different reservoirs regions and possible injection scenarios

	BHP - Region 1	**BHP - Region 2**	**BHP - Region 3**
DSU- Region 1	Continuous Injection or Huff n Puff?	Continuous Injection or Huff n Puff?	Continuous Injection or Huff n Puff?
DSU- Region 2	■	Continuous Injection or Huff n Puff?	Continuous Injection or Huff n Puff?
DSU- Region 3	■	■	Continuous Injection or Huff n Puff?

5.4. Reservoir Simulation Modeling

Reservoir simulation is a valuable tool to understand the mechanisms and predict the performance of gas-based EOR in unconventional reservoirs. It allows engineers to evaluate a particular EOR method through a sensitivity analysis and more intricate optimization algorithms. Most simulation models often use the compressibility concept to consider the change of pore volume, where the rock properties are usually assumed to be insensitive to the change of stress state (An et al., 2019). However, shale rock and fluid dynamic features in confined nano-pore space show that reservoir compaction and stress changes can considerably impact reservoir management and production performance. Therefore, it is necessary to provide more realistic dynamic flow predictions.

5.4.1. DSU Variable Regions

In this study, based on the observation from experimental data and available permeability-pressure correlation for the Bakken and Three Forks formations, the focus was on the effect of permeability evolution and hysteresis on CO2-EOR performance for improving CO2 injection design in tight oil reservoirs. First, eight layers reservoir model was built with no permeability change during the injection/production process. The model is compared with stress-dependent permeability in which the permeability evolution is considered within the Bakken/Three Forks ranges. In this study, two different permeability-pressure correlations were utilized in the simulation models, one based on the derived equation by ML technique in this study and the second considered exponential (EXP) decline as per literature (Boualam et al., 2020). For each correlation, the hysteresis effect was integrated during unloading by assuming a 15-30% permeability reduction before critical effective pressure. CO2 injection at different reservoir pressure statues was conducted to determine permeability alteration effect on CO2-EOR. In addition, critical effective stress is considered in the range of 25-30 MPa (Boualam et al., 2020; Assady et al., 2020). Single-stage fractured properties and simulation data used as the base case are summarized in Table 5-3 and Figure 5-2. These data are gathered from previous Bakken case studies (Alfarge et al., 2017) and available data in the North Dakota Industrial Commission (NDIC) website. For comparison, all input parameters were kept constants for all cases, except the matrix compaction table where it varies based on selected correlation for the Bakken and Three Forks formations.

Table 5-3. Fracture properties used in this study

Reservoir depth, ft.	9,000	**Fracture numbers**	15
Fracture spacing, ft.	50	**Fracture width, ft.**	0.02
Fractured permeability, md	20	**Fracture half-length, ft.**	350

A compositional simulation approach for a symmetric Cartesian grid system and single porosity model was applied in this study. The compositional model for reservoir fluid was generated using WinProp PVT modeling with a generic fluids PVT data from the Bakken Formation. Hydrocarbon model was utilized to build a validated phase behavior model and obtain tuned composition properties.

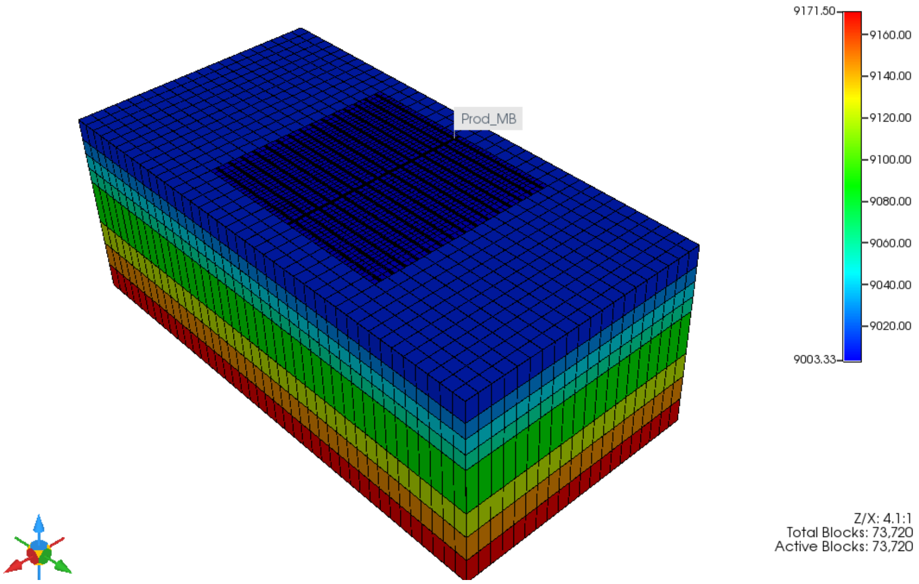

Fig. 5-2. Single-stage base model with 8 layers for Bakken and Three Forks Fm

During oil production, miscibility/immiscibility of CO_2 was controlled by monitoring the bottom hole pressure (BHP), in which pressure above MMP pressure (~2500 psi) means CO_2 and oil are under miscible conditions.

The base reservoir model for each studied case (i.e., the model with ML/EXP compaction table and no compaction table) was initially run under natural depletion condition for 5475 days (15 years). The production well was subjected to the minimum bottom-hole pressure of 500 psi. As expected, in the natural depletion scenario, the production well initially started with a high production rate and followed a sharp decline until a significantly low rate, as shown in Figure 5-3.

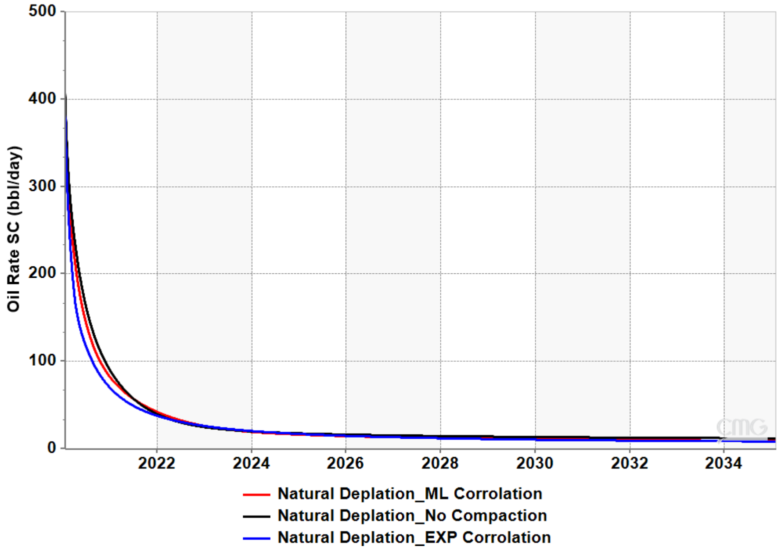

Fig. 5-3. Decline oil rate under primary depletion for cases 1, 2 and 3

This is the typical trend observed in most unconventional reservoirs. Also, if the stress-dependent permeability is considered, compared to the case with no compaction table, the permeability and oil production will be further reduced during the depletion period. Additionally, based on cases 1 and 3 (Table 5-4), the production loss is dependent on the selected permeability correlation models (e.g., ML and exponential).

5.4.1.1. Simulation Procedures

To investigate the effect of time on CO_2-EOR performance, CO_2 at different times during the production-well life was injected. In the first scenario, CO_2 huff and puff process in each case started when stimulated reservoir pressure (Figure 5-4) approached 4000 psi (above critical pressure). In the second scenario, the CO_2 injection started at 2800 psi, in the range of critical pressure and miscible CO_2. In the third scenario, injection at 2500 psi was chosen as it is lower than critical stress and CO_2 is still miscible. Forth scenario was done by injecting at 1500 psi where reservoir pressure approaches beyond critical pressure and CO_2 is not miscible anymore. As shown in Figure 5-4, stimulated reservoir volume is the major area for oil production. The rest of the reservoir had not been affected by the production well because the drainage area around the wellbore was very limited due to the tight formation.

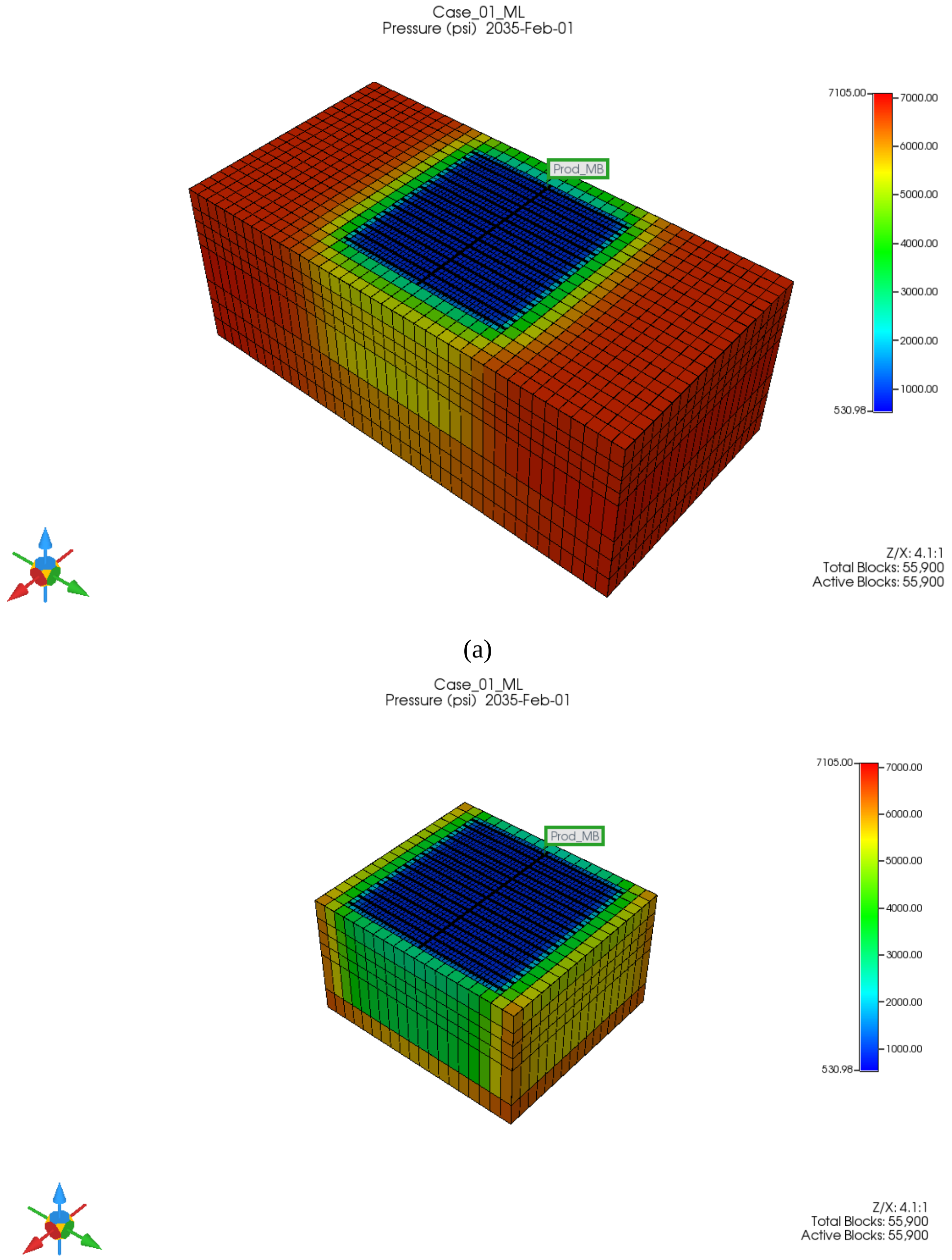

(a)

(b)

Fig. 5-4. Pressure disturbance in (a) Single-stage (b) stimulated reservoir

An optimum EOR strategy with five cycles of huff and puff for 30 days injection with the rate of 283,160 m^3 (10 MMscf) per day, 10 days soaking, and 30 days production was applied for CO_2-EOR performance. Table 5-4 summarizes several modeled cases in this study under above mentioned conditions.

Table 5-4. Different simulation cases studied in this study

Case	**1**	**2**	**3**	
Permeability-pressure correlation	ML	No Damage	EXP	
Injection Scenario	A) Before Critical Pressure – 4000 psi	B) During Critical Pressure – 2800 psi	C) After Critical Pressure – 2500 psi	D) After Critical Pressure – 1500 psi

5.4.1.2. Results and Discussion

In order to have a consistent comparison of all three proposed models, incremental oil percentage for each scenario after 3, 5, and 10 years of injection cycles end were calculated. Figure 5-5 illustrates oil production for the case by considering the compaction effect using ML correlation and four different injection scenarios based on Table 5-4.

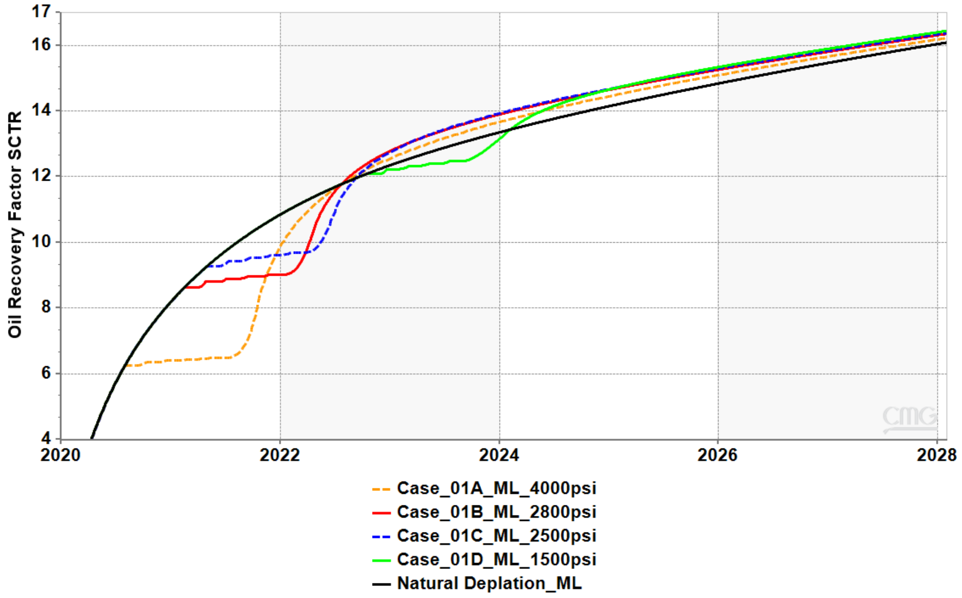

Fig. 5-5. Oil recovery factor for cases 1, 1.A, 1.B, 1.C, and 1.D

One of the most important criteria in designing a gas cycling scenario is the ideal time to start the operation. For all cases, it is observed that delaying the start of gas cycling with a more depleted reservoir is beneficial to production. This is mainly caused by the larger volumes of CO_2 that can be injected into the reservoir later due to depressurization of the stimulated reservoir region (Sanaei et al., 2018). However, cases with different permeability behavior under loading/unloading do not show a similar trend in incremental produced oil.

Based on Figure 5-6, injecting CO_2 at/near-critical pressure (i.e., 2800 and 2500 psi) shows higher incremental oil at the early injection time compared with injection at 1500 psi. While at a later time (10 years), where the effect of injection cycles ceased, incremental oil will reduce to lower than the case at 1500 psi.

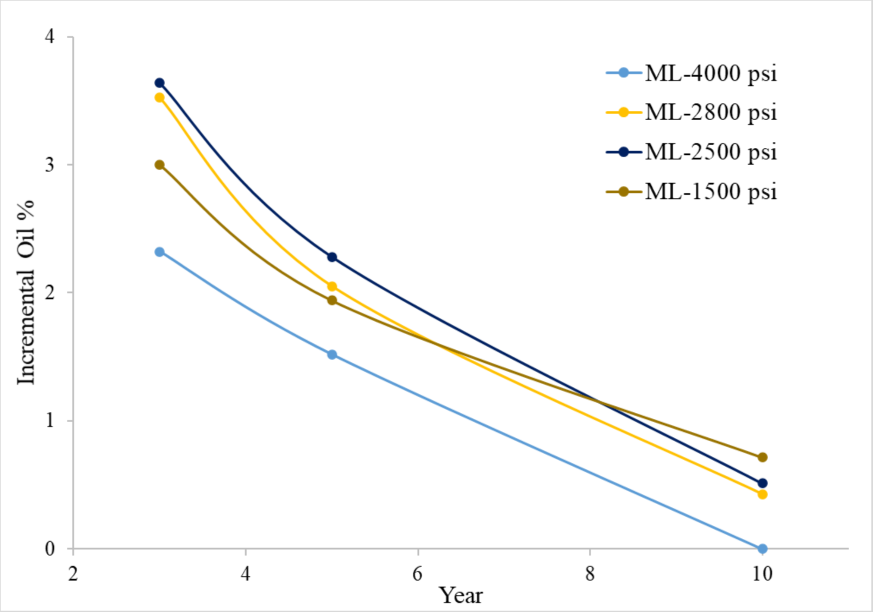

Fig. 5-6. Incremental produced oil over time-Case 1

Several mechanisms contribute to incremental oil recovery in the gas cycling process. Re-pressurization and oil swelling are the main mechanisms in this process (Alfarge et al., 2017). During the early time of injection, repressurizing would help enhance permeability along with oil swelling due to the interaction of oil and CO_2. Based on CO_2 injectivity behavior, the injected

CO_2 can initially flow in a high permeability medium as the permeability value has retrieved around the wellbore. Therefore, these two mechanisms could increase oil production from the stimulated region, and recovery can rise in a short time as high oil volume can be displaced.

Also, after a certain time of production, where reservoir pressure is decreased to a lower amount of critical pressure (less than 2800 psi), sharp permeability reduction causes a decrease in incremental oil production over time. While in the case with injection at 1500 psi, when pore-pressure reaches a certain value and permeability hits the plateau, the slight change of permeability will not make obvious differences on the incremental and cumulative production anymore. The oil production process at the injection of 1500 psi is mainly dependent on oil swelling, and permeability alteration will not occur over time.

For the case without any permeability change, where permeability is not decreasing during depletion (Case 2), re-pressurization and oil swelling as the main mechanisms in this process would increase oil recovery. As the reservoir is depleted more, it is expected that high injection CO_2 would diffuse easier to a matrix and can increase oil recovery by decreasing oil viscosity and oil swelling (Figure 5-7).

On the other hand, the case with exponential permeability decline (Case 3) does not consider any critical effective stress, and permeability reduction will be continuous under lower reservoir pressure. The results confirmed the prediction that CO_2 would perform better in cases that have earlier CO_2-EOR rather than the cases with low reservoir pressure at a late time, as shown in Figure 5-8. This could be explained by the exponential behavior of permeability evolution, which is significantly important to control the matrix permeability at low reservoir pressure in shale oil reservoirs

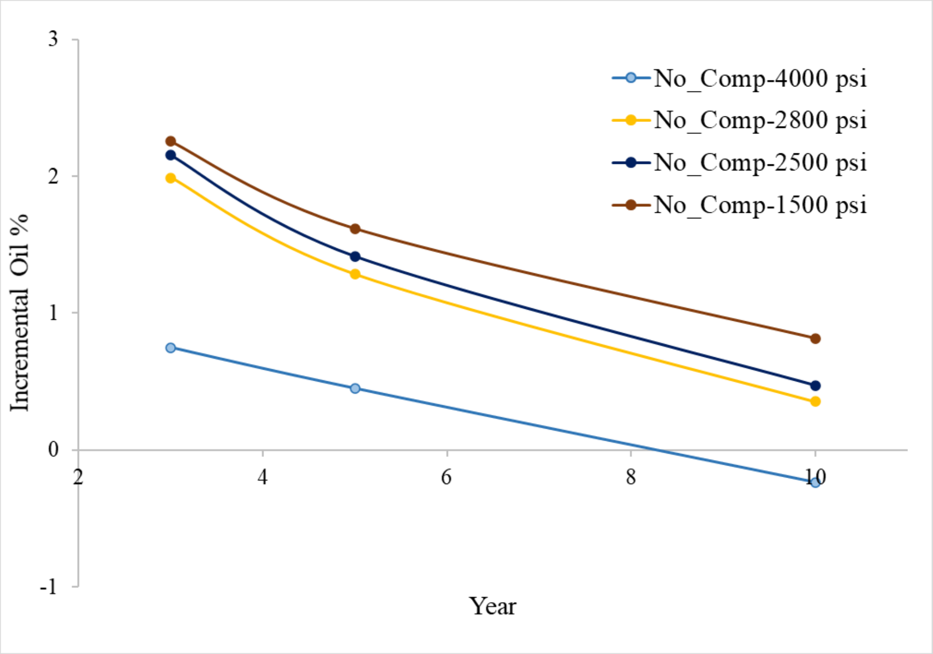

Fig. 5-7. Incremental produced oil over time-Case 2

.

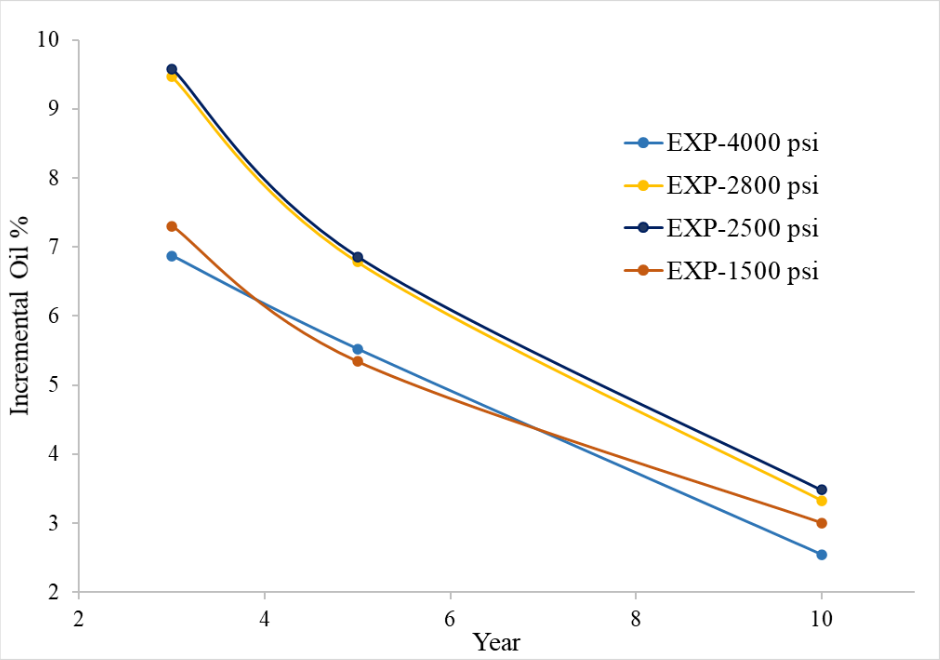

Fig. 5-8. Incremental produced oil over time-Case 3

An early CO_2-EOR application improves the performance because the injected CO_2 would find a more permeable flow path which helps in enhancing its diffusivity into formation oil. CO_2 at lower reservoir pressure is not miscible anymore, and permeability reduction continuously occurs at low reservoir pressure, leading to a significant decrease in oil production. While in real cases, based on the experimental results, permeability alteration does not occur after critical effective stress. Therefore, it is expected that permeability reduction does not impact oil production. As a result, exponential permeability decline cannot predict oil production under high effective stress correctly.

In addition, comparing different scenarios for three cases (Figure 5-9) shows exponential behavior would overestimate the incremental oil. This can be due to continuous change of permeability during the production/injection process, while permeability evolution is not considered or is limited in two other cases.

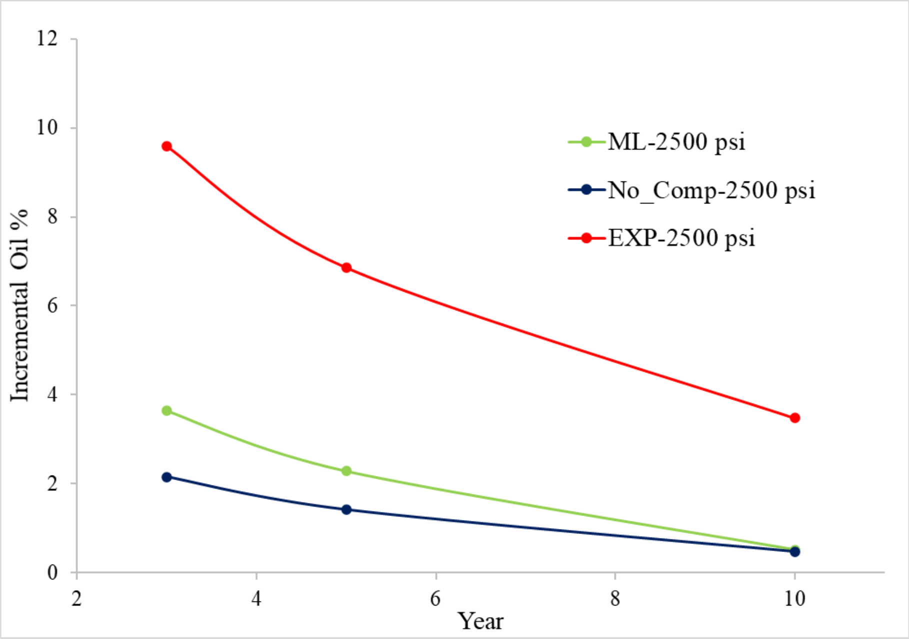

Fig. 5-9. Incremental oil prediction for studied cases (1,2 and 3C)

Although the presented model is simplified the well location and fractures, it can indicate general behavior of CO_2 injection in the presence of various permeability evolution. As the results showed, the oil recovery prediction caused by the stress-dependent permeability highly depends on the selected correlation. Neglecting permeability variation can cause unreliable predictions for CO_2-EOR, consequently affecting oil design patterns in the future. Selecting appropriate permeability correlation for different porous media is essential to predict the compaction behaviors and the permeability change in tight oil reservoirs.

It should be pointed out that all cases were evaluated based on rich gas scenarios. The results were similar to the findings from CO2 EOR. The evaluation of different gas injection impacts is out of this study's scope. Due to the CO2 cost, supply and presenting real field scenarios the rest of the investigation is based on rich gas injection performance.

5.4.2. Bottom Hole Pressure Variable Regions

The methodology presented in this study mainly focuses on developing reservoir simulation models with different pressure conditions. These models include a general Bakken geologic model and single-fracture-stage model and a DSU model with a Discrete Fracture Network (DFN). The goal was to investigate flow behavior in tight reservoirs to predict gas injection EOR performance by simulating different gas injection scenarios. Fundamental reservoir properties, including porosity, permeability, pore throat size, and mineral composition, etc., for the Bakken and Three Forks Formations was also used to support the modeling efforts. A gridding-based planar fracture model and DFN were used to construct the fracture matrix grid blocks in the models.

In order to mimic the real field well behavior and investigate different bottom hole pressure regions (i.e., region 1 to 3), permeability evaluation was continued using an advanced simulation modeling by importing the geologic model and setting up the associated reservoir petrophysics, rock types, and initial conditions. The simulation modeling was employed for the single fracture stage of the Middle Bakken well, in Williston County. A gridding-based planer hydraulic fractures and discrete fracture network (DFN) were used to model permeability change and historical fluid production. Understanding the current reservoir conditions by history matching the total fluid production would provide higher confidence in gas injection prediction. The history matching was conducted for the oil, water, and gas rate on a field scale following the fracture analyses. The study area consists of one well. The reservoir model, including the permeability-pressure curves for matrix, natural and hydraulic fractures, was substantially tuned during the history matching process concerning the wells fluids production. A 3D illustration of the reservoir simulation model is shown in Figure 5-10.

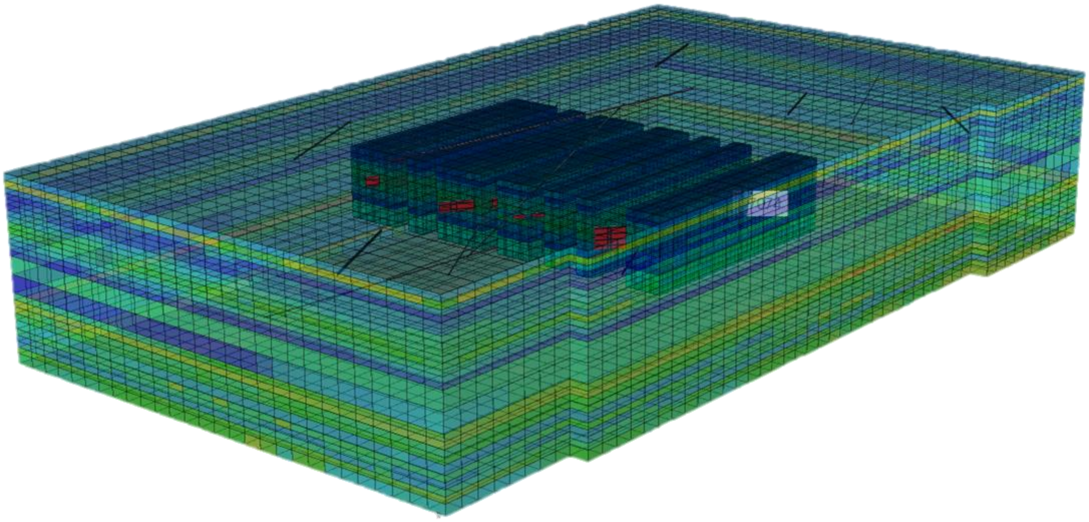

Fig. 5-10. 3D illustration of the reservoir simulation model

A set of genetic reservoir relative permeability curves generated using Brooks-Corey correlation was used, which was later tuned through the history matching process. Table 5-5 shows the general properties used for the numerical simulation analysis. The simulation results were aimed to provide a mechanism to assess the technical feasibility of produced gas injection at the potential pilot project site. The analysis of permeability evaluation associated with several injection scenarios provides a comprehensive insight into a produced gas injection performance in the Bakken formation to find an optimum gas injection time.

Table 5-5. Properties of modeled Middle Bakken and Three Forks Formations used for simulation griding

	Middle Bakken	**Three Forks**
Thickness (ft)	65	80
Average Porosity (%)	5	6.5
Average permeability (md)	0.005	0.02
Average Sw (%)	40	60
Oil Gravity (°API)	47	47
Average pressure gradient (psi/ft)	0.68	0.7

5.4.2.1. History Matching

A base model was created for the history matching efforts to validate the model using the existing historical production data. A Black-oil Simulator IMEX from CMG (Computer Modelling Group Ltd.) was used for this process. Utilizing the black-oil simulation can reduce the computational time for depletion production while maintaining simulation accuracy. Data of the target well located at the field of interest (i.e., MB-PROD) was collected from public domains such as North Dakota Industrial Commission (NDIC) and integrated into this simulation model in preparation to conduct a history matching process. History-matching involves tuning the reservoir model to match the production history of wells. Once a reasonable history match was obtained, the model was used for evaluating the potential gas injection scenarios and designing the optimum injection well patterns.

5.4.2.2. Equation of State (EOS) Model

The compositional simulation model was utilized to evaluate the injection EOR process. The fluid PVT model was generated in CMG's WinProp, a fluid property characterization tool and allow the simulation to be able to predict the injection of produced gas with different gas compositions. A set of generic pressure, volume, and temperature (PVT) test data from the previous Bakken studies were used in the simulation model development (Kurtoglu, 2013 and Jin et al., 2017). Since majority of produced gas composition consists of light gas components, the lighter gas components (i.e., N_2, CO_2, C_1 to C_4) were kept separate, and the heavier oil components (i.e., C5+) were lumped into three pseudo-components. The Equation of State (EOS) was adjusted to match the available lab-tested parameters, such as saturation pressure, differential liberation (DL), and constant composition expansion (CCE). Then the 9-component PVT model was used for gas injection evaluation. Tables 5-6 indicates the simulated injection gas composition used in the model. More details of the EOS study are brought in by Kurtoglu, 2013 and Jin et al., 2017.

Table 5-6. Injected gas compositions used in the simulation model

Component	N_2	CO_2	CH_4	C2	C3	IC4-NC4
Mole Fraction, %	3	1	60	20	10	6

5.4.2.3. Single Fracture Stage Modeling

A compositional reservoir simulation model with main hydraulic, induced and, natural fractures was developed using the geologic/reservoir properties, EOS through GEM-CMG. The model consisted of four formations of Upper Bakken (UB), Middle Bakken (MB), Lower Bakken (LB), and Three Forks (TF) Formations with a total layer of 26. One well was included in the simulation model. Because of the large number of fracture stages along the wellbore of each well, one fracture stage was utilized to reduce heavy computational load. The cluster efficiency reduced up to 60% after tunning the model as illustrated in Figures 5-11.

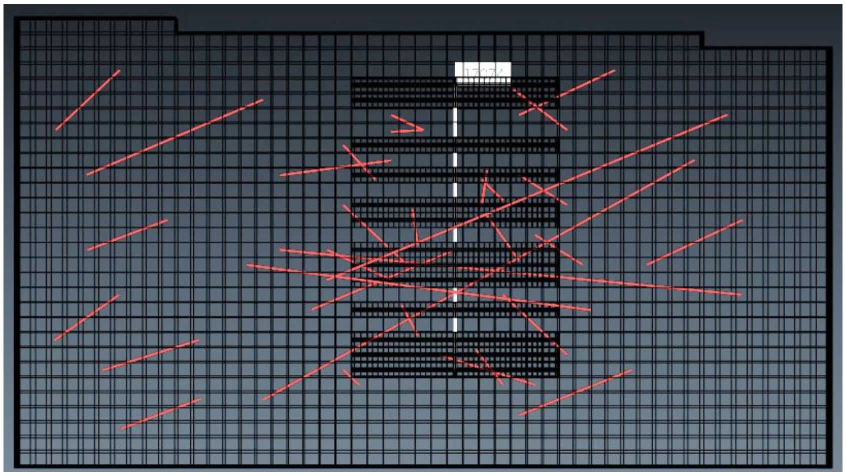

Fig. 5-11. Top view - NFR, induced and hydraulic fractures

The planer hydraulic fracture with refined gridding approach was modeled for each well, assuming an identical fracture in each stage. Hydraulic fractures were created along the wellbore based on the assumption fracturing data.

In tight reservoirs, such as the Bakken Fm., the main fluid flow path would be micro-cracks which can be closed from elevated stresses during the depletion. As several authors mentioned in their work, stress exerted on core samples can lead to permeability reduction by various mechanisms such as closing microcracks, rearrangement of grains, and crushing existing pores (Morris et al., 2003; Civan, 2017). Conversely, it might improve permeability by creating new cracks and opening conduit paths in core samples (Zoback and Byerlee, 1975; Paterson 1978, Morris et al., 2003, Civan, 2017). Therefore, proper modeling of fracture geometries can play a crucial role in modeling the fluid flow and incremental oil recovery. However, fracture networks' presence and complexity make unconventional modeling challenging with traditional simulation approaches. Dual porosity and dual permeability methods are common methods used in modeling. These models utilize a simple assumption of orthogonal fracture networks, leading to the low accuracy of these types of methods (Warren and Root, 1963; Yu et al., 2014). On the other hand, local grid refinement (LGR) and unstructured grid methods, which can simulate complex fracture geometries by including numerous and complicated grid structures, possess large computation load (Conlin et al., 1990; Choi et al., 1997; Mirzaei and Cipolla, 2012).

In this study, A high-efficient fracture stimulation technique— Discrete fracture network (DFN) technique —was used to set up complex fractures including natural and induced fractures in the simulation model. Figure 5-11 shows that the final DFNs were added to the simulation model. The properties of DFN, such as permeability and aperture, etc., were adjusted during history-matching process (Easley, 2014, Strum and Gomez, 2009). Table 5-7 shows the range of DFN parameters used in this study during the history matching process.

Table 5-7 – Different reservoirs regions and possible injection scenarios

	Range	**Final Model**
Theta (degree)	0-100	30-50 (NFR) 90-100(IF)
Permeability (md)	1-1000	1-900
Number of Fractures	15-42	32
Aperture (.in)	0.001-0.01	0.001
Dip	70-90	70-90

High-stress dependency of the Bakken shale porous media leads to significant permeability evolution during reservoir effective stress changes. During the production stage, the reservoir gradually loses its original pore pressure, and net effective stress increases. Consequently, a reduction in reservoir properties, such as permeability or porosity, can occur in response to net stress change within the pores due to the withdrawal of the fluids from the reservoir. Therefore, to include this behavior, the exponential, and separated exponential pressure-dependent permeability, and porosity used in this simulation course and shown in Figure 5-12. The models are adjusted based on history matching results and obtained the same pressure response for sake of comparison. It should be noted that using a machine learning model from one well data (Chapter 4) is not applicable due to the complexity of the model. Therefore, a separated exponential model for each medium (i.e., matrix, natural fractures, and hydraulic fracture) was used – the description of the separated exponential model can be found in Chapter 3 of this thesis.

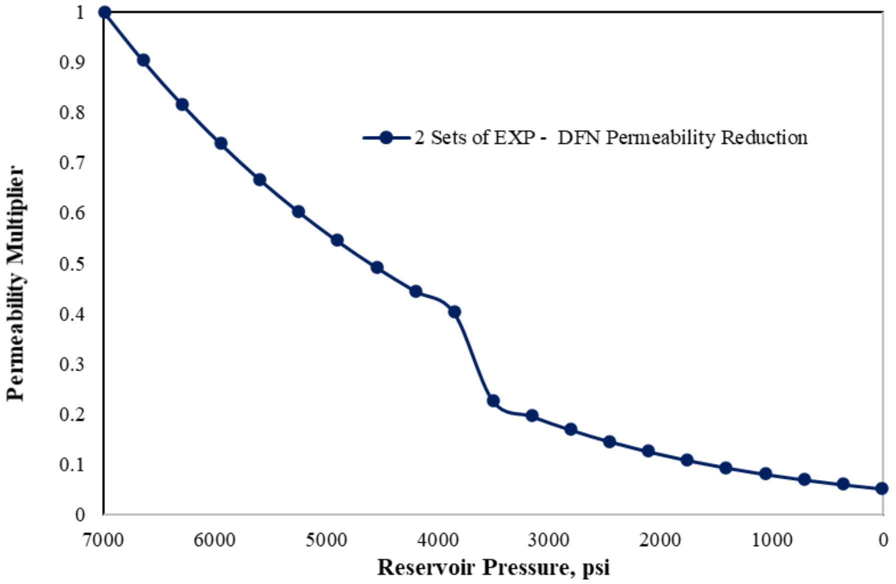

Fig 5-12. History matched DFN Pressure dependent permeability – 2 sets - Exponential models before and after critical effective pressure

5.4.2.4. History Match and Simulation Results

Due to the high production of oil and gas during primary production, acute pressure depletion can occur in Bakken wells. Matrix and fracture properties such as permeability-pressure curves were modified to mimic well fluid production history. So, the permeability-pressure coefficient of the fractures for each model (i.e., exponential and two sets of exponentials) is modified for three different regions of the matrix, natural fracture, hydraulic, and associate induced fractures. The history matched permeability reduction is shown in Figure 5-12. Example results of fluid rates history matching up to the year 2019 for the target EOR well, and the pressure decline is presented in Figure 5-13.

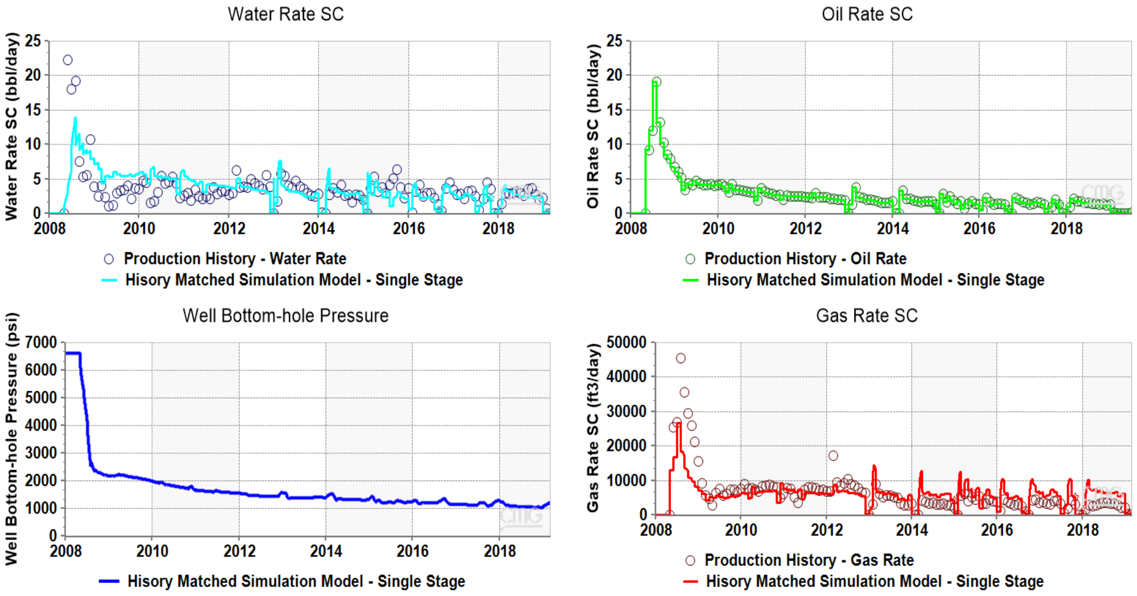

Fig 5-13. Results of history matching model for well MB-PROD

The results indicated that the model could capture the flow dynamics to a reasonable degree. Once a good history match was obtained, the model was used to evaluate the potential injection performance and design the optimum injection scenario. Results of several reservoir simulation case studies are used to explore methods for characterizing the recovery mechanism and EOR performance of rich gas injection single-well at different states of well bottom hole pressure.

5.4.2.5. EOR Forecasting

A series of simulation efforts were employed to evaluate the EOR performance at different well life stages. The analysis of EOR performance can provide an insight into the optimal time of the gas injection in the Bakken formation and associate permeability change effect. Bottom hole pressure based on pressure response is divided into three regions for each permeability-pressure curve (Figure 5-14). The continuous and huff and puff test with several injection configurations were tested.

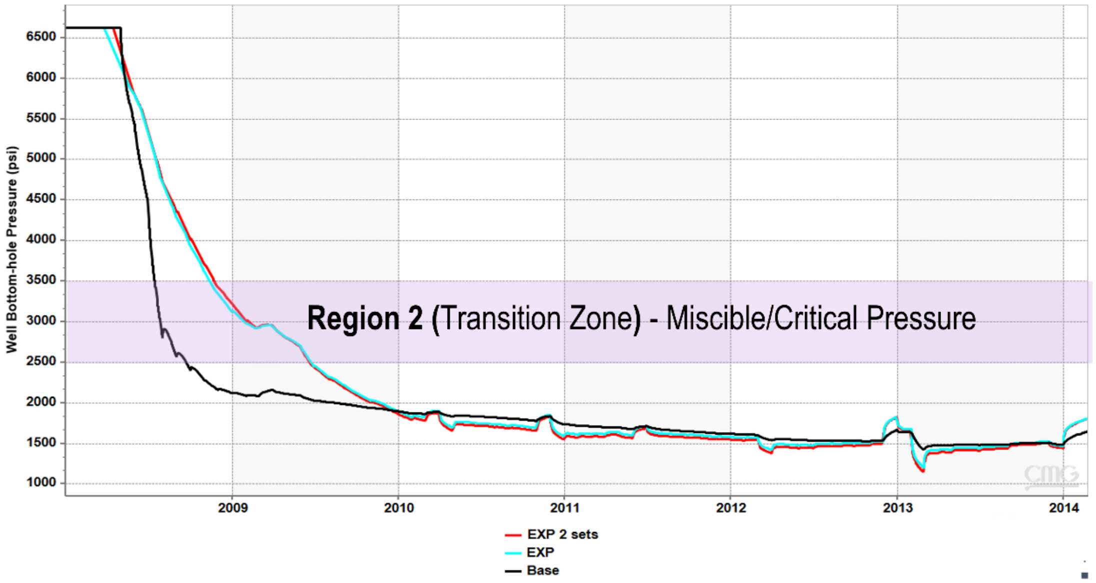

Fig. 5-14. Bottom hole pressure response from three different permeability correlations (1. No permeability change, 2. exponential 3. Two sets of exponentials before and after critical pressure)

The optimum cases in terms of recovery and running time were selected for further for evaluation of the EOR performance at a different time with 3 permeability correlation models (Table 5-8):

Table 5-8. Optimum injection case selected for this study

Case ID	Region (reservoir statues)	Injection Scenario	Gas Rate	Injection-Soaking-production time	Cycle
1	1	Huff n Puff	1 MMscfd	30 days	2
2		Continuous	1 MMscfd	60	1
3	2	Huff n Puff	1 MMscfd	30 days	2
4		Continuous	1 MMscfd	60	1
5	3	Huff n Puff	1 MMscfd	30 days	2
6		Continuous	1 MMscfd	60	1

During the EOR evaluation, a wide variety of different injection cycles, injection volumes, pressures, and injection fluid compositions were evaluated. A detailed discussion of the simulation parameters, assumptions, and approaches is beyond the scope of this research. The

EOR scenarios described and discussed below were selected to serve as illustrative examples that predict how permeability modeling may affect EOR operations in a Bakken reservoir.

Injection/production scenario tests of huff and puff and continuous injection at region one when BHP is above 3500 psi for all three models suggest that both EOR methods would not result in significant oil recovery improvement compared to the case that continues using primary depletion production. The results are expected and discussed in the previous section when well is at region 3 and DSU at region 1. As the results in the huff and puff process show (Figure 5-15), using the model where critical effective pressure is integrated, predicted higher incremental oil while two other models are slightly lower. On the other hand, the prediction of the huff and puff process in region 3 suggests an exponential model with higher oil recovery compared to the model with two sets of permeability correlation. This was expected since pressurizing the well using an exponential model will cause a gradual increase in permeability change while in model with effective pressure- permeability change at this region requires higher pressure build-up.

Overall, when DSU is under region 1 and wells are in variable regions, the huff and puff process did not show significant improvement in incremental oil after 4 years of production. However, continuous injection at regions 2 and 3 due to higher pressure build-up, more chance of miscibility of gas during the injection and permeability retrieve (Figure 5-16).

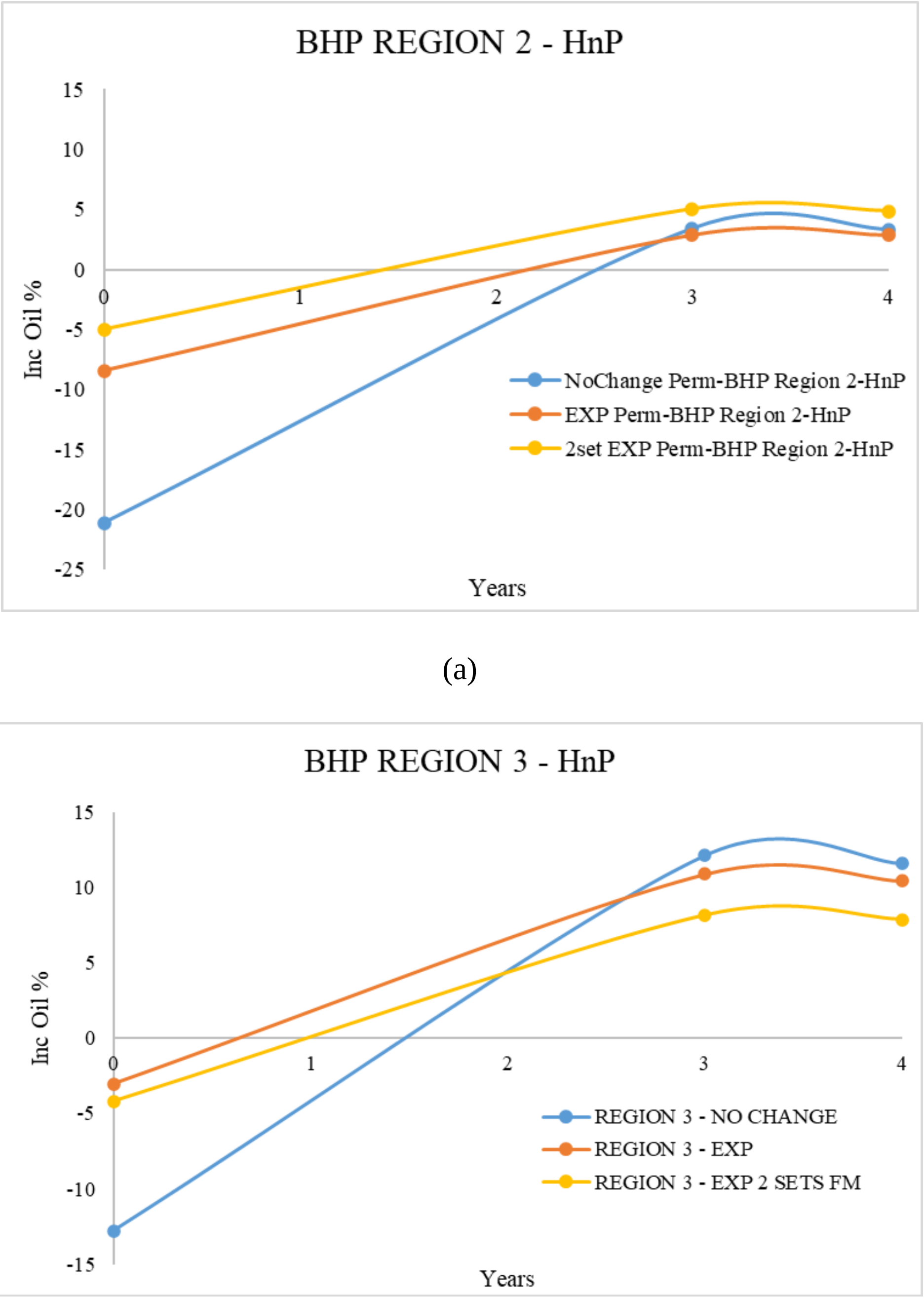

(a)

(b)

Fig. 5-15. Incremental oil of all three models during regions 2 and 3: (a) BHP at region 2 (b) BHP at region 3

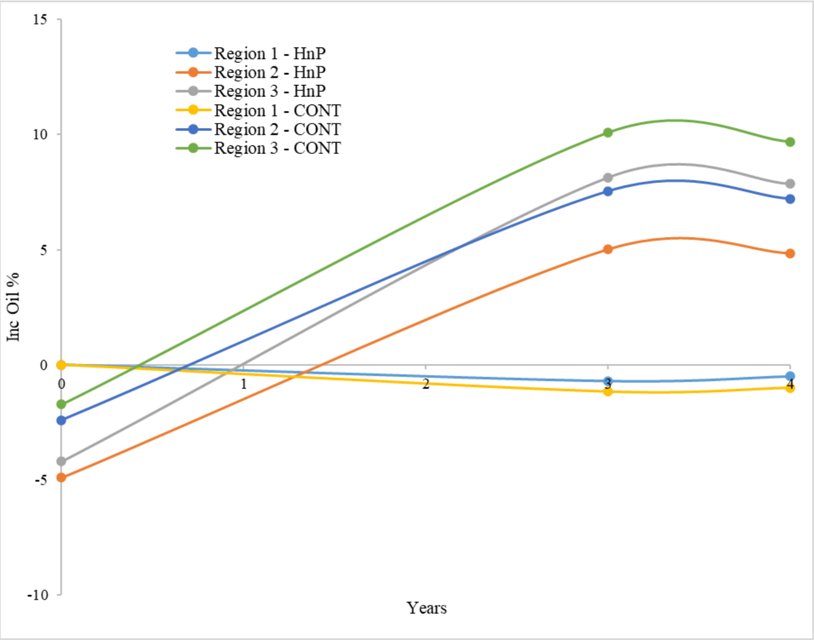

Fig. 5-16. Incremental oil of all two sets of the exponential model during huff and puff and continuous gas injection

Therefore, the injection scenario is highly dependent on reservoir pressure and the degree of DSU depletion. If the initial BHP is low (Region 3) and DSU is partially/fully depleted (i.e., in region two or three), the continuous injection would not be able to pressurize the formation enough to observe a significant EOR effect due to permeability change. However, gas huff and puff would be the better option since the near miscibility/miscibility mechanism can reduce oil viscosity and improve oil recovery. Based on Table 5-9 and obtained oil recovery, the best time to start a huff and Puff process would be at well pressure of region 3 and DSU of region 2 and 3.

Table 5-9 – Different reservoirs regions and possible injection scenarios

	BHP - Region 1	**BHP - Region 2**	**BHP - Region 3**
DSU- Region 1	No action	Continuous Injection	Continuous Injection
DSU- Region 2		N/A	Huff n Puff
DSU- Region 3			Huff n Puff

Further optimization can be done toward higher oil recovery by the increasing cycle of injection, the volume of gas injection, and adding soaking. However, higher injection rates seem to lead to higher production rates, but there is a limit to how much can be injected. Also, the injection cases produce lots of water and gas, which can be problematic and expensive to deal with operationally. Economic considerations will determine which injection strategy would be the best to implement.

5.5. Summary and Conclusions

- The general permeability alteration effect on CO_2-EOR oil recovery is evaluated. A synthetic reservoir model was built to investigate the impact of stress-dependent permeability on oil production performance. Several stress-permeability correlations were chosen to separately apply to the Bakken and Three Forks matrix based on their rock properties and compaction behaviors. Although these values might not reflect the real field data, they can be useful sources to show the noticeable effect of permeability evolution in tight reservoirs under different EOR conditions.
- Compared to the model without considering stress-dependent permeability, the cumulative production could reduce because the permeability decreases along with reservoir pressure decline. Compared to the model with exponential permeability decline, the production loss caused by the stress-dependent permeability varies based on the selected correlation.
- The study of operational parameters indicated that an optimum time for the start of gas cycling depends on the permeability behavior under reservoir depletion. However, all models showed that beginning the gas cycling operations too early in the life of the well will negatively affect the EOR performance.
- Based on numerous past studies and this work, it is evident that lab measurements and field data are required to highlight the role of permeability-pressure change,

critical effective stress, in order to predict reservoir behavior close to reality. Selecting appropriate permeability correlations for different porous media is critical to better describe the compaction behaviors and predict the permeability decline over the reservoir depletion. If proper stress-dependent permeability is not considered, the hydrocarbon production will be significantly overestimated/underestimated, leading to unwise management decisions.

- An advanced single-stage simulation modeling including geologic/reservoir characterization, EOS tuning, fracture modeling, history matching, and EOR scenarios development was employed in this study to characterize BPS in the target Middle Bakken and Three Forks formations. The model matched primary depletion and predicted EOR scenarios for a different types of permeability behavior.
- The injection scenario is highly dependent on reservoir pressure and the degree of DSU depletion. If the initial BHP is low (Region 3) and DSU is partially/fully depleted (i.e., in region two or three), the continuous injection would not be able to pressurize the formation enough to observe a significant EOR effect due to permeability change. However, gas huff and puff would be the better option since the near miscibility/miscibility mechanism can reduce oil viscosity and improve oil recovery. Based on Table 5-9 and obtained oil recovery, the best time to start a huff and puff process would be at well pressure of region 3 and DSU of region 2 and 3.

CHAPTER 6

CONCLUSIONS AND RECOMMENDATIONS

In this study, the permeability of some Bakken core samples was measured under various cases of loading/unloading effective-stress conditions. The permeability-stress sensitivity, critical effective stress, and average permeability damage were evaluated under short- and long-stress ranges, different pore pressures, and effective porosities. The effect of permeability change under different reservoir pressure on gas injection scenarios was studied in detail as part of this research project. The first section of this chapter lists the main conclusions made from this work and the second section presents some of the future work that is recommended as a continuation of this study.

6.1. Conclusions

From this study the following conclusions are drawn:

- The exponential permeability model can well describe the permeability measurement data of Bakken core samples through straight lines on the semi-log plot of permeability vs. effective pressure. From such plots, observations are made to identify the impact of critical effective stress on permeability sensitivity and average formation damage.
- Permeability continuously declines upon loading the sample and does not fully retrieve during unloading. The rate of permeability reduction changes beyond a certain point referred to as critical effective stress. Moreover, this research

experiment reveals that the span of loading/unloading stress has a direct impact on the hysteresis distance and average permeability damage. However, after the critical effective stress, there would be no significant change in the permeability and hysteresis and permeability recovery is almost zero. In other words, injection of fluids at any high pressure would not help the collapsed cracks and crushed grains to re-open, thus leading to lower production. Therefore, it is recommended that the critical effective stress be determined in the lab which helps us better design, optimize, and execute successful and timely-planned pressure maintenance and EOR treatments.

- Based on the conducted experiments it is shown that the length of loading/unloading pressure has a direct effect on hysteresis distance. But after reaching the critical stress point, there is no significant change in permeability and hysteresis. Therefore, the majority of changes happen before this point, which indicates that finding critical stress for each field can help to improve early injection decisions for pressure maintenance.
- The effect of pore pressure on the Bakken core samples is studied in this work. As the results illustrate, higher pore pressure in an early stage of a reservoir (i.e., low confining pressure) can have a positive impact on improving formation damage. However, in higher effective stress the effect is not significant. This can be considered another important behavior that leads to early injection in reservoir management.
- Comparing two different cores with various PSDs, proves that the heterogonous sample has slightly larger hysteresis. However, low effective porosity and pore sizes in homogenous samples cause lower permeability due to more sensitivity to stresses.

Therefore, both heterogeneity and pore sizes can affect hysteresis behavior and need to be considered during permeability hysteresis.

- The effect of pore pressure on permeability hysteresis is investigated in this research. The results demonstrate that at the early stages of production in unconventional reservoirs where pore pressure is higher (i.e., lower confining stress), the relapse of permeability has a better chance than that during the late time after the depletion has started. In higher effective stress increasing pore pressure has a negative impact on improving formation damage. This observation highlights the significance of optimal time injection for better EOR outcomes.
- With regards to the pore-size distribution, permeability hysteresis becomes more notable as the heterogeneity of samples is more significant. Comparing two different cores with various PSDs, concludes that the heterogonous sample has slightly larger hysteresis. However, low effective porosity and pore sizes in the homogenous sample can cause lower measured permeability and higher permeability reduction rate. Therefore, the permeability behavior in Middle Bakken core samples is mainly controlled by the pore size distribution, heterogeneity, and micro cracks.
- From the experiments a 50% reduction of the stress-sensitivity coefficient is observed, during both loading and unloading, when the applied stress approached the critical effective stress. Comparing stress sensitivity during loading with unloading results, show a reduction in permeability stress dependency during un-loading. Also, higher pore pressures before reaching the critical effective stress may cause greater sensitivity of permeability to effective-stress change.

- Before approaching the critical points, a direct relationship between stress dependency and permeability damage is observed, for the same core sample with varying pore pressure. However, this relationship would flip for the core sample with different porosities. This implies that stress sensitivity is not the only parameter controlling the permeability evolution.
- Due to limited laboratory conditions, stress sensitivity evaluation is not fully reflecting the reservoir conditions where stress relief or drilling-induced fractures can happen. Besides, the hysteresis phenomenon occurs based on several complicated processes, such as elastic and plastic deformation, contraction, shearing, compaction, and the like. Therefore, for a more accurate investigation, actual reservoir conditions need to be simulated as much as possible.
- A machine learning (ML) technique, specifically, an artificial neural network (ANN) algorithm, is employed over the entire set of formation depths. The model is trained over the variation of core sample properties, including rock density, porosity, and grain volume, to improve the permeability-stress correlation. This approach generated a model that can accurately predict the permeability change versus effective stress for entire depths, using only one equation. After the critical stress point, permeability change is not significant, which could be captured using an ML model. In contrast, an exponential model shows a continuous decrease in permeability at high effective stress. This inconsistency in exponential model results makes the ML method the best choice to obtain an accurate permeability-stress correlation in tight oil reservoirs.
- Although ANN algorithm over one set of well data showed promising results and accurate permeability prediction, the permeability prediction error for core data of

several wells is not low. Training the model does not cover the variation of data in wide range, higher permeability values are underestimated and R^2 is not reliable. Therefore, decision tree regression due to small range of investigation interval are better approach to capture the permeability trend.

- The general permeability alteration effect on gas EOR oil recovery is performed through the Bakken/Three Forks reservoir model simulation. Several stress-permeability correlations are chosen to separately apply to the Bakken and Three Forks matrix based on their rock properties and compaction behaviors.
- Compared to the model without considering stress-dependent permeability, the cumulative production could reduce because the permeability decreases along with reservoir pressure decline. Compared to the model with exponential permeability decline, the production loss caused by the stress-dependent permeability varies based on the selected correlation.
- If the permeability enhancement is intended in an injection process, it should be done before reaching the critical point. A higher bottom hole pressure could compensate for the certain production loss caused by the permeability decline, while it is not the best strategy in terms of final oil recovery.
- Integrating the permeability alteration over well life production, leads to defining three new regions with respect to critical effective pressure and miscibility of gas injection. The transition region in which critical effective pressure and miscibility are active is counted as a crucial time for starting gas huff and puff. This necessitates finding the critical points in each operating field and thus an optimal time of injection to improve the decision-making for EOR operations and reservoir management.

6.2. Recommendations

Namouras ideas and potential applications of permeability model were mentioned throughout this study, which require further investigations. Here, some of these ideas are recommended as continuation of this study:

- It would be useful if data from field studies are used to verify results of simulations and analytical studies from literature.
- The opportunity to develop a wide range of permeability-pressure coefficient data in Bakken/Three Forks that can be used as reference in reservoir modeling. Other labs and industries would benefit as more analysis can be done through the available core data. Utilize reliable model to fill the gap between oil recovery results in both lab and field-scale
- Based on numerous past studies and this work, it is evident that lab measurements and field data are required to highlight the role of permeability-pressure change, critical effective stress in order to predict reservoir behavior close to reality. Selecting appropriate permeability correlations for different porous media is critical to better describe the compaction behaviors and predict the permeability decline over the reservoir depletion. If proper stress-dependent permeability is not considered, the hydrocarbon production will be significantly overestimated/underestimated, leading to unwise management decisions.
- It is highly recommended to couple geomechanics with reservoir fluid flow to capture permeability change under stress evolution. An accurate geomechanical model can provide more realistic dynamic flow prediction and a reliable long-term production

forecast via reservoir simulation for operators to design more effective enhanced oil recovery plans in the Bakken.

REFERENCES

Abuamarah, B.A., Nabawy, B.S., Shehata, A.M., Kassem, O.M. and Ghrefat, H. 2019. Integrated geological and petrophysical characterization of oligocene deep marine unconventional poor to tight sandstone gas reservoir. *Marine and Petroleum Geology, 109, pp.868-885.*

Alfarge, D., Wei, M., Bai, B. and Almansour, A., 2017. Optimizing Injector-Producer Spacing for CO2 Injection in Unconventional Reservoirs of North America. In SPE Kingdom of Saudi Arabia Annual Technical Symposium and Exhibition.

Alharthy, N., Nguyen, T., Teklu, T. et al. 2013. Multiphase Compositional Modeling in Small-Scale Pores of Unconventional Shale Reservoirs. Presented at the SPE Annual Technical Conference and Exhibition, New Orleans, 30 September–2 October. SPE-166306-MS. https://doi.org/10.2118/ 166306-MS.

Amaefule, J. O., Wolfe, K., Walls, J. D., Ajufo, A. O., & Peterson, E. (1986, January). Laboratory determination of effective liquid permeability in low-quality reservoir rocks by the pulse decay technique. In SPE California Regional Meeting. Society of Petroleum Engineers.

An, C., Killough, J. and Mi, L. 2019. Stress-dependent permeability of organic-rich shale reservoirs: Impacts of stress changes and matrix shrinkage. *Journal of Petroleum Science and Engineering, 172, pp.1034-1047.*

Angra, S. and Ahuja, S. (2017) “Machine learning and its applications: A review” in 2017 International Conference on Big Data Analytics and Computational Intelligence (ICBDAC). Chirala, Andhra Pradesh, India, IEEE, 57–60.

AutoLab 1500 Manual. 2009. New England Research Inc.

Assady A, Jabbari H, Ellafi A, Goudarzi B. 2019. On the Characterization of Bakken Formation: Oscillating-Pulse, Pulse-Decay Permeability Measurement & Geomeachanics. 53rd US Rock Mechanics/Geomechanics Symposium; American Rock Mechanics Association.

Assady, A. and Jabbari, H. 2020. Pore Size Distribution and Permeability Hysteresis in Unconventional Plays; Digital Rock Physics and Pulse Decay. In Proceedings of 54th US Rock Mechanics/Geomechanics Symposium, Colorado, 28 June - 1 July.

Bautista, J., Fidler, L., Crouse, B., Balasubramanian, G., Chen, H., Zhang, R. and Ghodke, C., 2018, September. A Validated Digital Rock Workflow to Accurately Predict Apparent Permeability in Tight Rocks. In Unconventional Resources Technology Conference, Houston, Texas, 23-25 July 2018 (pp. 3410-3417). Society of Exploration Geophysicists, American Association of Petroleum Geologists, Society of Petroleum Engineers.

Belyadi, Hoss, and Alireza Haghighat. Machine learning guide for oil and gas using Python. Vol.10. Gulf Professional Publishing. doi, 2021.

Bendix, P. B., Henninger, S. K., & Henning, H. M. (2016). Temperature and mechanical stabilities and changes in porosity of silicone binder-based zeolite coatings. *Industrial & Engineering Chemistry Research*, 55(17), 4942-4947.

Bernabe, Y. (1987). The effective pressure law for permeability during pore pressure and confining pressure cycling of several crystalline rocks. *Journal of Geophysical Research: Solid Earth*, 92(B1), 649-657.

Bertoncello, A. and Honarpour, M.M. 2013, September. Standards for characterization of rock properties in unconventional reservoirs: fluid flow mechanism, quality control, and uncertainties. In SPE Annual Technical Conference and Exhibition. Society of Petroleum Engineers.

Boualam, A., Rasouli, V., Dalkhaa, C. and Djezzar, S., 2020. Stress-Dependent Permeability and Porosity in Three Forks Carbonate Reservoir, Williston Basin. In 54th US Rock Mechanics/Geomechanics Symposium.

Brace WF, Walsh J, Frangos W. 1968. Permeability of granite under high pressure. *Journal of Geophysical Research*. 73(6):2225-36.

Cao, P., Liu, J. and Leong, Y.K. 2016. Combined impact of flow regimes and effective stress on the evolution of shale apparent permeability. Journal of Unconventional Oil and Gas Resources, 14, pp.32-43.

Chen C., D. Hu, D. Westacott and D. Loveless. 2013. Nanometer-scale characterization of microscopic pores in shale kerogen by image analysis and pore-scale modeling, Geochem. Geophys. Geosyst., pp. 4066 – 4075.

Chen, T., & Stagg, P. W. (1984). Semilog analysis of the pulse-decay technique of permeability measurement. Society of Petroleum Engineers Journal, 24(06), 639-642.

Chen, Z. A., Wu, X. Y., Fang, H., & Yang, W. (1999). Gas transit measurement method of permeability on rock.

Choi, E.S., Cheema, T., and Islam, M.R., 1997, A new dual-porosity/dual-permeability model with non-Darcian flow through fractures: *Journal of Petroleum Science and Engineering*, v. 17,nos. 3–4, p. 331–344.

Chu, L., Ye, P., Harmawan, I.S., Du, L. and Shepard, L.R. 2012, January. Characterizing and simulating the nonstationariness and nonlinearity in unconventional oil reservoirs: Bakken application. In SPE Canadian Unconventional Resources Conference. Society of Petroleum Engineers.

Chuan-liang, L. I. (2008). A misunderstanding in reservoir rock stress sensitivity-In reply to Dr Liu Xiao-xu [J]. Special Oil & Gas Reservoirs, 3.

Civan F. 2018 Compressibility, porosity, and permeability of shales involving stress shock and loading/unloading hysteresis. Unconventional Resources Technology Conference, Houston, Texas, 23-25 July 2018; Society of Exploration Geophysicists, American Association of Petroleum. doi: 10.15530/urtec2018-2902156.

Civan, F. (2000). Reservoir Formation Damage-Fundamentals, Modeling, Assessment, and Migration, Gulf Pub. Co., Houston, TX, 742p.

Civan, F. (2007, January). Formation damage mechanisms and their phenomenological modeling-an overview. In European Formation Damage Conference. Society of Petroleum Engineers.

Civan, F. (2017, October). Phenomenological Correlation of Pressurization/Depressurization Hysteresis of Stress-Dependent Porosity and Permeability of Shale Reservoirs. In SPE Annual Technical Conference and Exhibition. Society of Petroleum Engineers.

Civan, F., Rai, C. S., & Sondergeld, C. H. (2011). Shale-gas permeability and diffusivity inferred by improved formulation of relevant retention and transport mechanisms. *Transport in Porous Media*, 86(3), 925-944.

Conlin, J.M., Hale, J.L., Sabathier, J.C., Faure, F., and Mas, D., 1990, Multiple-fracture horizontal wells—performance and numerical simulation: Presented at the European Petroleum Conference, the Hague, Netherlands.

Cudjoe, S., Barati, R., Goldstein, R. H., Tsau, J., Nicoud, B., Bradford, K., ... & Mohrbacher, D. (2019, October). An Integrated Pore-Scale Characterization Workflow for Hydrocarbon Gas Huff-n-Puff Injection into the Lower Eagle Ford Shale. In Unconventional Resources Technology Conference, Denver, Colorado, 22-24 July 2019 (pp. 4760-4779). Unconventional Resources Technology Conference (URTeC); Society of Exploration Geophysicists.

Cui, X., Bustin, A.M.M. and Bustin, R.M., 2009. Measurements of gas permeability and diffusivity of tight reservoir rocks: different approaches and their applications. *Geofluids*, 9(3), pp.208-223.

Darcy H. 1856. Les fontaines publiques de la ville de Dijon: exposition et application: Victor Dalmont.

Das, S., Dey, A., Pal, A., and Roy, N. (2015) Applications of Artificial Intelligence in Machine Learning: Review and Prospect. *International Journal of Computer Applications*, 115(9), 31–41.

David C, Wong T-F, Zhu W, Zhang J., 1994. Laboratory measurement of compaction-induced permeability change in porous rocks: Implications for the generation and maintenance of pore pressure excess in the crust. *Pure and Applied Geophysics*, 143(1-3):425-56.

David, C. (1993). Geometry of flow paths for fluid transport in rocks. *Journal of Geophysical Research: Solid Earth*, 98(B7), 12267-12278.

David, C., & Darot, M. (1989, January). Permeability and conductivity of sandstones. In ISRM International Symposium. International Society for Rock Mechanics and Rock Engineering.

De Jong, S. M., Spiers, C. J., & Busch, A. (2014). Development of swelling strain in smectite clays through exposure to carbon dioxide. *International Journal of Greenhouse Gas Control*, 24, 149-161.

Devarapalli, R.S., Islam, A., Faisal, T.F., Mohamed, S. and Mustapha J. 2017. Micro-CT and FIB–SEM imaging and pore structure characterization of dolomite rock at multiple scales, *Arab J Geosci* 10: 361.

Dicker A, Smits R. 1988. A practical approach for determining permeability from laboratory pressure-pulse decay measurements. International meeting on petroleum engineering; Society of Petroleum Engineers. doi:10.2118/17578-MS.

Dong J-J, Hsu J-Y, Wu W-J, Shimamoto T, Hung J-H, Yeh E-C, et al. 2010. Stress-dependence of the permeability and porosity of sandstone and shale from TCDP Hole-A. International *Journal of Rock Mechanics and Mining Sciences*, 47(7):1141-57. doi: 10.1016.

Doyen, P.M., 1988. Permeability, conductivity, and pore geometry of sandstone. *Journal of Geophysical Research: Solid Earth*, 93(B7), pp.7729-7740.

Dvorkin, J., Armbruster, M., Baldwin, C., Fang, Q., Derzhi, N., Gomez, C., Nur, B. and Nur, A., 2008. The future of rock physics: computational methods vs. lab testing. first break, 26(9).

Easley, E.J., 2014. A fracture and texture analysis of the Bakken Formation, Montana (Doctoral dissertation, Montana State University-Bozeman, College of Letters & Science).

Elhaj, M., Hashan, M., & Hossain, M. E. (2018, June). A critical review and future trend on relative permeability hysteresis. In SPE Trinidad and Tobago Section Energy Resources Conference. Society of Petroleum Engineers.

Ellis, D.V. and Singer, J.M. 2007. Well logging for earth scientists (Vol. 692). Dordrecht: Springer.

Evans, B., & Wong, T. F. (Eds.). (1992). Fault mechanics and transport properties of rocks. Academic press.

Ewy, R. T., Bovberg, C. A., Hagin, P. N., & Shalz, M. L. (2012, January). Permeability measurement with ultra-high fluid pressure and unequal stresses. In 46th US Rock Mechanics/Geomechanics Symposium. American Rock Mechanics Association.

Fan, L., & Liu, S. (2019). Evaluation of permeability damage for stressed coal with cyclic loading: An experimental study. *International Journal of Coal Geology*, 216, 103338.

Farajzadeh, R., Ranganathan, P., Zitha, P.L.J. and Bruining, J. 2011. The effect of heterogeneity on the character of density-driven natural convection of CO2 overlying a brine layer. Advances in Water Resources, 34(3), pp.327-339.

Feng, R., Harpalani, S., & Pandey, R. (2017). Evaluation of various pulse-decay laboratory permeability measurement techniques for highly stressed coals. Rock Mechanics and Rock Engineering, 50(2), 297-308.

Gan Z, Griffin T, Dacy J, Xie H, Lee R. 2018. Fast pressure-decay core permeability measurement for tight rocks. SPWLA 59th Annual Logging Symposium; Society of Petrophysicists and Well-Log Analysts.

Gerhard LC, Anderson SB, Fischer DW. 1990. Petroleum Geology of the Williston Basin: Chapter 29: Part II. Selected Analog Interior Cratonic Basins: Analog Basins.

Ghabezloo, S., Sulem, J., Guédon, S., & Martineau, F. (2009). Effective stress law for the permeability of a limestone. *International Journal of Rock Mechanics and Mining Sciences*, 46(2), 297-306.

Gonzales, R.C. and Woods, R.E. 2002. Digital image processing.

Grinestaff, G., Barden, C., Miller, J., Franklin, W., Barden, C. and Ding, E., 2020. Evaluation of Eagle Ford Cyclic Gas Injection EOR: Field Results and Economics. Presented at the SPE Virtual Improved Oil Recovery Conference, August 31 – September 4, 2020.

He, J. and Ling, K. 2016. Measuring permeabilities of Middle-Bakken samples using three different methods. *Journal of Natural Gas Science and Engineering*, 31, pp.28-38.

Hegde, C. and Gray, K. E. (2017) Use of machine learning and data analytics to increase drilling efficiency for nearby wells. *Journal of Natural Gas Science and Engineering*, 40, 327–335.

Hoffman, B.T., 2018. Huff-N-Puff Gas Injection Pilot Projects in the Eagle Ford. Presented at the SPE Canada Unconventional Resources Conference, Calgary, Alberta, Canada, March 12–14, 2018.

Hsieh, P. A., Tracy, J. V., Neuzil, C. E., Bredehoeft, J. D., & Silliman, S. E. (1981, June). A transient laboratory method for determining the hydraulic properties of ‘tight’rocks—I. Theory. In International Journal of Rock Mechanics and Mining Sciences & Geomechanics Abstracts (Vol. 18, No. 3, pp. 245-252). Pergamon.

https://www.dmr.nd.gov/ndgs/Resources

Jabbari H, Benson SA. 2013. Hydraulic Fracturing Design Optimization—Bakken Case Study. 47th US Rock Mechanics/Geomechanics Symposium; American Rock Mechanics Association.

Jabbari H. and Z. Zeng. 2011. Hydraulic Fracturing Design for Horizontal Wells in the Bakken Formation. ARMA 11-128, presented at the 46th ARMA held 24-27 June 2012 in Chicago, IL.

Jin H, Lewan M, Sonnenberg SA. 2017. Oil-generation kinetics for oil-prone Bakken Shales and its implication. Unconventional Resources Technology Conference, Austin, Texas, 24-26 July 2017; Society of Exploration Geophysicists, American Association of Petroleum Science.

Jin, Z., C. Lukashin, Y. Qiao, and A. Gopalan. 2013. An efficient and effective method to simulate the earth spectral reflectance over large temporal and spatial scales. *Geophys. Res. Lett.*, 40, no. 2, 374-379.

Jones S., 1997. A technique for faster pulse-decay permeability measurements in tight rocks. *SPE Formation Evaluation*, 12(01):19-26. doi:10.2118/28450-PA.

Jones, F.O. and Owens, W.W. 1980. A laboratory study of low-permeability gas sands. *Journal of petroleum Technology*, 32(09), pp.1-631.

Jouini, Mohamed Soufiane and Vega, Sandra and Al-Ratrout, Ahmed. 2015. Numerical estimation of carbonate rock properties using multiscale images, *Geophysical Prospecting*, 63(2), pp. 405-421.

Kantzas, A., Bryan, J., & Taheri, S. (2012). Fundamentals of fluid flow in porous media. Pore size distribution.

Karimi, S., Kazemi, H. and Simpson, G.A. 2017, March. Capillary pressure, fluid distribution, and oil recovery in preserved Middle Bakken cores. In SPE Oklahoma City Oil and Gas Symposium. Society of Petroleum Engineers

Khan, M. R., Alnuaim, S., Tariq, Z., and Abdulraheem, A. (2019) “Machine learning application for oil rate prediction in artificial gas lift wells” in SPE Middle East Oil and Gas Show and Conference. Society of Petroleum Engineers.

Krantz R, Saltzman J, Blacic J. 1990. Hydraulic diffusivity measurements on laboratory rock samples using an oscillating pore pressure method. International Journal of Rock Mechanics and Mining Sciences & Geomechanics Abstracts; Elsevier.

Kranzz, R. L., Frankel, A. D., Engelder, T., & Scholz, C. H. (1979, August). The permeability of whole and jointed Barre granite. In *International Journal of Rock Mechanics and Mining Sciences & Geomechanics Abstracts* (Vol. 16, No. 4, pp. 225-234). Pergamon.

Kurtoglu, B. 2013. Integrated reservoir characterization and modeling in support of enhanced oil recovery for Bakken (Doctoral dissertation, Colorado School of Mines. Arthur Lakes Library).

Kwon, O., Kronenberg, A. K., Gangi, A. F., & Johnson, B. (2001). Permeability of Wilcox shale and its effective pressure law. *Journal of Geophysical Research: Solid Earth*, 106(B9), 19339-19353.

Lasswell P. 2013. Steady-state permeability analysis in unconventional plays. Proceedings of the GeoConvention, Calgary, Canada, 6–10 May. 2013.

LeFever, J. A., Martiniuk, C. D., Dancsok, E. F., & Mahnic, P. A. (1991). Petroleum potential of the middle member, Bakken Formation, Williston Basin. Williston Basin Symposium.

Li H, Hart B, Dawson M, Radjef E. 2015. Characterizing the middle Bakken: Laboratory measurement and rock typing of the Middle Bakken formation. Unconventional Resources Technology Conference, San Antonio, Texas, 20-22 July 2015; Society of Exploration Geophysicists, American Association of Petroleum.

Lindquist, W.B., Lee, S.M., Coker, D.A., Jones, K.W. and Spanne, P. 1996. Medial axis analysis of void structure in three-dimensional tomographic images of porous media. *Journal of Geophysical Research: Solid Earth*, 101(B4), pp.8297-8310.

Ling K, He J, Pei P, Han G, Zhang H. 2013. Determining the permeability of tight rock with gas transient flow. *Journal of Natural Gas Science and Engineering*, 15:1-7.

Liu K, Ostadhassan M, Gentzis T, Carvajal-Ortiz H, Bubach B. 2018. Characterization of geochemical properties and microstructures of the Bakken Shale in North Dakota. *International Journal of Coal Geology*, 190:84-98.

Liu, K., Ostadhassan, M., & Bubach, B. (2016). Pore structure analysis by using atomic force microscopy. Unconventional Resources Technology Conference (URTEC).

Liu, K., Wang, L., Ostadhassan, M., Zou, J., Bubach, B., & Rezaee, R. (2019). Nanopore structure comparison between shale oil and shale gas: examples from the Bakken and Longmaxi Formations. Petroleum Science, 16(1), 77-93.

Liu, R., Liu, H., Li, X., Wang, J. and Pang, C. 2010, January. Calculation of oil and water relative permeability for extra low permeability reservoir. In International Oil and Gas Conference and Exhibition in China. Society of Petroleum Engineers.

Liu, R., Liu, H., Zhang, H., Tao, Y., & Li, M. 2011. Study of stress sensitivity and its influence on oil development in low permeability reservoir. *J. Rock Mechanics and Engineering*, 30(1), 2697-2702.

Lock, P.A. 2001. Estimating the permeability of reservoir sandstones using image analysis of pore structure (Doctoral dissertation, Department of Earth Science and Engineering, Imperial College).

Lu, X.C., Li, F.C. and Watson, A.T. 1995. Adsorption measurements in Devonian shales. *Fuel*, 74(4), pp.599-603.

Ma X, Zoback M. 2016. Experimental study of dynamic effective stress coefficient for ultrasonic velocities of Bakken cores. SEG Technical Program Expanded Abstracts 2016: Society of Exploration Geophysicists; p. 3221-5.

Ma, X., & Zoback, M. D. (2016, June). Laboratory investigation on effective stress in Middle Bakken: Implications on poroelastic stress changes due to depletion and injection. In 50th US Rock Mechanics/Geomechanics Symposium. American Rock Mechanics Association.

Madadi, M., Jones, A.C., Arns, C.H. and Knackstedt, M.A., 2009. 3D imaging and simulation of elastic properties of porous materials. *Computing in Science & Engineering*, 11(4), pp.65-73.

Maiti, R., Atta, A., & Nigam, K. D. P. (2008). Effect of particle porosity on hysteresis in trickle-bed reactors. *Industrial & Engineering Chemistry Research*, 47(21), 8126-8135.

Metwally, Y. and Chesnokov, E.M. 2010. Measuring gas shale permeability tensor in the lab scale. In SEG Technical Program Expanded Abstracts 2010 (pp. 2628-2633). Society of Exploration Geophysicists.

Metwally, Y. M., & Sondergeld, C. H. 2011. Measuring low permeabilities of gas-sands and shales using a pressure transmission technique. *International J. Rock Mechanics and Mining Sciences*, 48(7), 1135-1144.

Mirzaei, M., and Cipolla, C.L., 2012, A workflow for modeling and simulation of hydraulic fractures in unconventional gas reservoirs: Presented at the SPE Middle East Unconventional Gas Conference and C-4TFibition, UAE, Abu Dhabi: SPE-153022-MS.

Morris, J. P., Lomov, I. N., & Glenn, L. A. (2003). A constitutive model for stress-induced permeability and porosity evolution of Berea sandstone. *Journal of Geophysical Research: Solid Earth*, 108(B10).

Morrow, C. A., Lockner, D. A., Moore, D. E., & Hickman, S. (2014). Deep permeability of the San Andreas fault from San Andreas fault observatory at depth (SAFOD) core samples. *Journal of Structural Geology*, 64, 99-114.

Nagarajan, N. R., Stoll, D., Litvak, M. L., Prasad, R. S., and Shaarawi, K., 2020. Successful Field Test of Enhancing Bakken Oil Recovery by Propane Injection: Part I. Field Test Planning, Operations, Surveillance, And Results. Paper presented at the SPE/AAPG/SEG Virtual Unconventional Resources Technology Conference, July 20–22, 2020. URTEC-2020-2768-MS

Nai, C. A. O., & Gang, L. E. I. 2019. Stress sensitivity of tight reservoirs during pressure loading and unloading process. *J. Petroleum Exploration and Development*, 46(1), 138-144.

Nordeng, S. H., and Helms, L., 2010, Bakken Source System—Three Forks Formation assessment. Bismarck, North Dakota, North Dakota Department of Mineral Resources, 22 p.

North Dakota Industrial Commission, 2021. Department of Mineral Resources, Oil and Gas Division. https://www.dmr.nd.gov/oilgas

Okabe, H. and Blunt, M.J. 2004. Prediction of permeability for porous media reconstructed using multiple-point statistics. *Physical Review E*, 70(6), p.066135.

Paterson, M. S. (1978). Experimental Rock Deformation-The Brittle Field Speringer-Verlag.

PerGeos Manual 2019, Thermo-Fisher Scientific.

Pospisil, G., Griffin, L., Souther, T., Strickland, S., McChesney, J., Pearson, C.M., Dalkhaa, C., Sorensen, J., Hamling, J., Kurz, B. and Bosshart, N., 2022, June. East Nesson Bakken Enhanced Oil Recovery Pilot: Coinjection of Produced Gas and a Water-Surfactant Mixture. In SPE/AAPG/SEG Unconventional Resources Technology Conference.

Pospisil, G., Weddle, P., Strickland, S., McChesney, J., Tompkins, K., Neuroth, T., Pearson, C. M., Griffin, L., Kaier, T., Sorensen, J., and Jin, L., 2020. Report on the First Rich Gas EOR Cyclic Multiwell Huff N Puff Pilot in The Bakken Tight Oil Play. Paper presented at the SPE Virtual Annual Technical Conference and Exhibition, October 26–29, 2020.

Raschka, Sebastian, and Vahid Mirjalili. "Python machine learning: Machine learning and deep learning with python." Scikit-Learn, and TensorFlow. Second edition ed 3 (2017).

Reynolds, O. (1883). XXIX. An experimental investigation of the circumstances which determine whether the motion of water shall be direct or sinuous, and of the law of resistance in parallel channels. Philosophical Transactions of the Royal society of London, (174), 935-982.

Saenger, E.H. and Madonna, C. 2011. Digital rock physics: Numerical vs. laboratory measurements. In SEG Technical Program Expanded Abstracts 2011 (pp. 3693-3697). Society of Exploration Geophysicists.

Saif, T., Lin, Q., Butcher, A.R., Bijeljic, B. and Blunt, M.J. 2017. Multi-scale multi-dimensional microstructure imaging of oil shale pyrolysis using X-ray micro-tomography, automated ultra-high-resolution SEM, MAPS Mineralogy and FIB-SEM. Applied energy, 202, pp.628-647.

Sanaei, A., Abouie, A., Tagavifar, M. and Sepehrnoori, K., 2018, September. Comprehensive study of gas cycling in the Bakken shale. In Unconventional Resources Technology Conference, Houston, Texas, 23-25 July 2018.

Sang, G., Elsworth, D., Liu, S., & Harpalani, S. (2017). Characterization of swelling modulus and effective stress coefficient accommodating sorption-induced swelling in coal. *Energy & Fuels*, 31(9), 8843-8851.

Selvadurai, A. P. S. 2015. Normal stress-induced permeability hysteresis of a fracture in a granite cylinder. *J. Geofluids*, 15(1-2), 37-47.

Sharma, A. and Sharma, A. (2018) Machine learning: A review of techniques of machine learning.JASC *J. Appl. Sci. Comput*, 5, 538–541.

Shi Y, Wang CY. 1986. Pore pressure generation in sedimentary basins: overloading versus aquathermal. *Journal of Geophysical Research: Solid Earth*. 91(B2):2153-62.

Sigal, R. F. 2002. The pressure dependence of permeability. *Petrophysics*, 43(02).

Sinha S, Braun EM, Passey QR, Leonardi SA, Wood III AC, Zirkle T, et al. 2012. Advances in measurement standards and flow properties measurements for tight rocks such as shales. SPE/EAGE European Unconventional Resources Conference & Exhibition-From Potential to Production; European Association of Geoscientists & Engineers.

Smith MG, Bustin RM, 1995. Sedimentology of the Late Devonian and Early Mississippian Bakken Formation, Williston Basin: Williston Basin Symposium.

Sondergeld, C.H., Newsham, K.E., Comisky, J.T., Rice, M.C. and Rai, C.S. 2010, January. Petrophysical considerations in evaluating and producing shale gas resources. In SPE unconventional gas conference. Society of Petroleum Engineers.

Sorensen JA, Kurz BA, Hawthorne SB, Jin L, Smith SA, and Azenkeng A. 2017. Laboratory characterization and modeling to examine CO2 storage and enhanced oil recovery in an unconventional tight oil formation. *Energy Procedia*. 114:5460-78.

Sorensen, J. A., and Hamling, J. A., 2016. Historical Bakken Test Data Provide Critical Insights on EOR in Tight Oil Plays. *American Oil & Gas Reporter*, 59(2): 55–61.

Soulaine, C., Gjetvaj, F., Garing, C. et al. 2016. The Impact of Sub-Resolution Porosity of X-ray Microtomography Images on the Permeability. *Transp Porous Med*, 113, 227–243.

Sturm, S.D. and Gomez, E., 2009, June. Role of natural fracturing in production from the Bakken Formation, Williston basin North Dakota. In AAPG Annual Convention and Exhibition (Vol. 50199).

Tang Y, Tang J, Liu Q, Wang Y, Zheng Z, Yuan Y, et al. 2020. Review on Phase Behavior in Tight Porous Media and Microscopic Flow Mechanism of CO2 Huff-n-Puff in Tight Oil Reservoirs. Geofluids. 2020.

Teklu TW, Li X, Cui Q, Abass H, Zhou Z. 2016. Fracture and matrix permeability hysteresis in organic rich mudrocks. Unconventional Resources Technology Conference, San Antonio, Texas, 1-3 August 2016; Society of Exploration Geophysicists, American Association of Petroleum. doi:10.15530

Teklu, T. W., Li, X., Zhou, Z., & Abass, H. (2018). Experimental investigation on permeability and porosity hysteresis of tight formations. *SPE Journal*, 23(03), 672-690.

Teklu, T. W., Zhou, Z., Li, X., & Abass, H. (2016, June). Cyclic permeability and porosity hysteresis in mudrocks–experimental study. In 50th US Rock Mechanics/Geomechanics Symposium. American Rock Mechanics Association.

Teklu, T. W., Zhou, Z., Li, X., & Abass, H. (2016, May). Experimental investigation on permeability and porosity hysteresis in low-permeability formations. In SPE Low Perm Symposium. Society of Petroleum Engineers.

Terzaghi, K. (1943). Earth pressure and shearing resistance of plastic clay: a symposium: liner-plate tunnels on the Chicago (IL) subway. *Transactions of the American Society of Civil Engineers*, 108(1), 970-1007.

Thomson, P.R., Aituar-Zhakupova, A. and Hier-Majumder, S. 2018. Image segmentation and analysis of pore network geometry in two natural sandstones. *Frontiers in Earth Science*, 6, p.58.

Trimmer D. 1982. Laboratory measurements of ultralow permeability of geologic materials. *Review of Scientific Instruments*. 53(8):1246-54.

Van Noort, R., & Yarushina, V. (2019). Water, CO 2 and Argon Permeabilities of Intact and Fractured Shale Cores Under Stress. *Rock Mechanics and Rock Engineering*, 52(2), 299-319.

van Oort, E. (1994, January). A novel technique for the investigation of drilling fluid induced borehole instability in shales. In Rock mechanics in petroleum engineering. Society of Petroleum Engineers.

Vigil, G., Xu, Z., Steinberg, S., & Israelachvili, J. (1994). Interactions of silica surfaces. *Journal of Colloid and Interface Science*, 165(2), 367-385.

Walsh, J. B. (1965). The effect of cracks on the compressibility of rock. *Journal of Geophysical Research*, 70(2), 381-389.

Wang, H.F. and Hart, D.J. 1993. December. Experimental error for permeability and specific storage from pulse decay measurements. In International journal of rock mechanics and mining sciences & geomechcoles

Wang, S., & Civan, F. 2005. Modeling formation damage by asphaltene deposition during primary oil recovery.

Wang, Z., Jin, X., Wang, X., Sun, L. and Wang, M. 2016. Pore-scale geometry effects on gas permeability in shale. *Journal of Natural Gas Science and Engineering*, 34, pp.948-957.

Warpinski, N. R., & Teufel, L. W. (1992). Determination of the effective-stress law for permeability and deformation in low-permeability rocks. *SPE Formation Evaluation*, 7(02), 123-131.

Warren, J.E., and Root, P.J., 1963, The behavior of naturally fractured reservoirs. *Society of Petroleum Engineers Journal*, v. 3, no. 3, p. 245–255.

Whitaker, S. 2013. The method of volume averaging (Vol. 13). Springer Science & Business Media.

Wissler, T. M., & Simmons, G. (1985, December). The physical properties of a set of sandstones—Part II. Permanent and elastic strains during hydrostatic compression to 200 MPa. In International Journal of Rock Mechanics and Mining Sciences & Geomechanics Abstracts (Vol. 22, No. 6, pp. 393-406). Pergamon.

Xu, C., Lin, C., Kang, Y., & You, L. (2018). An experimental study on porosity and permeability stress-sensitive behavior of sandstone under hydrostatic compression: characteristics, mechanisms and controlling factors. *Rock Mechanics and Rock Engineering*, 51(8), 2321-2338.

Yang Z., X. Liu, Z. Zhang, T. Zhou, and S. Zhao. 2015. Physical simulation of staged-fracturing horizontal wells using CO2 huff and puff in tight oil reservoirs. *Acta Petrolei Sinica*, vol. 36, no. 6, pp. 724–729.

Yoshino, M., Taniguchi, M., Imaizumi, K., Miyasaka, S., Tanijiri, T., Yano, H., David, C., Thomas, L. and Clement, J.G. 2005. A new retrieval system for a database of 3D facial images. *Forensic Science International*, 148(2-3), pp.113-120.

Yu, W., Javadpour, F., Varavei, A., and Sepehrnoori, K., 2014, Sensitivity analysis of hydraulic fracture geometry in shale gas reservoirs: *Journal of Petroleum Science and Engineering*, v. 113, p. 1–7.

Zeynaly-Andabily, E. M., & Rahman, S. S. (1995). Measurement of permeability of tight rocks. *Measurement Science and Technology*, 6(10), 1519.

Zhang, J., Wong, T. F., & Davis, D. M. (1990). Micromechanics of pressure-induced grain crushing in porous rocks. *Journal of Geophysical Research: Solid Earth*, 95(B1), 341-352.

Zhang, Y., Yu, W., Li, Z. and Sepehrnoori, K. 2018. Simulation study of factors affecting CO2 Huff-n-Puff process in tight oil reservoirs. *Journal of Petroleum Science and Engineering*, 163, pp.264-269

Zhou, Z., Abass, H., Li, X., & Teklu, T. (2016). Experimental investigation of the effect of imbibition on shale permeability during hydraulic fracturing. *Journal of Natural Gas Science and Engineering*, 29, 413-430.

Zoback, M. D., & Byerlee, J. D. (1975). Permeability and effective stress. *AAPG Bulletin*, 59(1), 154-158.